Wave Speed Measurements of Grosmont Formation Carbonates: Implications for Time-Lapse Seismic Monitoring

by

Nam (Oliver) Ong

A thesis submitted in partial fulfillment of the requirements for the degree of

Master of Science

in

Geophysics

Department of Physics

University of Alberta

Abstract

The Grosmont Formation is a Devonian-aged carbonate platform complex that is estimated to hold over 64.5 billion m^3 (406 billion bbl) of bitumen in place, accounting for a significant portion of Canada's total hydrocarbon reserves. Despite this, the Grosmont formation has largely been undeveloped as a reservoir due to the high degree of heterogeneity, as well as the economic and environmental risks associated with in-situ heavy oil production. For such operations, thermal processes such as steam-assisted gravity drainage (SAGD) are used to reduce the viscosity of the reservoir fluids, allowing them to flow freely towards producing wells. Time-lapse seismic (4D) methods are key tools used to monitor this process, allowing operators to potentially mitigate these risks associated with producing from such a reservoir. However, the proper interpretation of 4D seismic data requires detailed knowledge of how the physical properties of the reservoir rocks respond to the variety of pressure, temperature, and saturation conditions induced by steam injection. In this contribution, bitumen-saturated carbonates from the Grosmont Formation are characterized through ultrasonic velocity experiments conducted in a range of conditions. P- and S-wave velocities of bitumen-saturated samples decreased significantly with increasing temperature, largely governed by fluid effects. Principal component analysis (PCA) of the wave speed measurements highlighted porosity, temperature, pressure, and grain density as the main factors that contributed to velocity variations within and between samples. Multiple linear regressions applied to the dataset of wave speed measurements establish empirical relations between velocity and the predictor variables determined through PCA. These results provide insight into the behavior of heavy oil saturated rocks under production conditions, however, further measurements at seismic and well-logging frequency ranges are recommended for proper interpretation of seismic data.

Preface

This thesis is submitted for the degree of Master of Science in Geophysics at the University of Alberta. The research conducted for this thesis forms part of a research collaboration between the University of Alberta, Laricina Energy Ltd., and Osum Oil Sands Corp., led by Professor Douglas R. Schmitt.

Chapter 6 of this thesis has been submitted for publication as "Ong, O.N., Schmitt, D.R., Rabbani, A., Kofman, R.S., 2018. Wave speed measurements of bitumen-saturated carbonates under thermal recovery conditions – Empirical relations and multi-variate analysis. Submitted. *Geophys. Prospect.*" I was responsible for the data collection, analysis, and manuscript composition. Prof. Douglas Schmitt was the supervisory author and was involved in manuscript preparation.

Acknowledgements

Foremost, I would like to express the gratitude and appreciation I have towards my advisor, Dr. Douglas R. Schmitt. He was not only my supervisor, but my mentor and friend who has provided unwavering support, guidance, and encouragement throughout my undergraduate and graduate academic career. To my supervisory committee, Dr. Mauricio Sacchi, Dr. Moritz Heimpel, and Dr. Erik Rosolowsky; thank you for taking the time to review and provide feedback for this work.

This project was made possible with the support of our industry partners: Laricina Energy Ltd. and Osum Oil Sands Corp, as well as financial support from NSERC. In particular, I would like to thank Jason Nycz and Ken Gray for their expertise and unrelenting support of this project. Thank you to Randy Kofman; your skills, expertise, and friendly chatter were instrumental in making this project a success.

I would also like to thank my friends and colleagues: Tariq Mohammed, Micah Morin, Chris Nixon, Sean Murray, Olivia Henderson, Deirdre Mallyon, Ryan Ferguson, Sean Bettac, and many others who I have spent countless hours collaborating with. Great works are hardly ever completed in isolation, and this is no exception.

And finally, to my partner, Humirah Sultani. Your love, support, and sacrifices mean the world to me and for which, I can only hope for the opportunities to repay you. I could not have done this without you; thank you for always being by my side.

Table of Contents

List of Tables

List of Figures

1 Introduction

The Devonian Grosmont Formation is a bitumen-bearing carbonate complex present in the subsurface of north-eastern and central Alberta, Canada. The formation spans approximately 150 km in width, and 600 km in length, with estimated reserves projected at 64.5 billion m^3 (406 billion bbl) of bitumen in place (Burrowes et al., 2010). The bitumen hosted within the heavily karsted and fractured carbonate platform account for a significant portion of Canada's total oil reserves, however, in contrast to the nearby Athabasca oil sands deposit, the Grosmont formation has remained relatively unexploited (Ardakani et al., 2014). This is largely due to the complex nature of the reservoir along with the challenges associated with its production.

Similar to the oil sands, the bitumen residing within the carbonates is immobile at reservoir temperatures, requiring the use of thermal recovery methods such as cyclic steam stimulation (CSS) and steam-assisted gravity drainage (SAGD) for in-situ production (Jiang et al., 2010; Mohebati et al., 2014; Rabbani and Schmitt, 2018; Yang et al., 2014). The basis of these techniques involves the injection of steam into the reservoir to reduce the viscosity of the bitumen, allowing it to flow freely throughout the pore space. Time-lapse methods such as 4D seismic are often employed to monitor the effectiveness of such recovery techniques, allowing operators to greatly reduce the economic and environmental risks associated with unintended injected fluid loss.

1.1 Motivation

It has been shown that 4D seismic methods are an effective tool for monitoring thermal recovery processes (Oldenziel, 2003; Shabelansky et al., 2015) within heavy oil reservoirs. During SAGD and CSS operations, injected steam can cause significant changes in reservoir conditions including elevated temperatures, changes in effective and pore pressures, changes in gas saturation, and substitution of bitumen with steam and water (Bianco et al., 2008).

These variations in reservoir conditions also reflect a change in seismic response, which can be captured by acquiring multiple seismic surveys over the course of production (Kato et al., 2008; Schmitt, 1999; Zhang et al., 2007). Conventionally, time-lapse seismic data is interpreted in a qualitative manner by comparing amplitudes and travel time differences between surveys, however, there have been recent attempts to transition to quantitative interpretation methods (Chadwick et al., 2010; Mutual et al., 2017; Shabelansky et al., 2015). This is often achieved by through the application of rock physics models or empirical relationships, which relate the changes in velocity or seismic response to the changes in temperature, pressure, and saturation.

The work completed in this thesis was motivated by the need to further understand the relationships between thermal enhanced recovery processes and the physical properties of rocks taken from the Grosmont Formation. In this contribution, we describe an extensive series of ultrasonic velocity measurements made on naturally-saturated candidate Grosmont Formation samples under various temperature, pressure, and saturation conditions.

1.2 Thesis Organization

The primary interest of this thesis is to develop an understanding of how the changes in temperature, pressure, and fluid saturation associated with thermal enhanced recovery methods govern the seismic response of Grosmont Formation reservoir rocks. To investigate these relationships, a series of ultrasonic velocity experiences are carried out under specific measurement conditions. In Chapter 2, a literature review is completed on previous works that have attempted to understand the properties of carbonates and heavy oil saturated rocks through the use of laboratory experiments. This chapter includes a section providing a brief geological overview of the Grosmont Formation of Alberta, Canada.

Chapter 3 discusses the theoretical background that is relevant to the work completed in this thesis. First, an overview of the theory of elasticity and wave propagation is given in the

context of isotropic media. A brief review of the effects of viscoelasticity and common linearly viscoelastic models is provided. Following this, two commonly used fluid substitution formulations developed by Gassmann and Biot are discussed in the context of their applicability and underlying assumptions.

In Chapter 4, the methodology behind the ultrasonic velocity experiments are reviewed. This includes a discussion of the Pulse Transmission Method, detailing the experimental configuration and workflow, sample preparation, ultrasonic transducer assembly, and challenges associated with velocity measurements conducted at high pressure and temperature conditions. This chapter also examines the petrophysical properties with detailed review of the sample characterization methods used.

In Chapter 5, we investigate the ultrasonic velocity trends in terms of its pressure and temperature dependence. A brief discussion of the effect of changing fluid saturation conditions is also explored, however, a more detailed and rigorous investigation will be provided in future contributions.

Chapter 6 focuses on the development of a template for describing the P- and S-wave behaviour of the bitumen-saturated Grosmont samples. A version of this chapter is submitted to Geophysical Prospecting (Ong et al., 2018) and as such, the chapter includes similar reviews of laboratory measurements in literature, methodology, and geological context. This chapter includes a discussion on principal component analysis and its applicability towards regression problems and understanding key relationships between measured variables.

Finally, in Chapter 7, we summarize the key findings from the thesis and propose future directions for research.

Additionally. the author apologizes in advance for any replication or redundant material that appears within this thesis due to certain chapters which were prepared as manuscripts for journal submission.

2 Background Information

2.1 Literature Review on Laboratory Measurements

It is estimated that approximately half of the world's total hydrocarbon reserves are hosted within carbonate reservoirs (Ahr, 2011), making them an important topic for ongoing research. Despite the abundance of these oil fields, carbonate reservoirs are considered to be more challenging to develop in comparison to their siliciclastic counterparts for a variety of reasons. Such reservoirs are typically deposited in complex geometries, with post-depositional processes adding further alterations and heterogeneity to the reservoirs. Diagenesis in particular, can drastically change the pore structure and porosity distribution within the reservoir.

The understanding of elastic properties in these carbonate reservoirs is equally challenging due to the complex lithologic influences on the wave velocities. In exploration seismology, knowledge of how changes in these geological factors affect wave velocity is crucial for the interpretation of surface seismic data. As such, there is a need for measurements of the elastic properties in controlled laboratory settings.

Most commonly, laboratory characterization of the elastic properties in carbonates are based on ultrasonic methods, which includes the pulse transmission (discussed in detail in Section 4.1), pulse echo, and resonant bar / forced oscillation methods. Many studies have been conducted to measure ultrasonic compressional and shear velocities in carbonate rocks (Anselmetti and Eberli, 1993; Assefa et al., 2003; Bakhorji, 2010; Best, 1997; Gegenhuber and Pupos, 2015; Martínez and Schmitt, 2013; Rafavich et al., 1984; Wang, 1997) with results showing large variability in velocity measurements. Many of these studies suggest pore structure and pore types to be the likeliest controlling factors of velocity variations within samples. In addition to ultrasonic studies, there have also been several studies that have aimed to measure the elastic properties of carbonate rocks at extended seismic frequencies

in order to measure the degree of velocity dispersion (Adam et al., 2006; Makarynska et al., 2010; Mikhaltsevitch et al., 2016).

As many of the world's largest oil deposits are hosted within carbonate rocks, it should be no surprise that there are many studies exploring the effects of fluid saturation on these rocks. Numerous studies have shown results to suggest a matrix-weakening effect with increasing fluid saturation (Adam et al., 2006; Assefa et al., 2003; Baechle et al., 2009). These studies are of particular significance to the widely-used Gassmann fluid substitution model as they invalidate the assumption that fluid saturation has no effect on the frame of the rock.

Another consideration for modelling fluid saturation effects is the viscoelastic nature of heavy oil, invalidating the Gassmann model assumption that the saturating fluid has no shear modulus. This viscoelastic behaviour is similarly observed in measurements of heavy oil bearing rocks such like the samples collected from the Grosmont formation, in which we will provide evidence for later in this thesis. It is this viscoelastic response which governs the dramatic decrease in seismic velocity of heavy oil reservoirs during SAGD operations. With steam injection, the increase in temperature reduces the viscosity of the reservoir fluid to the point in which in-situ production is achievable.

In early studies of clastic rocks saturated with heavy oil, such as the oil sands from the Athabasca bitumen deposit, laboratory measurements showed significant decreases in compressional and shear velocities with increasing temperature (Nur et al., 1984; Wang and Nur, 1988). It is with these observations that the authors of these studies suggested the use of seismic methods to map out fluid effects within these heavy oil reservoirs in order to monitor production. Subsequent work by Wang et al. (1990) and Batzle and Wang (1992) came to similar conclusions through the study of rocks saturated with oils of varying densities. Eastwood (1993) studied the dependence of ultrasonic velocity on temperature and found the results to be consistent with theoretical model predictions. Both theoretical and experimental results showed a decrease of compressional velocity with increasing temperature attributed

by the change in fluid bulk modulus. Further studies into the properties of the heavy oil itself include the works of Wang and Nur (1990), Daridon et al. (1998), Batzle et al. (2006), Han et al. (2008), and Rabbani et al. (2015). The studies also postulated that at sufficiently low temperatures, the heavy oil acts as a viscoelastic solid with a non-negligible shear modulus (Rabbani and Schmitt, 2018).

In more recent developments, the temperature dependence of heavy oil unconsolidated sands have been reaffirmed in the laboratory measurements of Martinez et al. (2012) and Yuan and Han (2013). In addition to the experimental work, there have been efforts to model the changes in acoustic response of heavy oil bearing rocks in order to further the understanding of time-lapse seismic data (Guo and Han, 2016; Gurevich et al., 2008; Makarynska et al., 2010; Wang et al., 2015; Yuan et al., 2016).

Despite the substantial amount of work completed on oil sands, studies on heavy oil hosted carbonates are still relatively spare. Rabbani et al. (2017) studied the ultrasonic velocity and attenuation of a bitumen-saturated carbonate sample from the Grosmont Formation under various pressure, saturation, and temperature conditions. The study showed a decrease in P- and S-wave velocities of 12% and 9% respectively, over a temperature range of 10°C - 102°C. In a similar study, Yuan et al. (2017) compared the velocity and attenuation trends of bitumen-saturated sands and carbonates in conditions analogous to a heated reservoir. P- and S-wave velocities were observed to decrease under 10% over a temperature range of 10°C – 120°C for the bitumen-saturated carbonate. Comparatively, over the same temperature range, the bitumen-saturated sand showed a decrease in velocities of 33%.

This thesis builds on the initial work of Johnston (2010), Yuan et al. (2018, 2017), and Rabbani et al. (2017) to further focus on the physical properties of bitumen-saturated carbonates taken from the Grosmont Formation. This study aims to study these properties over a wider range of confining pressure, pore pressure, and temperatures to build a unique and publicly

available data set that provides a strong framework for the development of empirical predictive relationships.

2.2 Geological Framework

The Upper Devonian Grosmont Formation is an extensive bitumen-bearing carbonate platform covering a substantial area of north-central and north-eastern Alberta. Contained within the Woodbend Group of the Western Canadian Sedimentary Basin (WCSB), the rock body was first described by Belyea (1952) as the Grosmont 'member' using drill cuttings from the Imperial Grosmont No. 1 13-17-67-23W4 well, and was named after the nearby hamlet of Grosmont, Alberta. In later studies of the geology of north-western Alberta by Law (1955), the Grosmont 'member' was promoted to formation status and subsequently referred to as such.

The Grosmont carbonate platform spans approximately 150 km in width and 500 km in length (Figure 2.1), comparable both in size and depositional environment to the present-day Bahama platform (Ardakani et al., 2014; Buschkuehle et al., 2007). In the western section, the Grosmont formation is overlain by the Devonian Upper Ireton and Nisku formations and is underlain by the Lower Ireton formation. However, at its eastern extent, the formation progressively thins out and subcrops against the Lower Cretaceous sediments of the McMurray formation (Figure 2.2). The Grosmont formation itself is subdivided into four stratigraphic units, which had initially been assigned the designation Lower Grosmont (LG), Grosmont 1 (G1), Grosmont 2 (G2), and Grosmont 3 (G3) in order of descending age. This terminology was adopted following Cutler (1983), who delineated the regionally correlatable argillaceous units through the interpretation of well logs and cores. In recent literature, the units of the Grosmont formation are more commonly referred to as the Grosmont A (GMA), B (GMB), C (GMC), and D (GMD) in place of LG, G1, G2, and G3 respectively. Hereafter, we will refer to each unit using this nomenclature. Each unit is separated by regionally extensive shales and marl commonly referred to as the "Grosmont shale breaks". Produced from regressive events,

these shales and marls are readily distinguishable on geophysical logs (Figure 2.3) and act as markers separating the units (Ardakani et al., 2014; Jones et al., 2003).

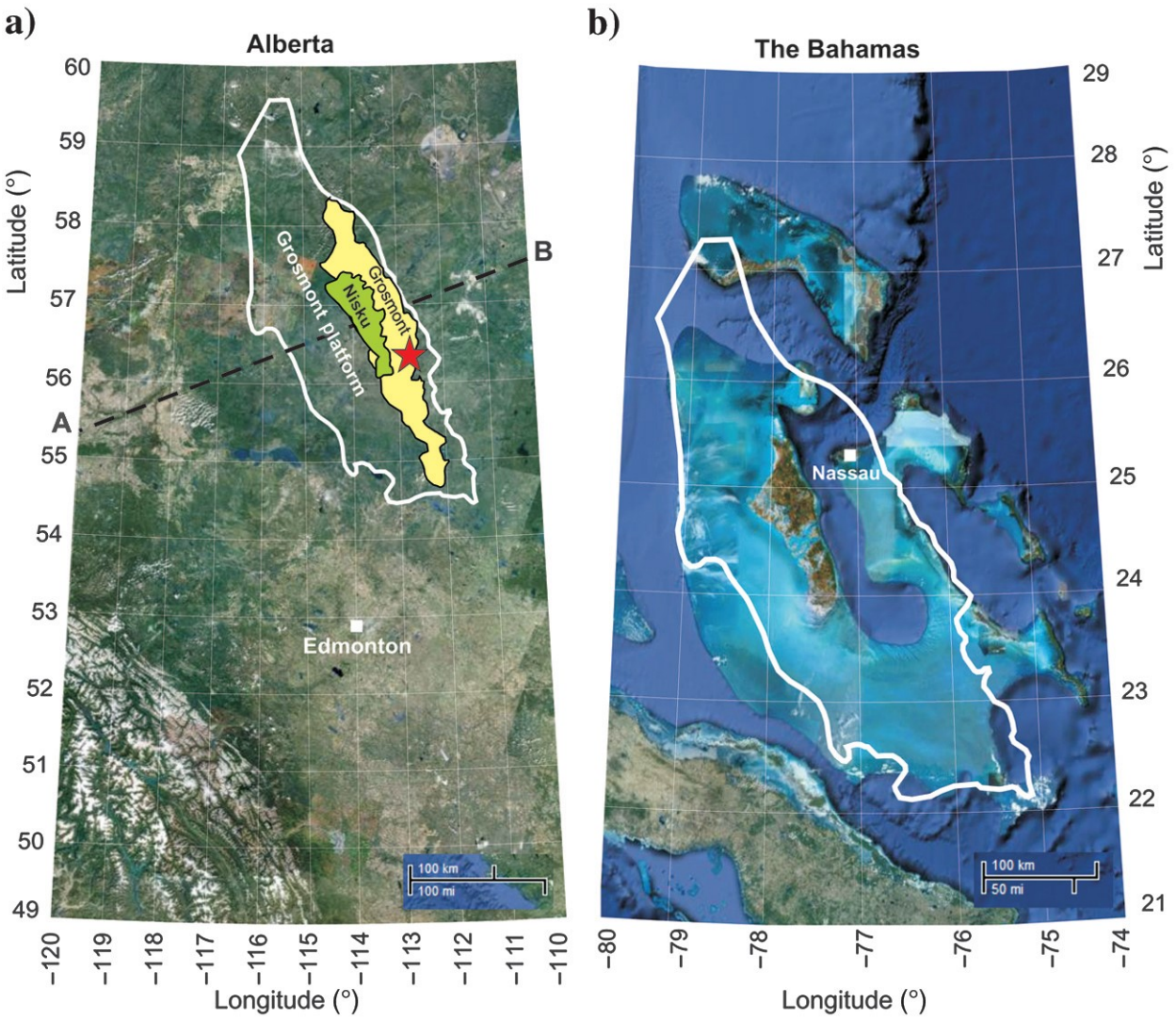

Figure 2.1: A comparison of satellite images of (a) Alberta showing the extent of the Grosmont carbonate platform in white and (b) the Bahama Banks acting as a modern-day shallow-water carbonate platform. The areas of the Grosmont and Nisku carbonate bitumen deposits are highlighted in yellow and green respectively while the study area is indicated by the red star. The outline of the Grosmont platform in Figure 2.1(a) is superimposed onto Figure 2.1(b) at the same scale. Figure from Ardakani et al. (2014) with permission granted from the Society of Exploration Geophysicists through their Fair Use Policy.

The units of the Grosmont formation represent successive stages in the evolution of a huge carbonate complex that consists mostly of shallow-water platform carbonates, reefal buildups,

deeper water marls, and some evaporites (Machel et al., 2012). The Grosmont formation, along with the other major subdivisions of the Woodbend Group (Cooking Lake, Duvernay, Leduc, and Ireton formations) represent intervals of major eustatic sea level changes in which platform carbonates, reefs, and shales were deposited during marine transgression. The Grosmont platform itself was deposited in the late Devonian and subsequently experienced subsidence and burial. It is at this stage in which dolomitization began, transforming the deposited limestone into dolomite (Huebscher and Machel, 1997). Dolomitization is pervasive in GMC and GMD while the units GMA and GMB remain primarily composed of limestone.

Following this was a long period of uplift and erosion where subaerial exposure to meteoric water resulted in pervasive karstification within the formation (Machel et al., 2012). This process is a major control on reservoir quality as karstification creates porosity and fractures through the dissolution of carbonate rock from the weakly acidic water. These karst features range in scale from small microscopic pores, to macro-sized vuggy porosity, and large caverns spanning tens of meters (Buschkuehle et al., 2007). Such features have been identified using surface seismic methods on both the local (Ardakani et al., 2014; Bown, 2011) and regional scale (Russel-Houston and Gray, 2014a).

The units GMC and GMD have the largest degree of karstification and as such, are considered to have the highest reservoir potential (Mohebati et al., 2014). In the study area, the GMC has an average thickness of 33 meters and an average porosity of 18.6%. The unit is further subdivided into five informal units named after their main facies associations: Lower Argillaceous Dolomite, Fractured Large Vug, Small Vug, High Porosity, and Upper Grosmont C / GMC (Barrett, 2016).

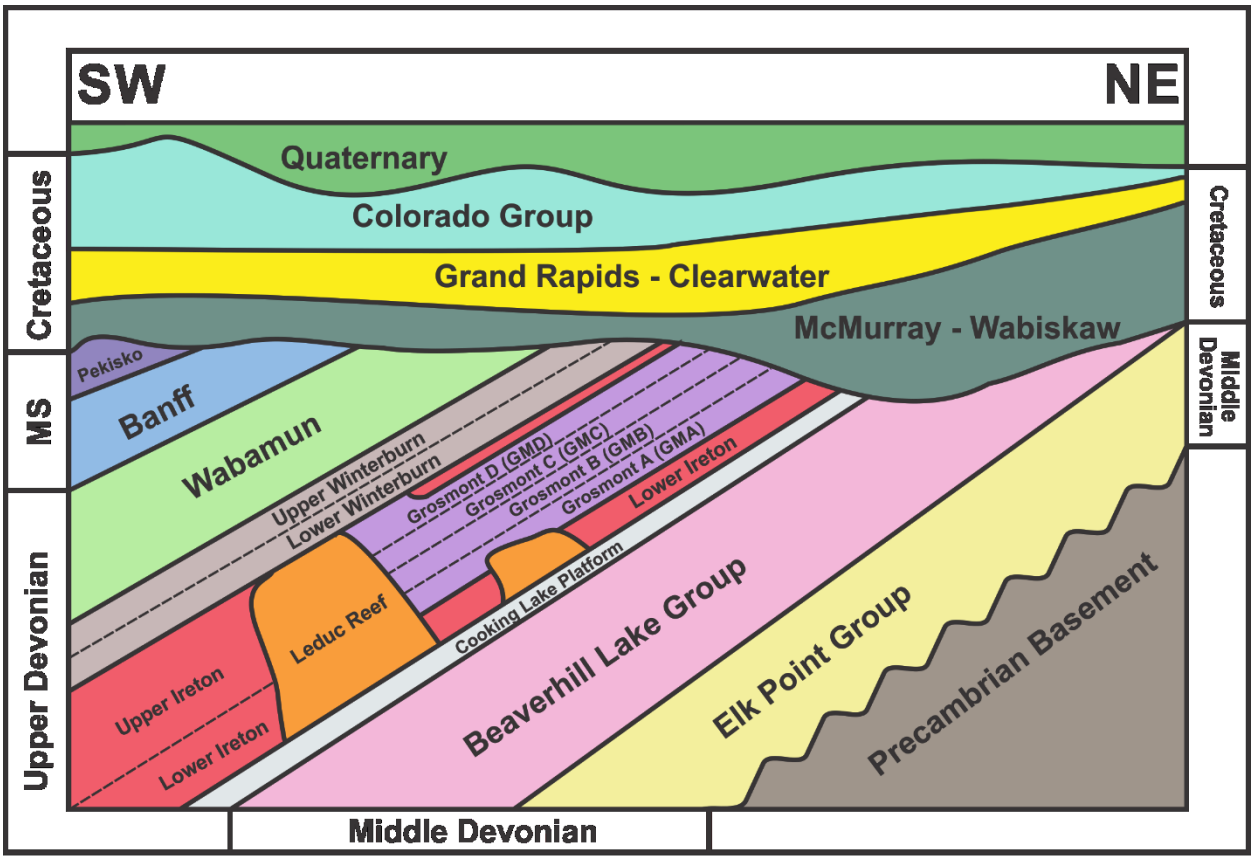

Figure 2.2: Regional stratigraphic cross section running from Southwest to Northeast Alberta through the study area. Modified from Buschkuehle et al., (2007) with permission granted from Springer Nature.

The GMC Lower Argillaceous unit is an approximately 13.3 m thick, highly bioturbated dolowackestone to dolomudstone. The interval has a high clay mineral content with numerous irregular and discontinuous shale partings (Putnam et al., 2016). Despite having an average porosity of 9.5%, the unit has a matrix permeability of less than 10 mD and therefore classified as a non-reservoir unit (Barrett, 2016). The underlying GMC Fractured Large Vug unit consists of an approximately four meters thick, intensively bioturbated, massive dolomite wackestone. Irregularly-scattered, discontinuous shale partings can be found throughout the interval and produces an elevated gamma ray response. Porosity values average 13.5% with the dominant pore type being of vugular nature. The vugs are typically greater than 0.5 cm

in diameter and are thought to have been formed by the leeching of burrows. Furthermore, these vugs appear to be connected by randomly oriented sub-vertical fractures which are mainly less than 3 cm in length (Barrett, 2016).

The GMC Small Vug unit consists of an approximately 6.5 m thick, stromatoporoid-rich dolomite with an average porosity of 17.9%. Common pore types found in this interval include pinpoint vug, intrafossil, and intercrystalline porosity, however the majority of the pore space is attributed to small vugs that are typically 0.1 – 0.5 cm in diameter. Similar to the underlying Fractured Large Vug unit, the vugs are thought to be a product of fossil material leeching. With an average thickness of 2.5 m, the GMC High Porosity unit is composed of a dolomite interval that grades between a laminated dolomite with significant fine pinpoint vuggy porosity and bitumen-saturated carbonate consisting of silt and sand sized dolomite crystals termed disaggregated dolomite (Barrett, 2016). Particle size analysis of the disaggregated dolomite matrix yield median and mean grain sizes of 55 and 121 microns, respectively. Furthermore, the unit shows great potential with average porosity and bitumen saturation values of 31.4% and 82.2% respectively, which are higher than any other GMC interval. Finally, the Upper GMC unit is a clean dolomite interval typically consisting of laminated fine-grained grainstones overlain by vuggy mudstones and a thick slightly argillaceous, bioturbated mudstone sub-unit.

The Grosmont D unit is approximately 32 m thick with an average porosity of 24.3% determined from core analyses. The unit is further subdivided into the Lower, Middle, and Upper GMD intervals. The Lower GMD interval includes an approximately 1 m thick marl layer termed the CD Marl, which separates the GMC and GMD units as well as as 11-16 m thick dolomite breccia interval. The CD Marl layer is composed primarily of interbedded siliclastic green shales, bioturbated low porosity dolomite, and fine bitumen-saturated disaggregated dolomite. This layer is part of the previously mentioned “shale breaks” due to its elevated gamma ray response from its high clay content. It is noted that this layer is of particular

interest to reservoir engineers as it may act as a potential barrier or baffle to fluid flow in the context of steam recovery methods (Barrett, 2016). The remainder of the Lower GMD unit consists of karst breccia with angular dolomite clasts enclosed in a matrix of disaggregated dolomite. The breccia clasts range from pebble size to tens of centimeters in diameter. This interval is the thickest, and most porous among all other Grosmont bitumen bearing units with saturation levels of approximately 83.6%. The majority of the porosity in the Lower GMD unit is intergranular within the disaggregated dolomite with permeability values less than 100 MD.

The Middle GMD unit is approximately 10 m thick and consists of moderately fractured alternating argillaceous and non-argillaceous dolomite beds. Average porosity and bitumen saturation for this interval is approximately 14% and 67.7% respectively. Lastly, the Upper GMD unit is composed of a laminated dolomite grainstone featuring occasional stromatolites and is relatively clay-free. The lower portion of this interval consists of a dolomite breccia similar to the Lower GMD unit. Average porosity and bitumen saturation are 26.1% and 80.6%, respectively. Common pore types found within this interval include pinpoint vugs, intercrystalline, intraparticle, and fracture (Barrett, 2016).

The source rock, defined as a rock that has generated or is capable of generating hydrocarbons, has been a long-debated topic for the Grosmont formation. Early studies have identified the Devonian Duvernay formation along with the Carboniferous Exshaw formation as the principle source rocks (Dawson and Kalkreuth, 1994; Hitchon and Filby, 1984; Stoakes and Creaney, 1984), however, recent literature has come to suggest that most of the oil that migrated to the Grosmont formation was derived from the Jurassic Fernie Group (Higley et al., 2009). Many of these studies note that the characteristics of the Grosmont formation bitumen are similar to that of the bitumen in the Athabasca oil sand deposit, and as such are likely to share the same source rock. After migration, the light oil was then biodegraded into bitumen by bacteria present in the near-surface formation waters.

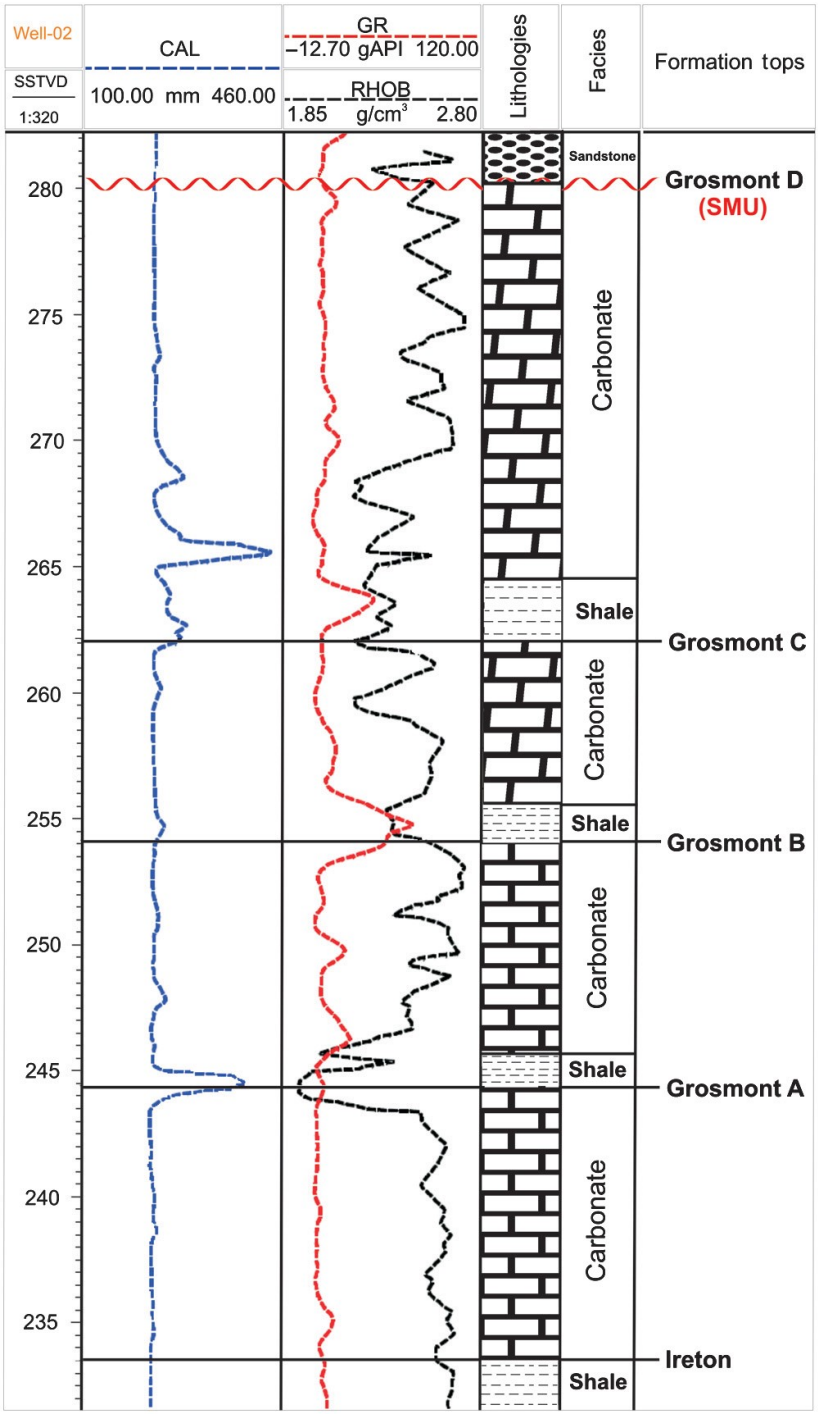

Figure 2.3: Typical well log highlighting the tops of major subdivisions in the Grosmont formation along with overlaying strata. "Shale breaks" markers have higher radioactivity signatures that are easily distinguished in gamma ray logs. Figure from Ardakani et al. (2014) with permission granted from the Society of Exploration Geophysicists through their Fair Use Policy.

Five samples used in this study are sourced from the 100/01-27-085-19W4 well at the Saleski Pilot Site. Figure 2.4 highlights the main reservoir units of the Grosmont formation on the representative well log at the study area. The samples that were sourced from this well are marked on the log at their corresponding depths. The 6th sample was taken from the 101/10-26-85-19W4 well at a depth of 360.79 m within unit. All samples were taken from within GMC, GMD, and the marl layer separating the two intervals.

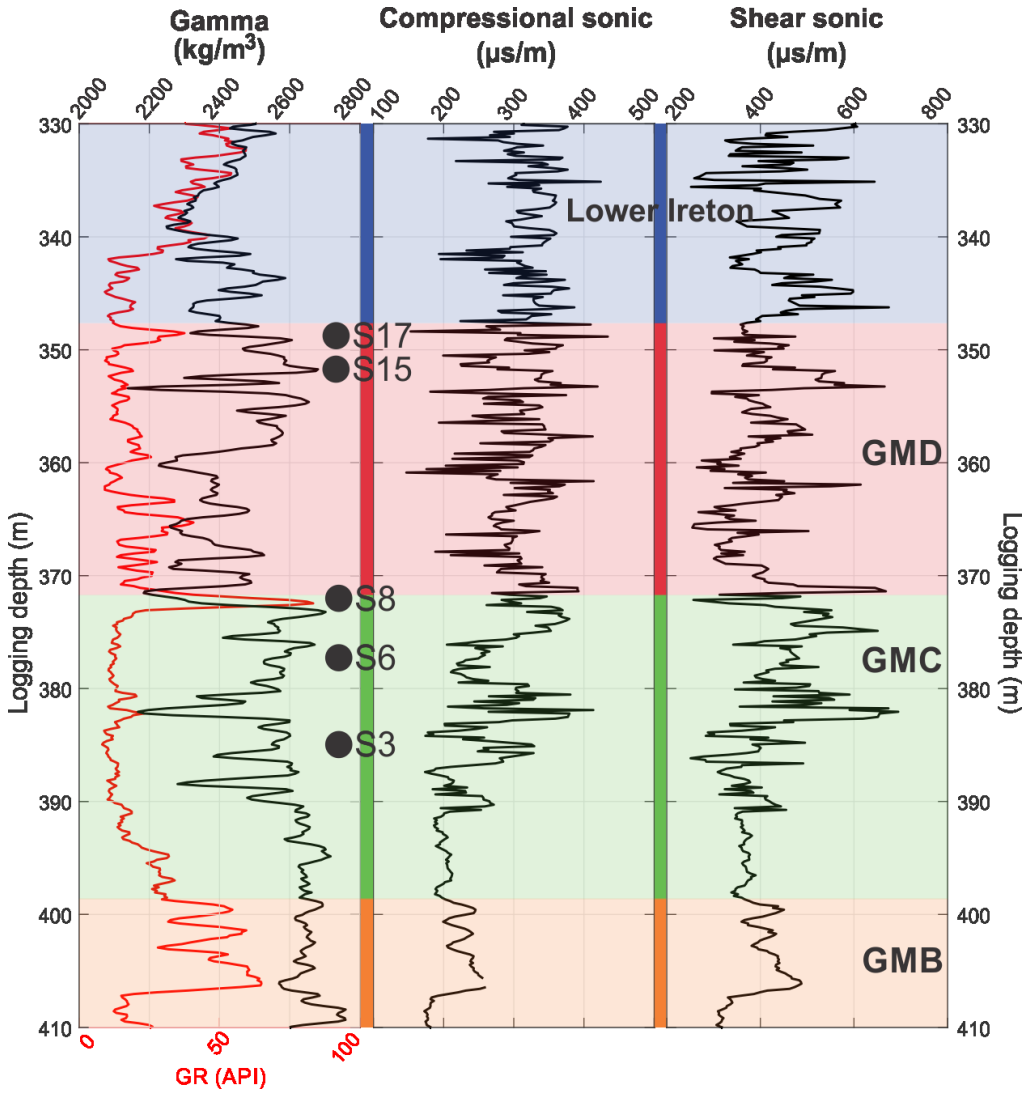

Figure 2.4: Gamma-ray, density, and sonic (monopole compressional and shear) well logs for well 100/01-07-85-19W4 highlighting the tops of major subdivisions of the Grosmont formation along with overlaying strata. Each unit is separated by marl layers often referred to as "shale breaks". Samples used for this study are showed at corresponding depths

2.3 Summary

In this chapter, a brief geological background of the Devonian-aged Grosmont Formation is provided. The Grosmont Formation is a bitumen-bearing carbonate platform complex spanning approximately 150 km in width and 500 km in length across north-central and north-eastern Alberta, Canada. The formation is discussed in terms of its stratigraphy, depositional setting, and diagenetic history.

The GMC and GMD (Units C and D) have the highest reservoir potential due to the large degree of karstification. Reservoir characteristics for these units are provided in detail.

3 Theoretical Background

3.1 Theory of Elasticity

To understand the propagation of seismic waves in the subsurface, we must first describe the details in which deformation occurs in an elastic body. Stress is defined as a measure of the internal forces in a material or in more relatable terms, the ratio of applied force to a certain cross-sectional area. Consider an infinitesimal cube under a static state of stress with the faces aligned with the axes of an orthogonal coordinate system. The components of stress acting on the surface of the cube are represented by the terms σ_{ij}, where the indices i and j represent one of the three axes in the Cartesian coordinate system.

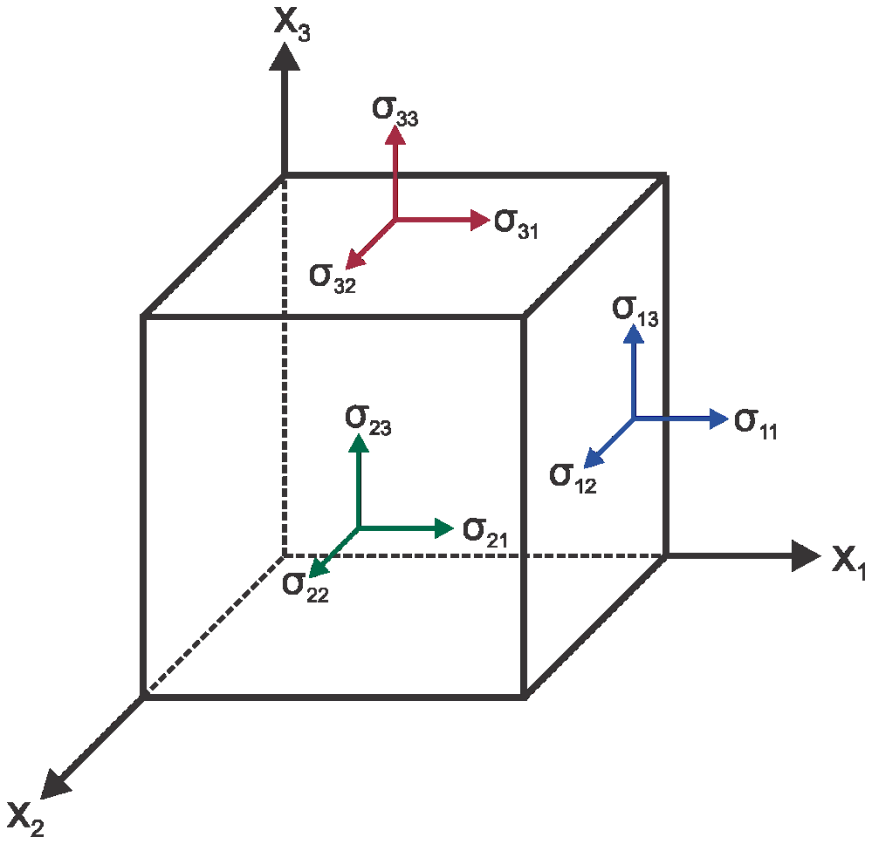

Figure 3.1: Visualization of stress components acting on the faces of an infinitesimal cube in an orthogonal coordinate system

Of the nine total components, three are considered to be normal stresses ($i = j$), those in which the stress is applied perpendicular to the surface. The other six components are shear stresses ($i \neq j$), where the stress is applied tangential to the surface.

When stress is applied to a given material, the deformation that occurs is known as the strain. Internal forces resist this strain and the material will tend to return to its original state as the external stress is removed. This resistive force is known as elasticity.

In an elastic medium, the relationship between stress and strain can be described by the generalized Hooke's Law, which states that the strain is linearly proportional to the stress applied to it:

$$\sigma_{ij} = C_{ijkl}\varepsilon_{kl}\,, \tag{3.1}$$

where σ and ε are second-order stress and strain tensors respectively, and C is a fourth-order elastic stiffness tensor. The indices i, j, k, l = 1, 2, 3 represents one of the three orthogonal axes. At a particular point, the elastic stiffness tensor C defines the elastic properties of a material with C_{ijkl} making up the 81 components of the tensor. The symmetric nature of the stress and strain tensors (Bos et al., 2004) imply the relations:

$$\sigma_{ij} = \sigma_{ji}\,, \tag{3.2}$$

and

$$\varepsilon_{kl} = \varepsilon_{lk}\,, \tag{3.3}$$

to allow the nine components of the stress and strain tensors to be reduced to six independent components. The same symmetric properties of the stress and strain tensors also imply the following relations:

$$C_{ijkl} = C_{jikl} = C_{ijlk} = C_{jilk}\,. \tag{3.4}$$

These symmetries, as well as the consideration of the energy conservation relations, which show that:

$$C_{ijkl} = C_{klij}\,, \tag{3.5}$$

allows the elastic stiffness tensor to be reduced to twenty-one independent components. With these vastly simplified version of the generalized Hooke's Law, we can now make us of the reduced Voigt notation, in which pairs of indices are placed with a single index

$$\begin{array}{ccc} ij,kl & & m,n \\ 11 & \rightarrow & 1 \\ 22 & \rightarrow & 2 \\ 33 & \rightarrow & 3 \\ 23 & \rightarrow & 4 \\ 13 & \rightarrow & 5 \\ 12 & \rightarrow & 6 \end{array}\,. \tag{3.6}$$

In the Voigt notation, Equation 3.1 is now reduced to

$$\sigma_m = C_{mn}\varepsilon_n\,, \tag{3.7}$$

and is written in its full tensor form as

$$\begin{bmatrix} \sigma_1 \\ \sigma_2 \\ \sigma_3 \\ \sigma_4 \\ \sigma_5 \\ \sigma_6 \end{bmatrix} = \begin{bmatrix} C_{11} & C_{12} & C_{13} & C_{14} & C_{15} & C_{16} \\ C_{12} & C_{22} & C_{23} & C_{24} & C_{25} & C_{26} \\ C_{13} & C_{23} & C_{33} & C_{34} & C_{35} & C_{36} \\ C_{14} & C_{24} & C_{34} & C_{44} & C_{45} & C_{46} \\ C_{15} & C_{25} & C_{35} & C_{45} & C_{55} & C_{56} \\ C_{16} & C_{26} & C_{36} & C_{46} & C_{56} & C_{66} \end{bmatrix} \begin{bmatrix} \varepsilon_1 \\ \varepsilon_2 \\ \varepsilon_3 \\ \varepsilon_4 \\ \varepsilon_5 \\ \varepsilon_6 \end{bmatrix}. \tag{3.8}$$

Conversely, Equation 3.7 can also be written as

$$\varepsilon_m = S_{mn}\sigma_n\,, \tag{3.9}$$

where the compliance matrix S_{mn} is the inverse of the elastic stiffness matrix with the form

$$S_{mn} = \begin{bmatrix} S_{11} & S_{12} & S_{13} & S_{14} & S_{15} & S_{16} \\ S_{12} & S_{22} & S_{23} & S_{24} & S_{25} & S_{26} \\ S_{13} & S_{23} & S_{33} & S_{34} & S_{35} & S_{36} \\ S_{14} & S_{24} & S_{34} & S_{44} & S_{45} & S_{46} \\ S_{15} & S_{25} & S_{35} & S_{45} & S_{55} & S_{56} \\ S_{16} & S_{26} & S_{36} & S_{46} & S_{56} & S_{66} \end{bmatrix}. \tag{3.10}$$

$$S = C^{-1} \tag{3.11}$$

3.2 Isotropic Media

The behavior of materials can be described by up to all 21 constants of the elastic stiffness tensor. With increasing symmetry, a material can be described with fewer independent elastic constants. The most basic case is an isotropic media, where the physical properties are independent of direction. In this case, the elastic stiffness tensor can be described using two independent elastic constants, assuming the form

$$C_{mn} = \begin{bmatrix} C_{33} & C_{33}-2C_{44} & C_{33}-2C_{44} & 0 & 0 & 0 \\ C_{33}-2C_{44} & C_{33} & C_{33}-2C_{44} & 0 & 0 & 0 \\ C_{33}-2C_{44} & C_{33}-2C_{44} & C_{33} & 0 & 0 & 0 \\ 0 & 0 & 0 & C_{44} & 0 & 0 \\ 0 & 0 & 0 & 0 & C_{44} & 0 \\ 0 & 0 & 0 & 0 & 0 & C_{44} \end{bmatrix}. \tag{3.12}$$

Where the elastic constants are related to the Lamé parameters λ and μ, as well as the bulk modulus K (Thomsen, 1986)

$$C_{33} = \lambda + 2\mu = K + \frac{4}{3}\mu\,, \tag{3.13}$$

and

$$C_{44} = \mu\,. \tag{3.14}$$

The bulk modulus K measures the material's resistance to uniform compression and is defined as the ratio of the infinitesimal pressure change to the resulting relative decrease in volume V

$$K = -V\frac{\partial P}{\partial V}\,, \tag{3.15}$$

where P is the applied pressure. The inverse of the bulk modulus is known as the compressibility

$$\beta = \frac{1}{K} = -\frac{1}{V}\frac{\partial V}{\partial P}\,. \tag{3.16}$$

The shear modulus μ is defined as the ratio of shear stress to shear strain

$$\mu = \frac{\sigma_{ij}}{\varepsilon_{ij}}, i \neq j\,. \tag{3.17}$$

3.3 Wave Propagation in Isotropic Media

The full derivation of the wave equation will be not presented here as the details are quite involved and can be found in many textbooks (Bhatia and Singh, 1986; Ikelle and Amundsen, 2005; Lay and Wallace, 1995). We will however, touch upon certain concepts and principles which will be relevant in later sections of this dissertation.

The wave equation in elastic media for a displacement u,

$$\rho\frac{\partial^2 u}{\partial t^2} = (\lambda + 2\mu)\nabla(\nabla\cdot\mu) - \mu\nabla\times(\nabla\times\mu)\,, \tag{3.18}$$

where u is given in terms of position x and time t. From here, it is possible to break down the structure of this equation through use of the Helmholtz decomposition theorem, which

states that any arbitrary vector field can be represented as the sum of its curl-free and divergence-free forms (Ikelle and Amundsen, 2005). The Helmholtz decomposition of the displacement field u is given as

$$u = \nabla\phi + \nabla \times \psi\,, \tag{3.19}$$

where ϕ is a curl-free scalar potential, representing a field with no shearing motion. In contrast, ψ is a divergence-free vector potential, representing a field with no volumetric change. These two fields represent the two types of body waves that can propagate through an elastic medium

Through substitution of Equation 3.19 into Equation 3.18, and the use of the identity $\left(\nabla \times \nabla \times \psi = -\nabla^2\psi\right)$, we obtain the following:

$$\nabla\left[(\lambda + 2\mu)\nabla^2\phi - \rho\frac{\partial^2\phi}{\partial t^2}\right] + \nabla \times \left[\mu\nabla^2\psi - \rho\frac{\partial^2\psi}{\partial t^2}\right] = 0\,. \tag{3.20}$$

One solution to this equation is obtained by setting the bracketed terms to zero, yielding two independent solutions to the scalar and vector potentials:

$$\frac{\partial^2\phi}{\partial t^2} = \frac{(\lambda + 2\mu)}{\rho}\nabla^2\phi\,, \tag{3.21}$$

$$\frac{\partial^2\psi}{\partial t^2} = \frac{\mu}{\rho}\nabla^2\psi\,. \tag{3.22}$$

By setting

$$\alpha = \sqrt{\frac{\lambda + 2\mu}{\rho}} \tag{3.23}$$

$$\beta = \sqrt{\frac{\mu}{\rho}}\,, \tag{3.24}$$

we notice Equations X and X has the form of the scalar wave equation for ϕ and the vector wave equation for ψ (Lay and Wallace, 1995). Here, the term α corresponds to the wave velocity for the P-wave (also known as primary, pressure, longitudinal, and compressional waves), and β corresponds to the wave velocity for the S-wave (also known as secondary, shear, and transverse waves).

3.4 Viscoelasticity

Unlike the purely elastic mediums discussed thus far, viscoelastic materials exhibit both elastic and viscous characteristics when undergoing deformation. When a shear stress is applied to a viscous material, strain accumulates as a function of time

$$\sigma_{ij} = \eta \frac{\partial \varepsilon_{ij}}{\partial t}, i \neq j\,, \tag{3.25}$$

where η is the dynamic shear viscosity of the material. On the other hand, purely elastic materials have an instantaneous response to applied stress, that is to say, there is no time dependency on the stress-strain relationship. In reality, most materials are unlikely to exhibit a purely elastic or viscous response, but a combination of the two. These types of materials are considered to be 'viscoelastic'.

Some typical properties of viscoelastic materials that are relevant to our study are provided in Lakes (2009) and summarized here:

1. *If the stress is held constant, the strain increases with time (creep)*: In Figure 3.2, the strain response is shown for elastic, viscous, and viscoelastic materials for an applied step stress. However, note that in reality, no load can be physically applied instantaneously.

   As a step load of σ_0 is applied, the elastic response is instantaneous as the stress-strain relationship for elastic materials is time independent. For viscous materials, the strain will accumulate during the loading process, and will stop at the time of unloading. The viscoelastic response will share characteristics of both curves.

   At the time of loading, the viscoelastic material will gradually strain with time; this phenomenon is called 'creep'. When the stress is unloaded, the elastic behaviour of the material causes the strain to instantaneously decrease, after which the viscous response of the material takes over, as evident by the decreasing strain with time. Due to the viscous nature of deformation, the strain of the viscoelastic material never fully recovers.

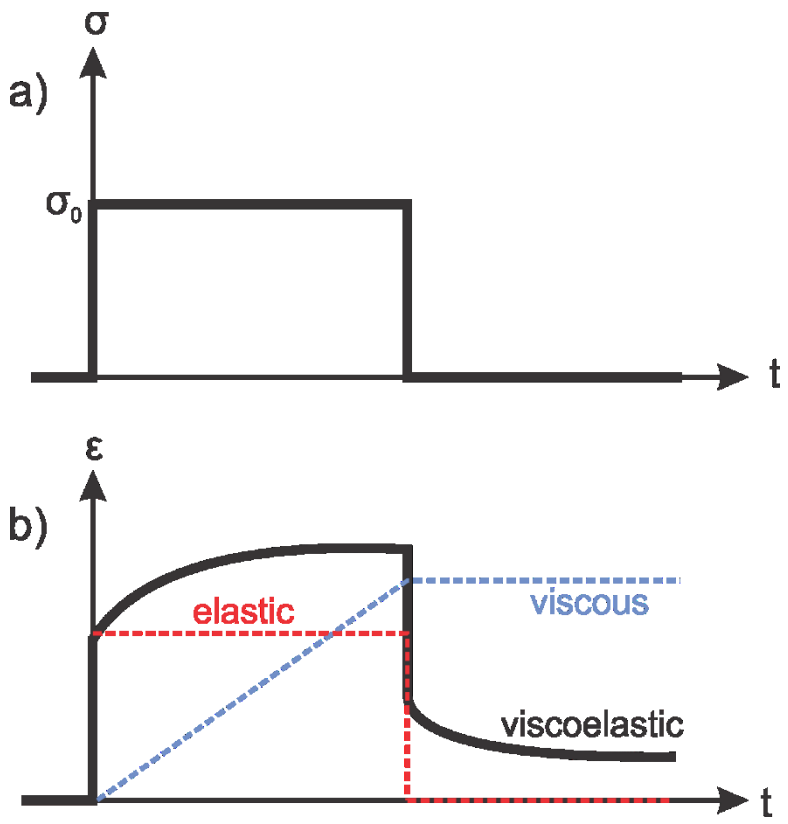

Figure 3.2: Creep and recovery response - a) Step stress of magnitude σ_0 as a function of time. b) Strain response with time to applied strain for elastic, viscous, and viscoelastic materials. Figure modified from Lakes (2009)

2. *If the strain is held constant, the stress decreases with time (relaxation)*: In Figure 3.3, the stress response is shown for a viscoelastic material held at constant strain. At the time when the strain of the material is induced to a magnitude ε_0, the stress will instantaneously increase due to the elastic response of the material. With time, the stress decreases to keep the strain level at constant value. At the time when the step strain returns to zero, the stress will elastically change directions to recover the strain. Immediately after, the viscous response takes over, governing the gradual return to zero stress. However, due to the viscous nature of deformation, a residual is seen in the stress curve.

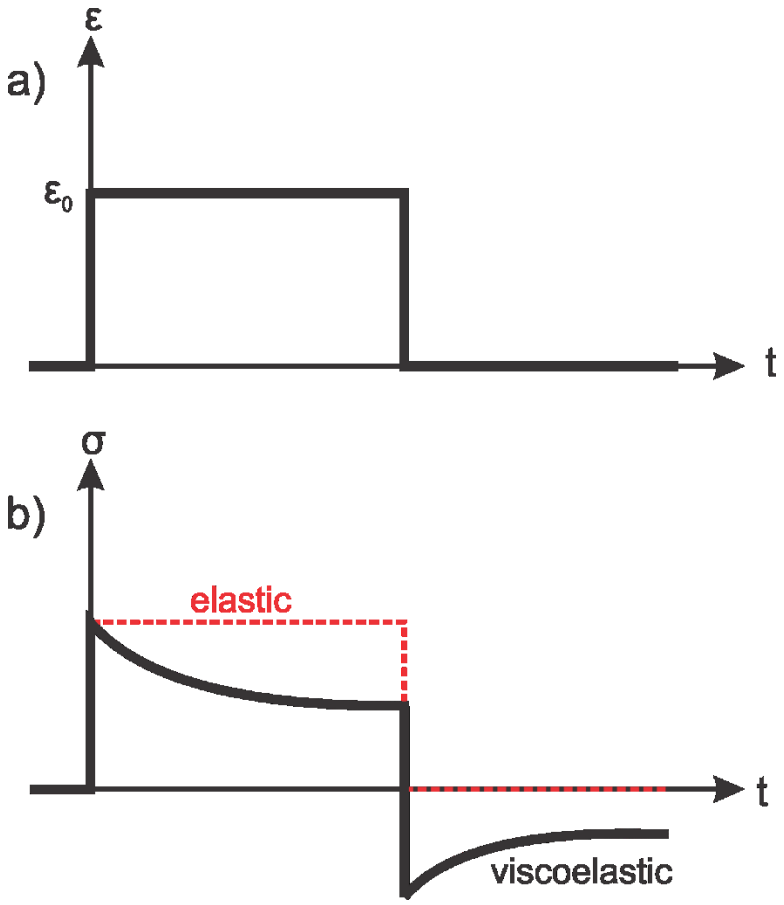

Figure 3.3: Stress relaxation and recovery response – a) Step strain of magnitude ε_0 as a function of time. b) Stress response with time as material is held at constant strain. Figure modified from Lakes (2009)

3. *If cyclic loading is applied, hysteresis (a phase lag) occurs, leading to a dissipation of mechanical energy*: Suppose the stress is varying sinusoidally with time t and angular frequency ω, given by

$$\sigma(t) = \sigma_0 \sin(2\pi\omega t) \quad . \tag{3.26}$$

The strain response of the applied stress for a linearly viscoelastic material will also be sinusoidal in time, however, it will lag the stress by a phase angle δ (also known as the loss angle)

$$\varepsilon(t) = \varepsilon_0 \sin(2\pi\omega t - \delta) \; . \tag{3.27}$$

With both strain and stress responses varying sinsoidally at the same period $T = 1/\omega$, the loss angle is related to the time lag Δt between the two responses by

$$\delta = \frac{2\pi\Delta t}{T} \, . \tag{3.28}$$

The loss angle δ is a dimensionless measure of the viscoelastic damping of the material (Lakes, 2009). In purely elastic material, the stress and strain are completely in phase with a loss angle of zero. In contrast, for purely viscous behaviour, the strain is out of phase with stress by 90 degrees. Viscoelastic materials will have a loss angle somewhere in between tese two values. The tangent of this parameter is called the loss tangent

$$\tan\delta = \frac{C''}{C'} \, , \tag{3.29}$$

where C' and C'' are the real and imaginary components, respectively, of the dynamic stiffness C^*

$$C^* = C' + iC'' = \frac{\sigma(t)}{\varepsilon(t)} \, . \tag{3.30}$$

The dynamic stiffness C^* is the viscoelastic equivalent to the stiffness modulus C that was used to relate stress and strain in perfectly elastic materials. For purely elastic behaviour, this parameter is a real number, but for viscoelastic behaviour, this number is complex, due to the phase lag between the stress and strain. The real component C' of the dynamic stiffness is commonly referred to as the *storage* modulus while the imaginary component C'', is called the *loss* modulus. For a loss tangent $\tan\delta = 0$, this would be considered an elastic solid.

4. *The effective stiffness depends on the rate of application of the load*: Viscoelastic materials exhibit time and frequency dependency and as such, the complex dynamic stiffness is

dependent on the rate of loading. This property also means that wave propagation speed is inherently dependent on the frequency of the source.

5. *Acoustic waves experience attenuation*: Consider the one-dimensional problem of wave propagation along a thin rod of linearly viscoelastic material. The wave equation and corresponding solution is given as

$$\frac{\partial^2 u}{\partial t^2} = \frac{E^*}{\rho}\frac{\partial^2 u}{\partial x^2}\ , \tag{3.31}$$

and

$$u(x,t) = u_0 \exp\left(i\omega\left(\frac{x}{v} - t\right)\right)\exp\left(-x\frac{\omega}{2v}tan\,\delta\right)\ , \tag{3.32}$$

respectively, where v is the wave velocity. In Equation 3.28, the left exponential describes the phase propagation of the wave, whereas the right exponential is completely real, and implies a decrease of wave amplitude with distance x. This decrease is known as attenuation, where for a linearly viscoelastic material, the attenuation coefficient α is defined as:

$$\alpha = \frac{\omega}{v}\tan\frac{\delta}{2}\ . \tag{3.33}$$

It is important to note that an isotropic material will have two independent stiffness constants, therefore two independent attenuation values.

There are many models that attempt to simulate the response of viscoelastic behaviours under varying loading conditions. These models, which include the Maxwell and Kelvin-Voigt models, simulate the elastic and viscous components as linear combinations of springs and dashpots, respectively.

3.5 Maxwell and Kelvin-Voigt models

In these models, the elastic and viscous behaviour can be represented by springs and dashpots, respectively - as such, they are commonly referred to as "spring-dashpot" models.

The spring, analogous to an object used to store mechanical energy, is used to represent the elastic component, obeying Hooke's law as

$$\sigma = C\varepsilon \,, \tag{3.34}$$

where σ is the stress, E is the Young's modulus, and ε is the strain. This elastic component (Figure 3.4a) provides the instantaneous and reversible material deformation in linear viscoelastic models.

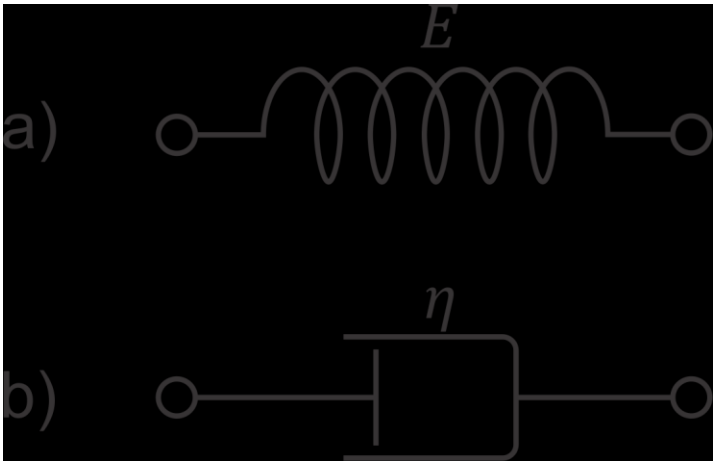

Figure 3.4: a) Hookean spring representing the elastic and b) Newtonian dashpot representing the viscous response

Like-wise, the dashpot (Figure 3.4b) represents the viscous response of said models and relates the applied stress and strain using the relation

$$\sigma = \eta \frac{d\varepsilon}{dt} \,, \tag{3.35}$$

where η is the shear viscosity.

Two simple configurations used to simulate the response of viscoelastic systems are the "Maxwell" and "Kelvin-Voigt" models. The Maxwell model (Figure 3.5) is represented by a perfectly elastic spring and perfectly viscous dashpot connected in series (much like an

electrical circuit). In this system, the stress is applied equally on the spring and dashpot while the sum of strain on each component is equal to the total strain

$$\sigma = \sigma_s = \sigma_d \,, \tag{3.36}$$

$$\varepsilon = \varepsilon_s + \varepsilon_d \,, \tag{3.37}$$

where the subscripts s and d represents the spring and dashpot, respectively. For the Maxwell model, the stress and strain relationship is given by Christensen (1982) as

$$\sigma + \frac{\eta}{E}\frac{d\sigma(t)}{dt} = \eta\frac{d\varepsilon(t)}{dt} \,. \tag{3.38}$$

Figure 3.5: The Maxwell viscoelastic model, with spring (elastic component) and dashpot (viscous component) connected in series

The Maxwell model predicts that stress decays exponentially with time while defining the term relaxation time τ

$$\tau = \frac{\eta}{E} \,, \tag{3.39}$$

as the time needed for the stress to decrease to $1/e$ of the initial magnitude. However, one limitation of this model is its failure to describe the phenomenon of creep (time-dependent strain relaxation under constant stress) properly.

In the Kelvin-Voigt model (Figure 3.6), the spring and dashpot are connected in parallel. In this configuration, the sum of the stress applied on the spring and dashpot is equal to the total stress while the strain of each component are equal following the relations

$$\sigma = \sigma_s + \sigma_d \,, \tag{3.40}$$

and

$$\varepsilon = \varepsilon_s = \varepsilon_d \,. \tag{3.41}$$

The constitutive equation governing the relationship between stress and strain is given as

$$\sigma = E\varepsilon(t) + \eta \frac{d\varepsilon(t)}{dt} \,. \tag{3.42}$$

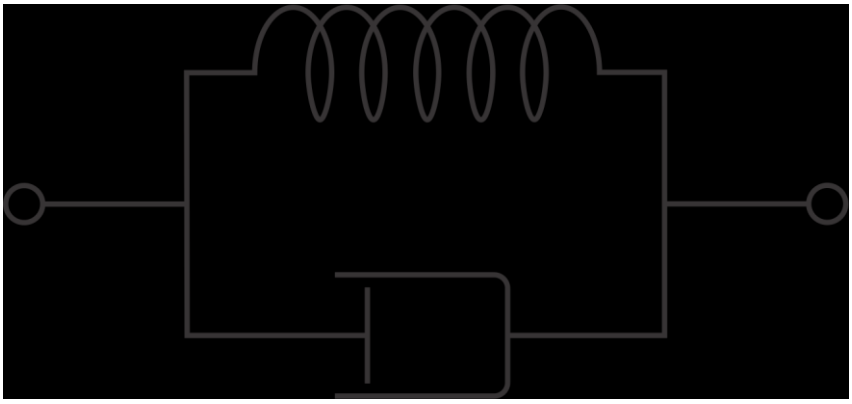

Figure 3.6: The Kelvin-Voigt viscoelastic model, with spring (elastic component) and dashpot (viscous component) connected in parallel

In contrast to the Maxwell model, the Kelvin-Voigt material is effective at predicting creep, however, it is unable to describe the relaxation response.

3.6 Poroelastic and Effective Medium Theories

Up to this point in this section, the theoretical background for wave propagation had been given assuming a homogeneous or continuous medium. However, actual rock material is normally porous, which is to say that the material is made up of a solid matrix and a void volume containing a fluid. The elastic properties that govern the propagation of waves through such a medium are therefore directly influenced by the properties of the solid and fluid constituents, as well as their interaction with one another. To complicate things even further, the solid matrix of the rock itself is not homogeneous, but is a composite material made of

different mineral grains, often with varying properties. The elastic properties of this material can be quite complicated, with developed theories often providing approximations instead of exact calculations. This field of study is called 'effective medium theory'.

Here, we will review and discuss some of the most common theoretical rock-fluid interaction models used within the field of geophysics.

3.7 Gassmann's Equation

One of the most widely-used fluid substitution models in exploration geophysics is Gassmann's equation (Smith et al., 2003). The model, popular due to its simplistic form and presumed application to data in the seismic frequency range (5 – 200 Hz), is commonly used to relate the effective bulk modulus of the rock to its frame and fluid properties. In Gassmann's formation, the bulk modulus of a saturated rock K_{sat}, is related to the bulk modulus of the rock frame K_{dry}, constituent minerals making up the frame K_0, and fluid K_{fl}, as well as the porosity ϕ of the rock:

$$\frac{K_{\mathrm{sat}}}{K_0 - K_{\mathrm{sat}}} = \frac{K_{\mathrm{dry}}}{K_0 - K_{\mathrm{dry}}} + \frac{K_{\mathrm{fl}}}{\phi(K_0 - K_{\mathrm{fl}})}\,, \tag{3.43}$$

and most commonly rearranged as

$$K_{\mathrm{sat}} = K_{\mathrm{dry}} + \frac{\left(1 - \frac{K_{\mathrm{dry}}}{K_0}\right)^2}{\frac{\phi}{K_{\mathrm{fl}}} + \frac{1-\phi}{K_0} + \frac{K_{\mathrm{dry}}}{{K_0}^2}}\,. \tag{3.44}$$

The saturated shear modulus μ_{sat} is considered to be equal to the dry shear modulus μ_{dry}:

$$\mu_{\mathrm{sat}} = \mu_{\mathrm{dry}}\,, \tag{3.45}$$

as Gassmann's formulation assumes that the pore fluid is unable to sustain shear forces and thus does not affect the shear modulus of the rock. However, this assumption is violated in

applications of heavy oil saturated rocks due to the non-zero shear modulus of the fluid μ_{fl} at low temperatures.

1) Estimation of fluid elastic moduli

The elastic properties of the fluid residing the pore space can greatly influence the overall properties of the rock. In fluid substitution problems, it is important to have information of the about density, bulk modulus, and in the case of viscous fluids, the shear modulus of the presently saturating fluid as well as those of the new fluid we wish to substitute. These properties are typically directly measured using laboratory methods or calculated from empirical relationships (Batzle et al., 2006; Batzle and Wang, 1992), often using the relation for the adiabatic bulk modulus

$$K_{\mathrm{fl}} = \rho_{\mathrm{fl}} {V_{p\mathrm{fl}}}^2 , \tag{3.46}$$

where ρ_{fl} and $V_{p\mathrm{fl}}$ are the fluid density and P-wave velocity, respectively. In instances where the fluid has a non-negligible shear modulus, sustaining S-waves with velocity $V_{s\mathrm{fl}}$, the relationship becomes

$$K_{\mathrm{fl}} = \rho_{\mathrm{fl}} ({V_{p\mathrm{fl}}}^2 - \frac{4}{3} {V_{s\mathrm{fl}}}^2) . \tag{3.47}$$

In the case of most reservoir rocks, the residing pore fluid is typically composed of a mixture of different fluid phases. The overall pore fluid bulk properties can be calculated using the Reuss iso-stress model:

$$K_{\mathrm{fl}} = \left[\sum_{i=1}^{n} \frac{f_i}{K_{\mathrm{fl}i}} \right]^{-1} , \tag{3.48}$$

where f_i and $K_{\mathrm{fl}i}$ are the volume fractions and bulk moduli of the constituent fluid phases, respectively. Similarly, the end member fluid bulk density for a mixture can be calculated using

$$\rho_{\mathrm{fl}} = \sum_{i=1}^{n} f_i \rho_{\mathrm{fl}i} \ , \tag{3.49}$$

where $\rho_{\mathrm{fl}i}$ is the bulk density of the individual fluid phases.

2) Estimation of dry frame elastic moduli

The dry frame elastic moduli K_{dry} and μ_{dry} are relatively simple to calculate for ultrasonic studies as they can be directly related to the P- and S- wave velocities of the porous frame of the rock devoid of any pore fluids, however special considerations should be taken to ensure the measurements are conducted in proper conditions. Cadoret and Poirier (1993) showed that from an initial dry state, the measured P-wave velocity of limestones dropped by approximately 4% with introduction of moisture. This velocity drop, also observed in measurements of clastic rocks, has been attributed to the softening of cements, clay swelling, and other surface effects (Mavko et al., 2009). Therefore, precautions should be taken in removing pore fluids from the rock samples to prevent the sample from becoming "too dry".

3) Estimation of grain elastic moduli

The parameter K_0 is the bulk modulus of the mineral matrix, which is typically composed of a mixture of grains. If one wishes to estimate the effective elastic moduli of a mixture of grains, we need to know: 1) the volume fraction of each constituent phase, 2) the elastic moduli of each phase, and 3) the geometric details of how each phase is oriented with respect to each other (Mavko et al., 2009). The constituent minerals and their volume fractions can be determined the laboratory through analysis of thin-sections or X-ray diffraction / fluorescence methods (XRD/XRF). Upon identification of constituent minerals, their elastic properties can found from literature such as Bass (1995). However, detailed knowledge of the grain geometry is difficult to obtain and without such information, we can only at-most, specify the upper and lower bounds for the effective moduli.

The Voigt (1907) average (also known as the iso-strain average), is the upper bound of the effective bulk modulus K_V and is given by

$$K_V = \sum_{i=1}^{n} f_i K_i \ , \tag{3.50}$$

where f_i and K_i are the volume fractions and bulk modulus of the constituent mineral phases, respectively. The lower bound K_R corresponds to the Reuss (1929) average (also known as the iso-stress average) and calculated using

$$K_R = \left[\sum_{i=1}^{n} \frac{f_i}{K_i} \right]^{-1} \ . \tag{3.51}$$

From the Voigt and Reuss averages calculated, the effective bulk modulus of the mixture of grains can be estimated using the Voigt-Reuss-Hill approximation (Hill, 1952), which is the simple arithmetic average of the two bounds:

$$K_{VRH} = \frac{1}{2}(K_V + K_R) \, . \tag{3.52}$$

Alternatively, the Hashin-Shtrikman (HS) averaging may be used with the Hashin and Shtrikman (1963) bounds.

Several other assumptions made in the Gassmann model are:

1. The rock is macroscopically homogeneous and isotropic
2. The pore space is completely connected such that fluids can move freely within the rock
3. The frame of the rock is composed of minerals with the same bulk and shear moduli
4. There are no interactions between the rock frame and saturating pore fluid
5. Only valid at low enough frequencies such that pore pressures can be equilibrated over a length scale much greater than a pore dimension and much less than the wavelength of the passing wave (Smith et al., 2003)

The last point is of particular significance for the application of this model in heavy oil saturated rocks. The relaxation time of the rock is heavily influenced by the viscosity of the saturating fluid and thus potentially violating a key assumption of Gassmann's equation. Another potential violation is the assumption of free-flowing pore fluids as the variation of permeability in the Grosmont formation is relatively large due to the complex nature of the reservoir. As such, some parts of the formation may contain rock material with isolated pores or pores connected with small pore throats, thus restricting the flow of fluids.

As previously mentioned, Gassmann's formulation is only assumed to be valid for sufficiently low frequencies. Therefore, for rocks which show significant velocity dispersion, such as those saturated with viscous fluids, fluid substitution analysis should employ the use of Biot's theory, which extends Gassmann's formulation to the full frequency range.

3.8 Biot's Formulation

The theory introduced by Biot (1956a, 1956b) describes a general framework for the propagation of elastic waves in a porous, fluid-filled medium, extended to the full frequency range. Biot's formulation considers the medium to be comprised of three components: the porous solid frame, the solid matrix of grains which form the frame, and the fluid saturating the pore space. In contrast to Gassmann's formulation, Biot's theory incorporates viscous and inertial interactions between the pore fluid and solid matrix of the rock to predict the frequency-dependent velocities of a saturated porous medium. This framework was developed with several assumptions (van Dalen, 2013; Yam, 2011) in mind:

1) Fluid phase is fully connected within the porous medium. Disconnected pore space is considered as part of the solid matrix
2) The solid and fluid phases are assumed isotropic and homogeneous
3) The pore fluid is Newtonian
4) The pore space is fully saturated at all times

5) Thermoelastic and chemical reaction effects are absent
6) Displacements for solid and fluid phases are small

Here, only the application, implementation, and limitations of Biot's theory is discussed, however, an extensive derivation of the formulation can be found in Bouzidi (2003).

At the low frequency limit, Biot's theory reduces to Gassmann's equations, however, at the high frequency limit, his formulation predicts the existence of both "fast" and "slow" compressional waves, due to the inclusion of inertial interactions between the solid and fluid phases. In the notation of Johnson and Plona (1982), the fast and slow P-wave velocities, and S-wave velocity at the high frequency limit are given as

$$V_P(\text{fast, slow}) = \left[\frac{\Delta \pm [\Delta^2 - 4(\rho_{11}\rho_{22} - {\rho_{12}}^2)(PR - Q^2)]^{1/2}}{2(\rho_{11}\rho_{22} - {\rho_{12}}^2)}\right]^{1/2}, \tag{3.53}$$

$$V_S = \left(\frac{\mu_{\text{fr}}}{\rho - \phi\rho_{\text{fl}}\alpha^{-1}}\right)^{1/2}, \tag{3.54}$$

$$\Delta = P\rho_{22} + R\rho_{11} - 2Q\rho_{12}, \tag{3.55}$$

$$P = \frac{(1-\phi)\left(1 - \phi - \frac{K_{\text{fr}}}{K_0}\right)K_0 + \frac{\phi K_0 K_{\text{fr}}}{K_{\text{fl}}}}{1 - \phi - \frac{K_{\text{fr}}}{K_0} + \frac{\phi K_0}{K_{\text{fl}}}} + \frac{4}{3}\mu_{\text{fr}}, \tag{3.56}$$

$$Q = \frac{\left(1 - \phi - \frac{K_{\text{fr}}}{K_0}\right)\phi K_0}{1 - \phi - \frac{K_{\text{fr}}}{K_0} + \frac{\phi K_0}{K_{\text{fl}}}}, \tag{3.57}$$

$$R = \frac{\phi^2 K_0}{1 - \phi - \frac{K_{\text{fr}}}{K_0} + \frac{\phi K_0}{K_{\text{fl}}}}, \tag{3.58}$$

where P, Q, and R are generalized elastic coefficients which can be related to related to the bulk modulus of the fluid K_{fl}, and solid matrix K_0. The bulk modulus of the solid frame K_{fr}, and shear modulus of the solid frame μ_{fr}, equal to either the dry frame moduli, or the high-frequency, unrelaxed, "wet-frame" moduli (Mavko et al., 2009). The density terms ρ_{ij} are related to the density of the solid matrix ρ_0 and fluid ρ_{fl} by the relationships

$$\rho_{11} = (1-\phi)\rho_0 - (1-\alpha)\phi\rho_{\mathrm{fl}}\,, \tag{3.59}$$

$$\rho_{22} = \alpha\phi\rho_{\mathrm{fl}}\,, \tag{3.60}$$

$$\rho_{12} = (1-\alpha)\phi\rho_{\mathrm{fl}}\,, \tag{3.61}$$

$$\rho = \rho_0(1-\phi) + \rho_{\mathrm{fl}}\phi\,. \tag{3.62}$$

The parameter α, known as the tortuosity, is a geometrical factor that describes the complexity of the structure of a pore space. In the context of porous media, tortuosity is the ratio of the average length of the geometric flow paths through the medium to the straight line path (Ghanbarian et al., 2013), and has a value that is greater than or equal to 1. This parameter is independent of solid or fluid densities with Berryman (1981) showing that it can be estimated using the following relation

$$\alpha = 1 - r\left(1 - \frac{1}{\phi}\right)\,. \tag{3.63}$$

where $r = \frac{1}{2}$ for spherical pore shapes, and lies between 0 and 1 for other ellipsoids. Lamb (1945) provides a table of values for r as a function of aspect ratio. The physical meaning of ρ_{11} as described by Biot is that of the total effective density of the solid frame is moving in the fluid. The term ρ_{12} describes the inertial drag that the fluid exerts on the solid as the latter is accelerated relative to the former and vice versa (Johnson and Plona, 1982).

3.9 Summary

In this chapter, the basics of elastic wave propagation is first described through a brief review of the theory of elasticity. In this context, we review Hooke's Law, which describes the behavior of a material where the stress and strain are linearly proportional to each other. Here, we show that for a perfectly elastic isotropic medium, the elastic stiffness tensor can be reduced from 81 elastic constants to 2 independent constants. Consequently, P- and S-wave velocities can be defined in terms of these constants and the bulk density of the material. The concept of viscoelasticity is next introduced and discussed in the context of wave propagation. Following this section, Maxwell and Kelvin-Voigt models are briefly reviewed as two simple constitutive models for linear viscoelasticity.

Next, the concepts of poroelastic theory are briefly discussed along with independent reviews of Gassmann and Biot's formulations. Gassmann's equation is a commonly-used fluid substitution model that is used to relate the properties of a fluid-saturated rock in terms of the porosity and the properties of the dry frame, grains, and fluids. The formulation of Gassmann is based on several assumptions which are discussed here in detail along with its implications for modelling heavy oil saturated rocks. One particular limitation of Gassmann's equation is its restriction to low frequency applications. In contrast, Biot's formulation is applicable for the full frequency range.

4 Methodology

This study involves the determination of velocity and their associated dynamic elastic moduli of our samples at ultrasonic frequency. There are several established techniques that are commonly employed for this task, which includes the use of pulse transmission, pulse echo, and forced oscillation / resonant bar experiments. For this project, we use the pulse transmission method, a technique that has been used extensively in the study of physical properties of rocks (Birch, 1961, 1960; Rabbani et al., 2016; Tosaya and Nur, 1982; Wang and Nur, 1990). The common usage of the pulse transmission method in rock physics studies is attributed to its relatively easy setup and adaptability for use under a variety of experimental conditions. Details of the pulse transmission method, electronic setup, sample preparation steps, and measurement workflow are first provided in this chapter. Following this are the details outlining the methods used in the characterization of the sample material.

4.1 Pulse Transmission Method

Conceptually, the basic mechanics of the pulse transmission method are very simple. The premise of this technique is to place a sample between a source and receiver ultrasonic transducer. As the source transducer is excited, mechanical vibrations propagate through the sample as ultrasonic waves. The arrival of the wave at the other end of the sample is then detected and recorded by the receiver transducer. From analysis of the waveform, transit times can be picked and the wave velocity of the sample can then be calculated from the simple relation

$$V = \frac{d}{t} \ , \tag{4.1}$$

where d is the displacement length between ultrasonic transducers, and t is the transit time of the propagating wave.

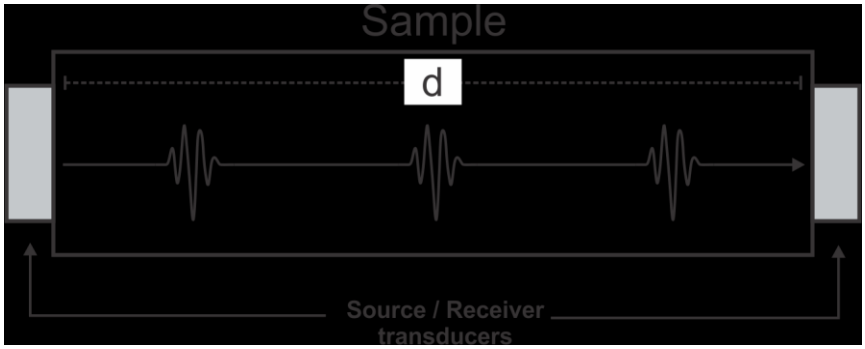

Figure 4.1: Simplified illustration of Pulse Transmission Method basics. Wavelets denote the wave path through the sample

As previously mentioned, a significant advantage of the pulse transmission method is the versatility of the technique under varying experimental conditions. However, for its application in high temperature and pressure experiments such as the one in this study, careful consideration must be taken in the construction of the ultrasonic transducers.

4.1.1 Piezoelectric Elements

In a general context, transducers refer to any device that converts one form of energy to another. In the case of piezoelectric transducers, the devices convert mechanical vibrations into an electric signal and vice versa. In this section, we provide details on the materials and assembly of the transducers used in this study. The active component of the transducer is the piezoelectric element that converts an electric potential into mechanical vibrations (and vice versa) through the piezoelectric effect. There are many materials, both naturally occurring and synthetic, that exhibit this effect and as such, there are many different types of piezoelectric elements are that manufactured for use in specific environments.

The most common type of piezoelectric element in use today, and the one used in most applications in the University of Alberta Experimental Geophysics Group, are made from lead zirconate titanate (PZT). The elements are made by combining the fine powders of each ceramic material component, mixed with chemical binders. They are then pressed into the

desired shapes and then fired in a industrial kiln to a specific temperature and time ("Piezoelectricity," 2016). After cooling, elements are trimmed to specifications and electrodes are applied. Elements are then polarized by heating them up above the Curie temperature within an applied electric field. These PZT ceramic elements are physically strong, exhibit high piezoelectric coefficients, and are relatively inexpensive to manufacture in comparison to single-crystal elements.

However, the working stability of ceramic elements are more sensitive to high temperatures (Islam, 2018). This proves problematic with in our experiment as the piezoelectric transducers will have to be exposed to the high temperature and pressure conditions required for this study. Early tests of ultrasonic transducers made with PZT ceramic elements showed significant reduction in shear wave propagation energy at temperatures of 70°C and higher. This effect, in combination with the highly attenuative properties of the bitumen-saturated rocks, resulted in the acquisition of lower quality shear-wave data at high temperatures.

Table 4-1. Piezoelectric constants of laboratory transducer elements

	Piezoelectric charge constant (10^{-12} C/N)		
Material description	**d_{15}**	**d_{31}**	**d_{33}**
APC 842 (PZT Ceramic)[1]			300
APC 850 (PZT Ceramic)[1]	590	-175	-0.85
BPO ($LiNbO_3$ Single-crystal) [2]	69	-1	6

1. Values retrieved from "Physical and Piezoelectric Properties of APC Materials" (2016)
2. Values retrieved from "Lithium Niobate - Physical Properties" (2018)

It was presumed that the reduction in s-wave source energy may be attributed to the temperature dependence of the element's piezoelectric charge constant. This constant relates the mechanical strain that is produced when a piezoelectric material is subjected to an electric field (induced polarization of material). Table 4-1 shows the manufacturer provided piezoelectric constants of interest for two PZT ceramic elements as well as for a lithium niobate single crystal. As piezoelectric materials are generally considered to be anisotropic, their

corresponding electromechanical properties are accordingly described in tensor notation. Each constant has two subscripts which indicates the directions of induced polarization and produced mechanical strain, following the coordinate system described in Figure 4.2. The direction of positive polarization established during the manufacturing process is commonly made to coincide with axis 3. The higher the value of the charge constant, the more strain is produced for a given electric potential, and larger energy ultrasonic waves are generated from the source transducer. The piezoelectric shear constant d_{15} for the PZT ceramic material is approximately 8 times higher than for the lithium niobate single-crystal, however, the temperature dependence for the lithium niobate element is much weaker (Bukhari et al., 2014).

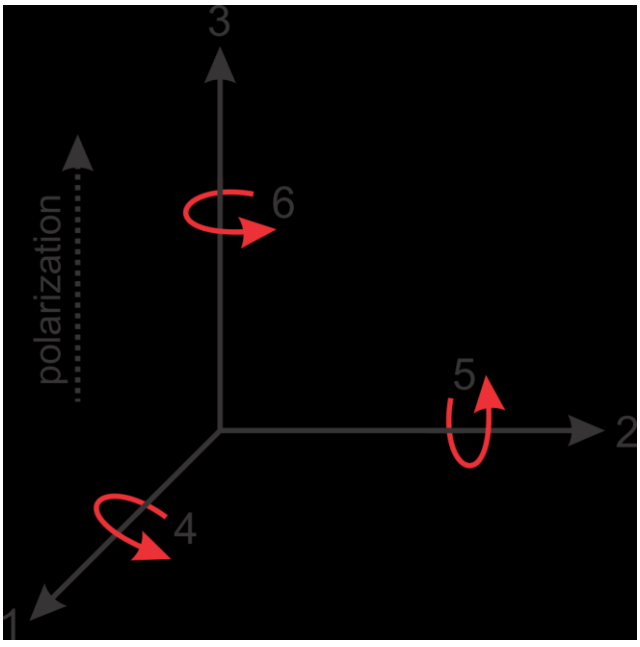

Figure 4.2: Orthogonal coordinate system to describe properties of polarized piezoelectric materials. Positive polarization direction coincides with axis 3.

Another possible explanation for substantial decrease in s-wave source energy is the temperature dependent loss of rigidity in the adhesive used for bonding the piezoelectric element to the aluminum buffer. At high temperatures, this effect could drastically reduce coupling between these two components, effectively reducing the energy of the transmitted ultrasonic wave. For experiments where high temperature conditions are not expected, silver conductive epoxy is typically used for bonding. According to the manufacturer, this epoxy has a constant service temperature ranging from -55°C to 150°C, however, it is unknown which physical properties are considered in the determination of these values. Another alternative adhesive is a specialized epoxy commonly used to bond metals together in marine settings. This marine epoxy cures to a greater hardness than the silver conductive epoxy and has a higher max operating temperature of 315°C.

To systematically test these configurations, a simple pulse echo experiment was conducted to determine the effectiveness of the piezoelectric element and adhesives at high temperatures. Three sets of piezoelectric elements and adhesives were bonded directly to a 25 mm (1-inch) thick aluminum plate:

1) APC 850 PZT Ceramic with MG Chemicals 8331 Silver Conductive Epoxy

2) APC 850 PZT Ceramic with J-B Marine Weld Epoxy

3) Boston Piezo Optics $LiNbO_3$ Single-crystal with J-B Marine Weld Epoxy

Both piezoelectric elements were transversely polarized (s-mode) and had a resonance frequency of 1 MHz. This plate was then placed into an oven where the temperature was varied from 23°C to 110°C. At a constant excitation voltage, pulse-echo signals were recorded as they reflected off the interface between the air and the other side of the aluminum plate. For the 3 element-adhesive sets, RMS amplitudes and Normalized RMS amplitudes (normalized by its max value) were calculated and plotted with respect to operating temperature.

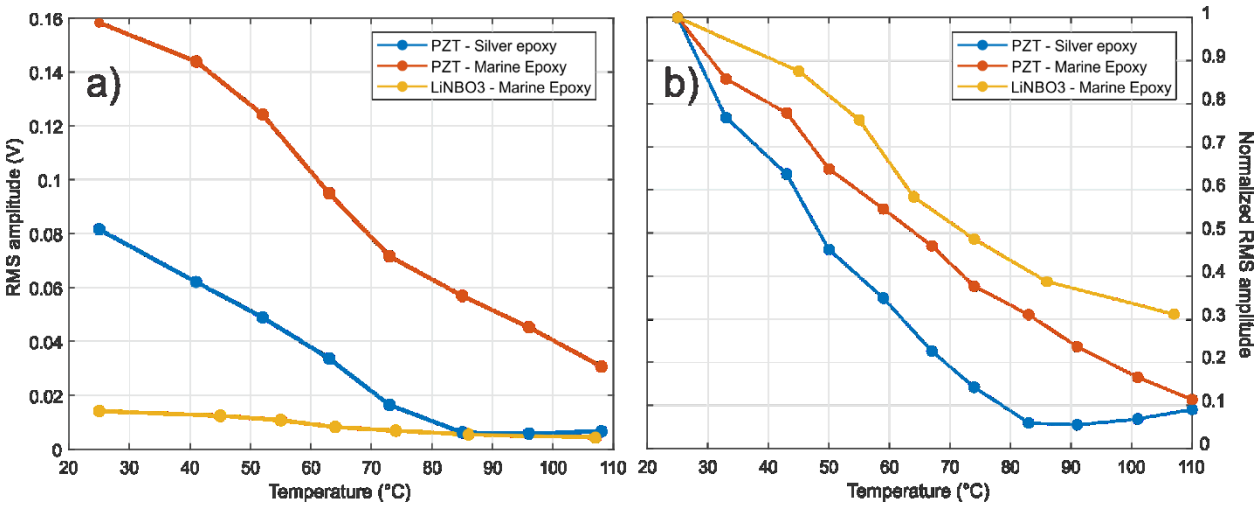

Figure 4.3: Plots of a) RMS amplitude and b) RMS amplitude normalized by its max value for 3 sets of piezoelectric elements and adhesive pairs

As expected, the RMS amplitudes of the pulse-echo signal suggests that PZT ceramic elements bonded with marine epoxy produces the strongest source signal. Following this set is the PZT ceramic element bonded with silver conductive epoxy, and with the lithium niobate single-crystal producing the weakest signal. Normalizing these values by the max RMS amplitude (Figure 4.3b) shows that the lithium niobate single-crystal shows the least amount of variation with temperature, but it cannot produce signals with the same strength as the PZT. However, due to the highly attenuative nature of bitumen and bitumen-saturated rocks, the optimal solution would be to choose a piezoelectric material and adhesive that maximizes the absolute energy of the transmitting ultrasonic wave. Thus, for our transducer material, we will use the PZT ceramic material with a marine weld epoxy.

4.1.2 Ultrasonic Transducer Assembly

To accommodate the 3.81 cm (1.5 inch) diameter cylindrical rock cores, specialized high-temperature ultrasonic transducers were made (Figure 4.4). As mentioned in the previous section, the piezoelectric element material used for this transducer is a PZT ceramic with a

resonant frequency of 1 MHz, manufactured by APC International, Ltd (Figure 4.5). Using a J-B Weld Marine Epoxy, the element is bonded directly onto the aluminum endcap, which acts as a buffer between the piezoelectric element and the rock specimen. A pore inlet is first machined through the endcap and then fitted with a stainless-steel tube, sealed to the endcap using high-pressure grade cone sealing couplings. During the experiment, this tube is fed through the pressure vessel to a HIP 37-6-30 high pressure generator with a max pressure rating of 207 MPa (30,000 psi). Wires are attached using solder to the positive and negative electrodes of the piezoelectric element. To protect the electrical components from the high pressure and temperature environment, the entire top of the endcap is then encased in Flexane™, a non-conductive polyurethane-based compound. The Flexane™ coating also acts as a damping material for the piezoelectric element, reducing the ringing in transmitted and reflected signals. In typical transducer designs for NDT (non-destructive testing) and medical imaging applications where damping / backing material is used, there is a greater importance placed in maximizing imaging resolution. The role of the damping material is to reduce the ringing of the piezoelectric element, which produces a shorter transmitted signal. The damping material also has the effect of broadening the bandwidth in order to capture more of the higher and lower frequencies at the expense of the overall energy of the transmitted ultrasonic wave. However, in our experiment, there is a greater importance placed on getting the ultrasonic waves through the highly attenuative bitumen-saturated rock, therefore we have excluded the use of damping material in order to maximize the amount of energy transmitted into the rock samples.

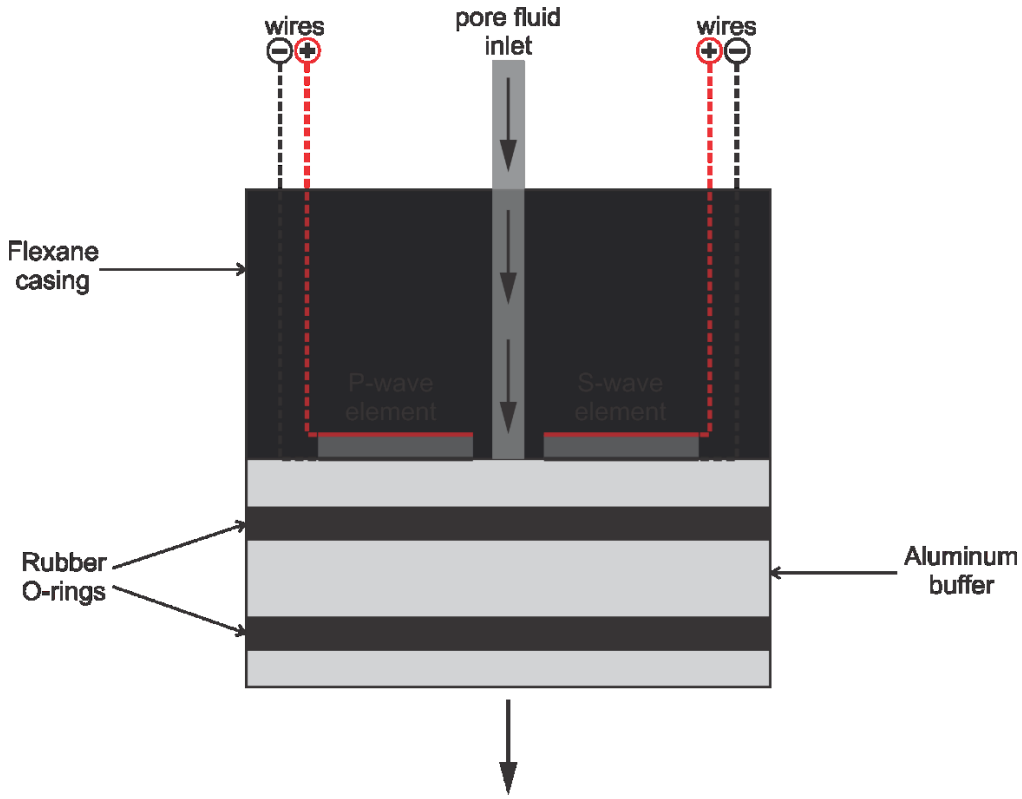

Figure 4.4: Schematic of the high temperature ultrasonic source / receiver transducer

Grooves are then carefully machined into the endcap and then fitted with high-temperature resistant rubber O-rings (Buna-nitrile 70A). During the experiment, the cylindrical sample is placed into a jacket with source and receiver transducers coupled to both faces. Hose clamps are then used to seal the jacket against these rubber O-rings. Further details of this procedure are provided in Section 4.2.

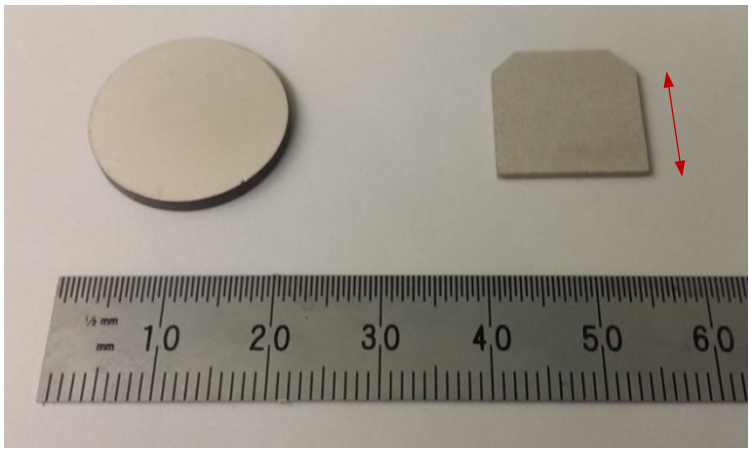

Figure 4.5: PZT Piezoelectric ceramic elements, manufactured by APC International, Ltd. P-wave axially polarized element (left) APC Material 842, and S-wave transversely polarized element (right) APC Material 850. For the S-wave element, polarization direction is in / out of the page while the red arrow shows displacement direction

4.1.3 Experimental setup / instrumentation

The instrumentation for the ultrasonic velocity measurements consists of a pulse / receiver (Olympus Panametrics-NDT 5800PR), digital oscilloscope (NI USB-5133) with a 100 MS/s sampling rate, and a custom-made LabView® program used to display and record the ultrasonic waveforms. The pulser / receiver applies a continuously pulsing 200 V square wave to excite the source transducer. The generated mechanical vibration travels through the sample as an ultrasonic wave and gets converted back to an electrical signal by the receiver transducer. This electrical signal then gets digitized by the oscilloscope and displayed within the LabView® program. Ultrasonic waveforms are stacked 300 times to reduce random electrical noise and then saved to disk.

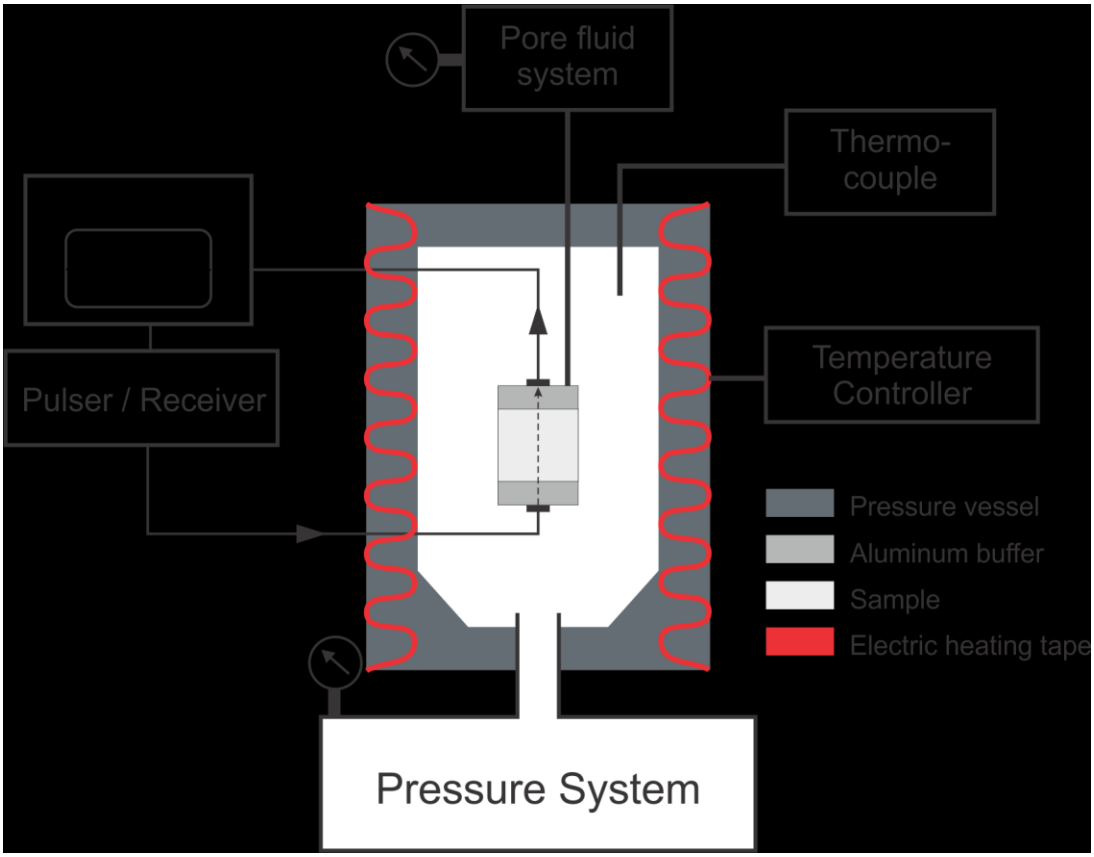

Figure 4.6: Simplified schematic of experimental setup and associated instruments. Figure from Rabbani et al. (2016) *with permission granted from the Society of Exploration Geophysicists through their Fair Use Policy.*

During the experiment, samples are subjected to a wide variety of pressure conditions. In this study, a cylindrical pressure vessel (Figure 4.6) was used to apply hydrostatic confining pressure to the samples. The pressure vessel uses hydraulic oil as its confining fluid and is outfitted with a Quizix Q5000 high pressure syringe pump, capable of producing pressures up to 70 MPa.

To change the temperature of the sample, the confining fluid is either heated or cooled, and the temperature change is allowed to diffuse into the sample over a period of time. To heat the confining fluid, electrical heating tape is wrapped around the cylindrical pressure vessel, along with insulating fabric to prevent loss of heat to the surrounding environment. To

measure the temperature of the hydraulic oil, a K-type thermocouple, manufactured by OMEGA Engineering, Inc., is fed into the pressure vessel. The thermocouple, along with the electrical heating tape, is wired directly into a custom-built temperature controller. For the cooling process, cold water is circulated around the pressure vessel using copper tubing and a NESLAB Endocal RTE-8DD Refrigerated Bath / Circulator. The temperature of the water bath circulator is manually controlled and generally set below the desired temperature to account for heat loss to the environment.

The pore fluid tube is fed through the pressure vessel to a HIP 37-6-30 high pressure generator using a series of stainless-steel tubing with cone sealing couplings. The hand pump works independently of the confining pressure system and deliver pore pressures up to 207 MPa (30,000 psi).

4.2 Sample Preparation

The bitumen-bearing samples are preserved in deep refrigeration prior to the measurement procedure to prevent the bitumen and other pore fluids from leaking out at room temperatures. The sample is cored to a diameter of 38 mm (1.5 inches) and faces ground parallel within a tolerance of 0.1 mm. Source and receiver transducers are then placed at both ends of the sample and the entire assemble is placed into a Kuri-Tec Klearon 73 PVC tubing. Steel hose clamps are placed and tightened around the PVC tubing, aligned with the rubber o-rings on the transducers to seal them. This step prevents contamination of the rock sample from the hydraulic confining fluid. The pore fluid tube is then connected, and the entire assembly is placed inside the pressure vessel.

4.3 Experimental workflow

In this study, samples are measured under a variety of temperature, pressure, and saturation conditions. Before going into further details on these conditions, it may be important to define the different types of pressures that may be applied to a given rock material.

As previously mentioned, the experimental apparatus is capable of providing two types of pressure: confining pressure, and pore pressure. Confining pressure is the external pressure acting on the surface of the sample while pore pressure is the pressure due to fluids contained within the pore space. The confining pressure, more commonly known as the overburden or lithostatic pressure, is the pressure imposed on a rock by the weight of the overlying material. In this real world this would be complicated in that there rarely would be a uniform pressure applied to the sample as an anisotropic state of stress is more likely to exist. Given that we do not know these stresses, we take the overburden pressure to adequately replace the three in situ stresses. At a given depth z, the overburden or confining pressure P_c can be calculated by

$$P_c = \rho g z \,, \tag{4.2}$$

where ρ is the density of the overlying rock material. On the other hand, pore pressure P_p is often referred to as the reservoir or formation pressure. The effects of these two pressures counteract each other and if the pore pressure is uniform throughout the pore space, we can define what is known as the differential pressure P_e

$$P_e = P_c - nP_p \,, \tag{4.3}$$

where the parameter n is called the effective stress coefficient. The value of this parameter is usually taken to be unity in the absence of any other information about the rock frame. It is also important to define terms: drained and undrained conditions. Drained conditions occur when pore fluid is allowed to freely in and out of the rock material. This condition prevents changes in pore pressure due to applied pressures or other external forces. In a laboratory context, this would mean venting the pore fluid inlet to the atmosphere, allowing pore fluids to freely move in and out of the sample such that the pore pressure can equilibrate. On the

other hand, undrained conditions occur when pore fluid is not allowed to flow in or out of the sample. Such conditions would lead to stress-induced pore pressure changes.

The experimental workflow for each sample consisted of measuring P- and S-wave velocities in 4 distinct sequential runs in which the conditions are varied following the protocol of:

1. Initial measurement of velocities on sample with all preserved pore fluids. In this run, the pore pressure is subjected to atmospheric conditions while the confining pressure is varied up to 40 MPa.
2. Measurement of velocities on sample subjected to a constant differential pressure. Similar to the initial run, the confining pressure is increased up to 40 MPa, however in this run, the pore pressure is controlled to maintain a constant differential pressure of 7 MPa (in-situ pressure at reservoir depths).
3. Before proceeding to the dry frame run, the bitumen and other associated pore fluids are extracted from the sample through a Soxhlet extraction method using toluene as the solvent. Depending on pore and permeability of the rock material, extraction times range from a minimum of 2 weeks up to 4 weeks. Samples were determined to be void of bitumen and other pore fluids when the solvent ceases to change colour.
4. After removal of solvent, velocities were then measured on dry frame of the rock. Pore pressure is subjected to atmospheric conditions (drained conditions) while the confining pressure is varied up to 40 MPa.
5. Samples are then re-saturated with water and measurements of velocities are repeated in the same conditions as run 2 (constant differential pressure of 7 MPa).

4.4 Picking of Transit Times

Transit times are picked from the first positive or negative extremum of the resulting waveform. These transit times are then shifted to the first arrival of the signal through a calibration procedure. In this procedure, the ultrasonic transducers are placed together and

jacketed with no sample in between. The assembly is placed in the pressure vessel and Pulse Transmission waveforms are obtained for the same temperature and pressure conditions experienced by the rock samples. Transit times are picked for these calibration waveforms at the first extremum, which are then subtracted from the transit times picked for the sample measurements. This step effectively accounts for the extra transit time needed for the ultrasonic wave to pass through the aluminum buffer endcaps as well as any system response delay associated with the excitation of the piezoelectric elements. The ultrasonic velocity is then calculated by the simple ratio of the sample length to the calibrated transit time.

4.5 Error Analysis

The main sources of error for velocities obtained through the Pulse Transmission Method are associated with the determination of sample length and transit times. As mentioned in Section 4.2, the parallelism of the sample's end-faces is accurate to 0.1 mm; thus the error in sample length is the sum of that value and the uncertainty in the resolution of the measurement instrument. The total uncertainty in time consists of the measurement error in the oscilloscope (10 ns) in addition to the errors associated with picking transit times are dependent on the quality of the signal. In general, quality of the signal increases with confining pressure as the closure of cracks facilitates the transmission of the ultrasonic wave. Despite this, the quality of the signal can vary widely from sample to sample due to differences in the structure of the rock frame as well as the different bitumen saturation levels.

Other sources of error may be attributed to the changes in sample length due to thermal expansion, as well as the thermal hardening of the aluminum transducer buffers from temperature cycling that potentially could influence the accuracy of the calibration.

4.6 Sample Characterization

Detailed knowledge of the sample material characteristics is crucial in the analysis and interpretation of the laboratory measurements presented in the later chapters. This is especially important for carbonate reservoirs where post-depositional processes have created a wide-range of pore types and sizes in the geologic material. In this chapter, we describe a variety of petrophysical parameters and laboratory methods used to determine said parameters. A summary of the petrophysical properties is presented below in Table 4-2.

Table 4-2. Petrophysical parameters

Sample	Porosity (%)		Grain density (kg/m^3)		Dry bulk density (kg/m^3)		Bitumen saturated bulk density (kg/m^3)
	He Pyc	MIP	He Pyc	MIP	Dim.[1]	MIP	
SA1	10.9	8.7	2830	2781	2492	2540	2588
S3	15.8	17.3	2712	2689	2257	2224	2460
S6	9.0	7.7	2826	2787	2572	2573	2637
S8	10.0	11.4	2798	2816	2541	2495	2563
S15	10.5	12.7	2802	2803	2510	2447	2613
S17		22.9		2767	2106	2132	2305

1. Dry bulk density calculated from mass and dimensions of cleaned cores

All materials characterization techniques are performed on core samples after Soxhlet extraction (i.e., the rock material devoid of pore fluids). Petrophysical analysis of the pore structure was completed using mercury intrusion porosimetry, gas pycnometry, and scanning electron microscopy (SEM). X-ray diffraction (XRD) analysis provided a qualitative assessment of minerals present in the sample material.

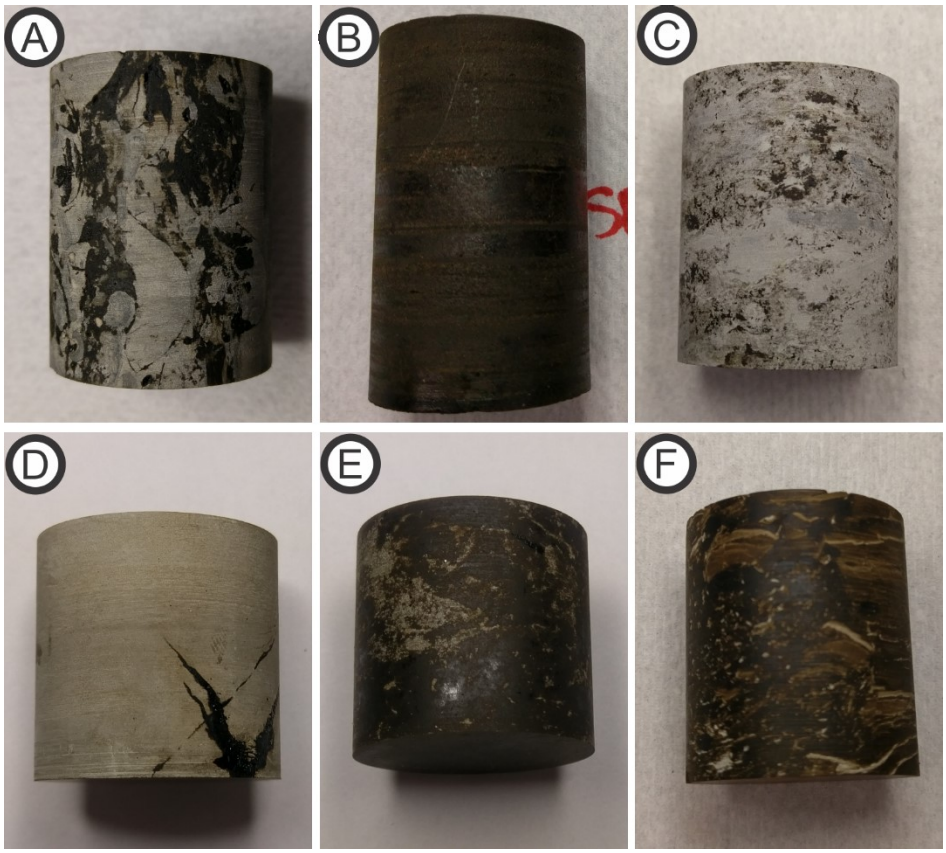

Figure 4.7: Core images of samples used for ultrasonic velocity study; a) Sample A1, b) Sample 3, c) Sample 6, d) Sample 8, e) Sample 15, f) Sample 17

4.6.1 Mercury Intrusion Porosimetry (MIP)

Mercury intrusion porosimetry (MIP) is a technique used to the study the pore structure of materials as well as provide estimates of common petrophysical parameters such as bulk density, grain density, porosity, and permeability. The mercury porosimeter used in this study is a Micromeritics AutoPore IV, which is capable to revolving pores throats with diameters ranging between 0.003 μm and 360 μm (Webb, 2001).

Mercury, which is a non-wetting liquid has the property of not intruding pores without the aid of an external force or pressure. In contrast, water and other wetting liquids will flow into the spaces of porous media at atmospheric pressure through capillary action.

Samples are put into sample holding 'penetrometers', which are then vacuumed to remove fluids from the rock material, and then injected with mercury. At atmospheric pressure, this injected mercury will surround the sample material without invading the pore space. Since the volume of the penetrometer is already known, by measuring the volume of mercury encasing the sample material, the porosimeter can immediately provide an accurate estimate of the bulk or envelope volume. The amount of mercury forced into the pore space of a given material is proportional to the pressure applied. This effect is represented by the Washburn equation

$$D = -\frac{4}{P}\gamma \cos\theta \ , \tag{4.4}$$

where D is the pore diameter, γ is the surface tension of the liquid, θ is the contact angle, and P is the applied pressure (Wardlaw and McKellar, 1981). It is important to note that the Washburn equation inherently makes the assumption that the pores and pore throats in the sample material are cylindrical in geometry, although this is rarely the case in real porous materials and particularly in rock. Furthermore, the diameter calculated from MIP analysis is more representative of the pore entry size as opposed to the size of the pore itself (Giesche, 2006).

Additionally, there are two other important limitations that should be considered for the analysis of MIP data. The first being that the mercury is only capable of intruding into pore space that is connected to the surface of the sample material. The second being that MIP analysis can only measure the properties of a small volume of sample material, which may not be representative of the rock as a whole. The first limitation means that closed, occluded, pore space is not considered in the estimation of porosity of the sample material, which is to say that the connected porosity is measured, and not the total porosity. In the context of most petroleum generation and production, the connected porosity is the more sought-after

parameter as it is only the interconnected pore volume that stores accessible fluids and contributes to fluid flow within a reservoir.

The second limitation is particularly important consideration for this study as the Grosmont formation is an especially inhomogeneous reservoir. In order to have a representative estimate of the reservoir porosity, the volume of rock material needed for measurement would be beyond the capabilities of MIP analysis. In addition, many of the pores, including the vug porosity seen throughout the cores, have dimensions larger than the upper limit of resolution for the porosimeter. Therefore, the pore volume measured only include intercrystalline, interparticular, small fractures, and other micro-scale features.

MIP measurements were performed on all 6 samples with the pore size distribution for each sample given in Figure 4.7. These samples provide a good range of different pore structures.

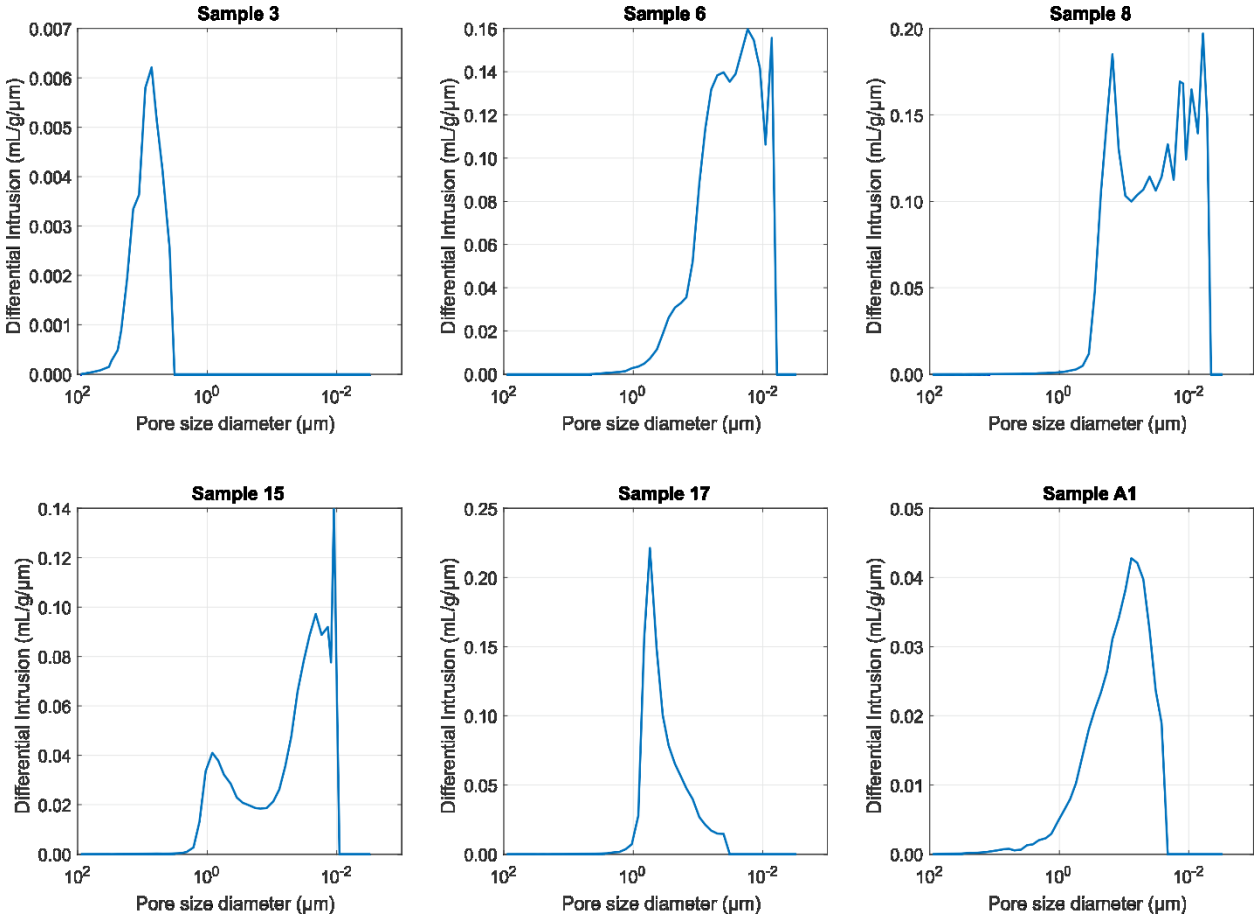

Figure 4.8: Differential mercury intrusion curves as a function of pore size diameter for samples

4.6.2 Helium Pycnometry (He Pyc)

Gas expansion pycnometers are instruments commonly used to measure the volume of solids. In this study, we will be using it to measure the skeletal volume of our rock samples. The skeletal, or grain volume, is the total volume of the rock without consideration of pore space. Gas pycnometry measures the volume based on Boyle's Law, which equates the pressure and volume of a gas under different sets of conditions

$$P_1V_1 = P_2V_2\,, \tag{4.5}$$

where P is the pressure, and V is the volume of the gas. The instrument consists of two separated but connected (by valve) cells of known volume. After loading the sample material into the sample cell, both cells are evacuated prior to filling them with gas. Helium is commonly used as the expanding as the small molecule size allows it to penetrate small pores and crevices (Donato and Lazzara, 2012). The reference cell is first filled with the helium gas where P_1 is known, and V_1 is measured by a pressure transducer. Upon opening the valve, the helium gas flows into the sample cell where equilibrium is established between the two cells. Once P_2 is measured in the sample cell, we can calculate V_2 by Equation 4.5, where the value represents the total volume of the sample and reference cell minus the volume of the sample. We can then calculate the sample volume using

$$V_s = V_c + \frac{V_r}{1 - \frac{P_1}{P_2}}\,, \tag{4.6}$$

where V_s, V_c, and V_r are the volumes of the sample (skeletal / grain volume), empty sample cell, and empty reference cell respectively. The skeletal density ρ_s is then calculated by the following equation

$$\rho_s = \frac{m}{V_s}\,, \tag{4.7}$$

where m is the mass of the sample. From the skeletal density or volume, we can also calculate the porosity if we have the corresponding bulk density or bulk volume.

$$\phi = 1 - \frac{V_s}{V_b} = 1 - \frac{\rho_b}{\rho_s}\,, \tag{4.8}$$

where V_b and ρ_b are the bulk volume and density respectively.

4.6.3 Scanning Electron Microscopy (SEM)

Scanning electron microscopy (SEM) is a common materials characterization technique that produces high-resolution imaging data with relatively little sample preparation. The instrument works on principle of detecting backscattered electrons, secondary electrons, and x-rays that are emitted from the sample that result of excitation from an electron beam. During SEM analysis, a beam of electrons is emitted from an electron gun and focused on a small area of the sample. The emitted electrons collide with the sample material and secondary electrons are ejected. The detection of these electrons, or alternatively, the backscattered emitted electron off the surface of the sample, can be used to form an image.

SEM analysis was completed using a Zeiss EVO LS15 EP-SEM with a LaB6 electron source. The instrument has a resolution of approximately 100 nm and analysis was conducted on dry sample material to characterize the pore structure of the rock material. As high vacuum conditions are required during SEM analysis, rock material containing pore fluids could not be imaged as it would affect the vacuum state and possibly damage the instruments. Sample preparation includes the conductive carbon coating using a Leica EM SCD005 evaporative coater.

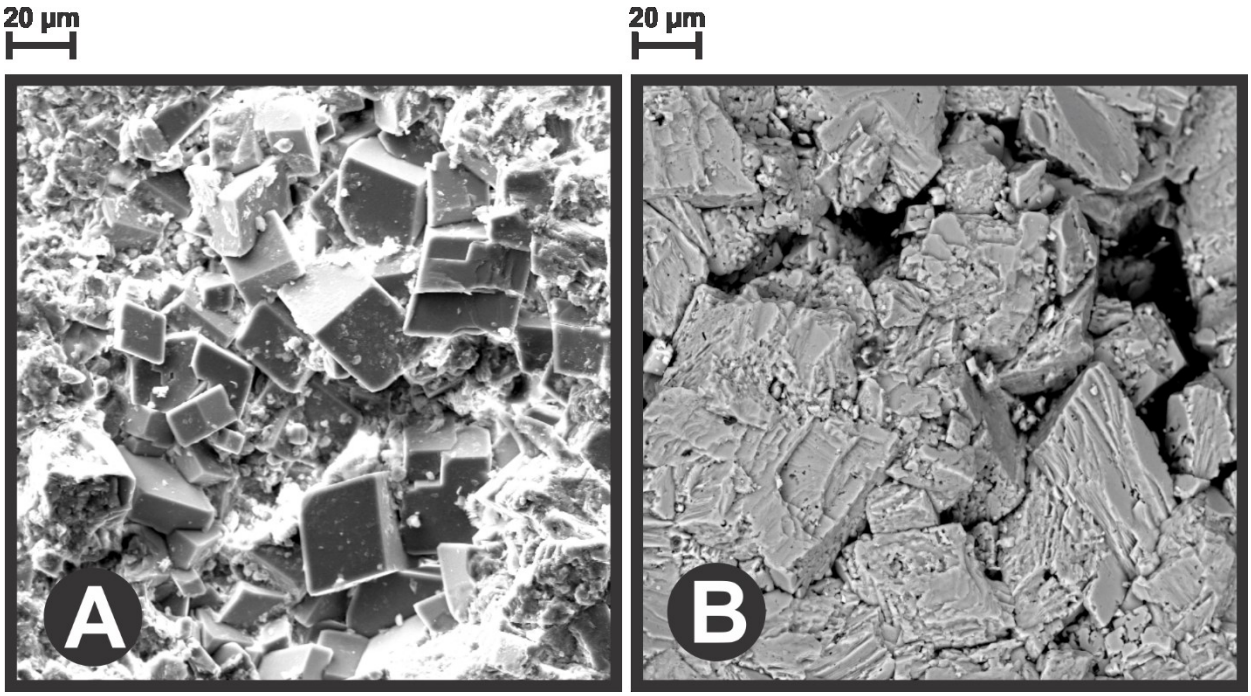

Figure 4.9: Scanning electron microscopy images of porosity found in samples. (a) Sample 3, showing euhedral dolomite crystals and intercrystal porosity. (b) Sample 6, showing intracrystal dissolution porosity in dolomite crystals and intercrystal porosity

Intercrystal porosity is pervasively found within all samples with relatively, evenly distributed pore sizes. Large euhedral dolomite crystals are commonly observed, along with intracrystal dissolution porosity within the crystals themselves. Large and small vugs are can observed by the unaided eye and at low levels of magnification in samples SA1, S6, S8, and S15.

4.6.4 X-Ray Diffraction Analysis (XRD)

X-ray diffraction (XRD) techniques are commonly used in the identification of crystalline material by the principle of Thomson scattering (Lavina et al., 2014). When materials with a crystalline structure are illuminated by x-ray radiation, a distinct diffraction pattern is produced that is characteristic of the structure. As the angle θ of the x-ray source is varied, the intensity of the reflected radiation is recorded by the opposing detector at an angle 2θ from the source path. The relative intensities are plotted against the detector angle 2θ and compared with a catalog of reference diffraction patterns of known crystalline material. The

method allows for the qualitative identification of multiple minerals in a given sample with minimal preparation.

Samples are ground down into a fine powder with an approximate particle size of 10 microns. Data was collected using at Rigaku Ultima IV x-ray diffractometer provided by the Earth and Atmospheric science department at the University of Alberta. The x-ray generator of the machine uses a cobalt block run with a tube voltage and current of 38 kV and 38 mA, respectively. Tests were run with a continuous scan of 2.0°/min with a sampling width of 0.02°. The scan ran with a detector angle 2θ between 5° and 90°. The results of the XRD analysis is presented below in Table 4-3. XRD analysis showed that all samples were composed predominately of dolomite and quartz with trace amounts of the other minerals. Future work should include more quantitative assessment of the mineral modes.

Table 4-3. Sample information and composition

			X-ray Diffraction Analysis					
Sample	**Well**	**Depth (m)**	Dolomite	Quartz	Kaolinite	Illite	Pyrite	Sanidine
SA1	101/10-26-85-19W4	360.79	■	■	■		■	
S3	100/01-27-85-19W4	384.46	■	■				
S6		374.66	■	■	■	■		
S8		371.09	■	■		■	■	■
S15		349.97	■	■				
S17		347.27	■	■	■		■	■

4.7 Summary

This chapter provided details on the methodology behind the ultrasonic velocity study and characterization of samples. Details are provided for the Pulse Transmission Method, which is used to obtain waveforms used for the determination of P- and S-wave velocities. This chapter provided extensive details on the choice of piezoelectric elements, assembly of the ultrasonic transducers, and description of the experimental / instrumentation setup. The procedure for sample preparations and experimental workflow are also provided, outlining exact pressure, temperature, saturation conditions for each sample. P- and S-wave velocities are estimated using the measured sample length and transit time of the ultrasonic pulse, picked from first extremum (after calibration step).

Sample characterization was also completed on 6 carbonate samples taken from two wells within the Grosmont Formation. Characterization techniques were performed on clean samples, devoid of pore fluids (dry state). Mercury intrusion porosimetry (MIP) and helium pycnometry were used to determine the porosity, bulk density, and grain density for all samples and are summarized in Table 4-2. MIP was used to provide details of the pore size distribution with scanning electron microscopy (SEM) revealing intercrystal porosity found pervasively within all samples. X-ray diffraction analysis (XRD) showed that all samples were composed predominately of dolomite and quartz with trace amounts of kaolinite, illite, pyrite, and sanidine.

5 Ultrasonic velocities – Results and Discussion

The P- and S-wave ultrasonic velocities for the entire set of Grosmont formation carbonate samples were measured under varying temperature, pressure, and saturation conditions. The complete details on these conditions are found in Section 4.3. Velocities were estimated using Equation 4.1 where the transit times were picked from the recorded waveforms, an example of which is illustrated in Figure 6.6.

For visual clarity of the velocity results, only the measurements for the increasing pressurization cycle are plotted in this section. For the complete set of measurements, which include the waveforms and picked transit times associated with the depressurization cycle, please refer to the corresponding PANGEA archive.

5.1 Temperature and Pressure Dependence

The ultrasonic velocities for each sample are plotted as a function of confining pressure and temperature (Figures 5.1 – 5.6). P- and S-wave velocities are observed to drop significantly with increasing temperature for the naturally-preserved sample runs (Figures 5.1(a-b) – 5.6(a-b)) which is most likely attributed to the change in the physical properties of the saturating bitumen. These fluid effects are thought to be a result of decreasing fluid bulk and shear moduli with temperature. It is important to note that the decrease in temperature is relatively small in comparison for the dry and water-saturated states of each sample (Figures 5.1(c-d) – 5.6(c-d)).

Pressure-dependent effects are also seen in these samples with preliminary observations including the increase in P- and S-wave velocities with confining pressure as well as pore pressure. One notable exception for this trend is the dry run measurements for Sample 6 in which P-wave velocity is observed to decrease with increasing confining pressure while S-wave velocity increases. Additional details and a discussion of these pressure and temperature associated effects are provided in Section 6.5.

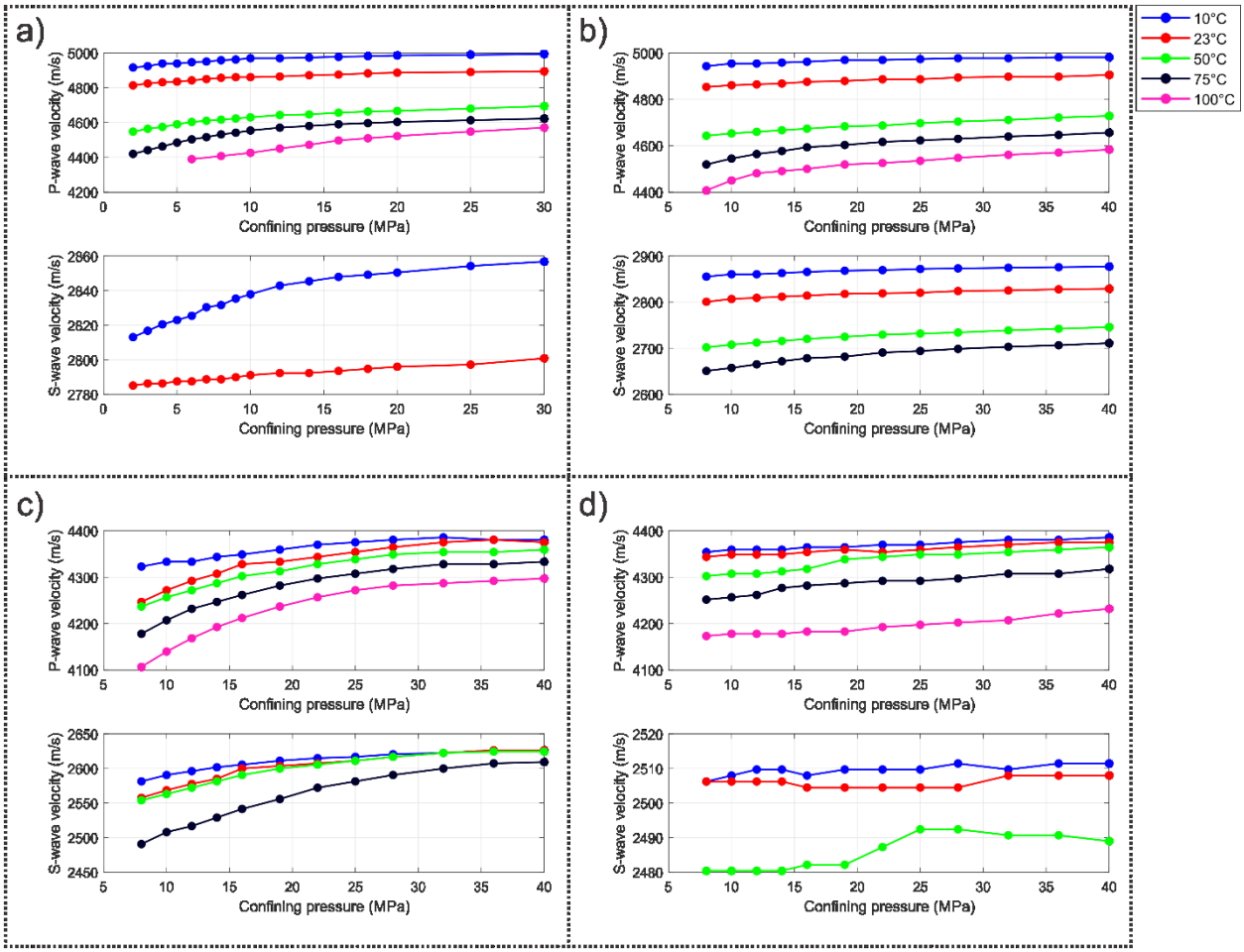

Figure 5.1: Plots for P- and S-wave velocities for Sample 3 as a function of confining pressure under conditions of a) naturally-preserved state with P_p = 0 MPa, b) naturally-preserved state with P_e = 7 MPa, c) dry state with P_p = 0 MPa, and d) water-saturated state with P_e = 7 MPa

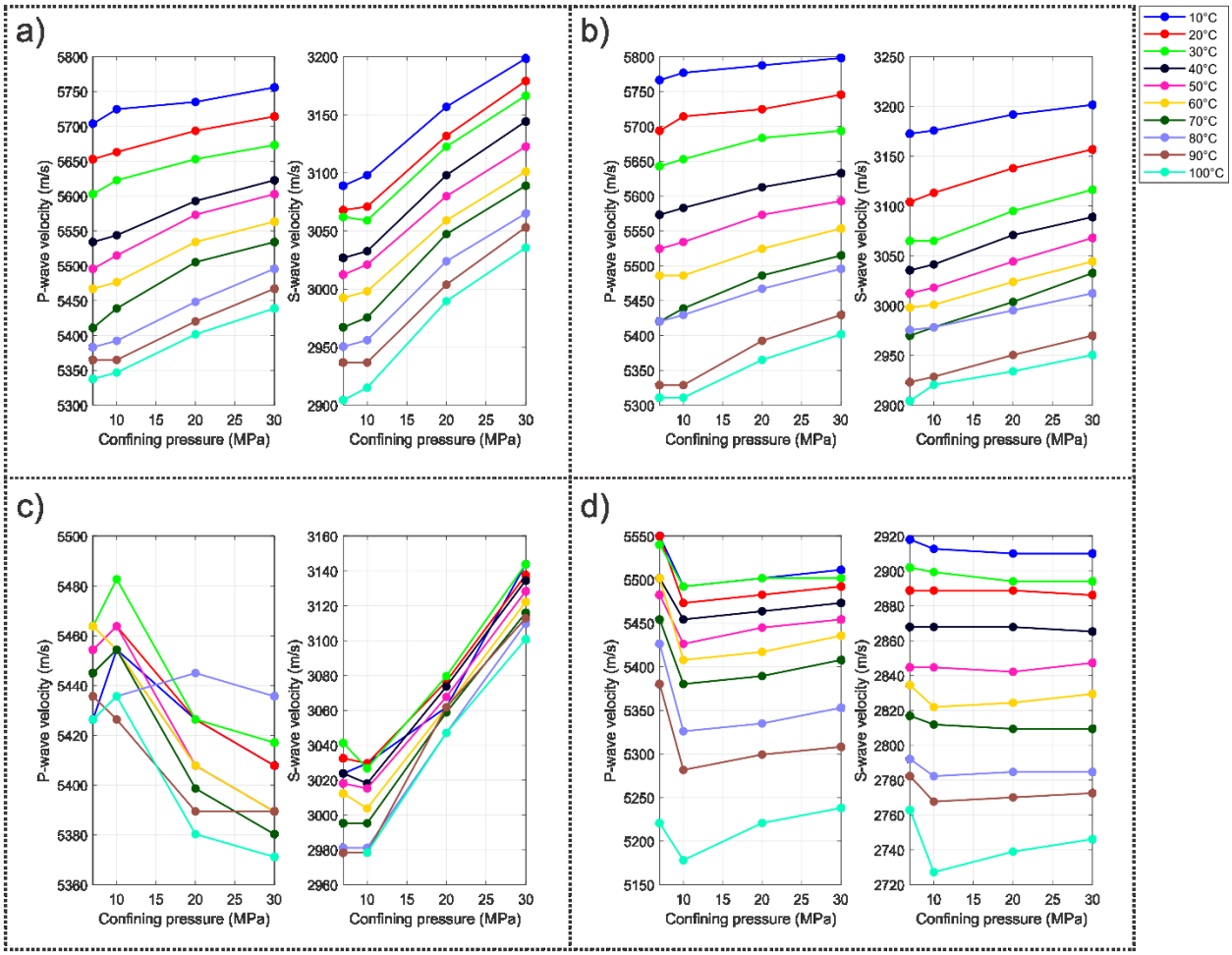

Figure 5.2: Plots for P- and S-wave velocities for Sample 6 as a function of confining pressure under conditions of a) naturally-preserved state with P_p = 0 MPa, b) naturally-preserved state with P_e = 7 MPa, c) dry state with P_p = 0 MPa, and d) water-saturated state with P_e = 7 MPa

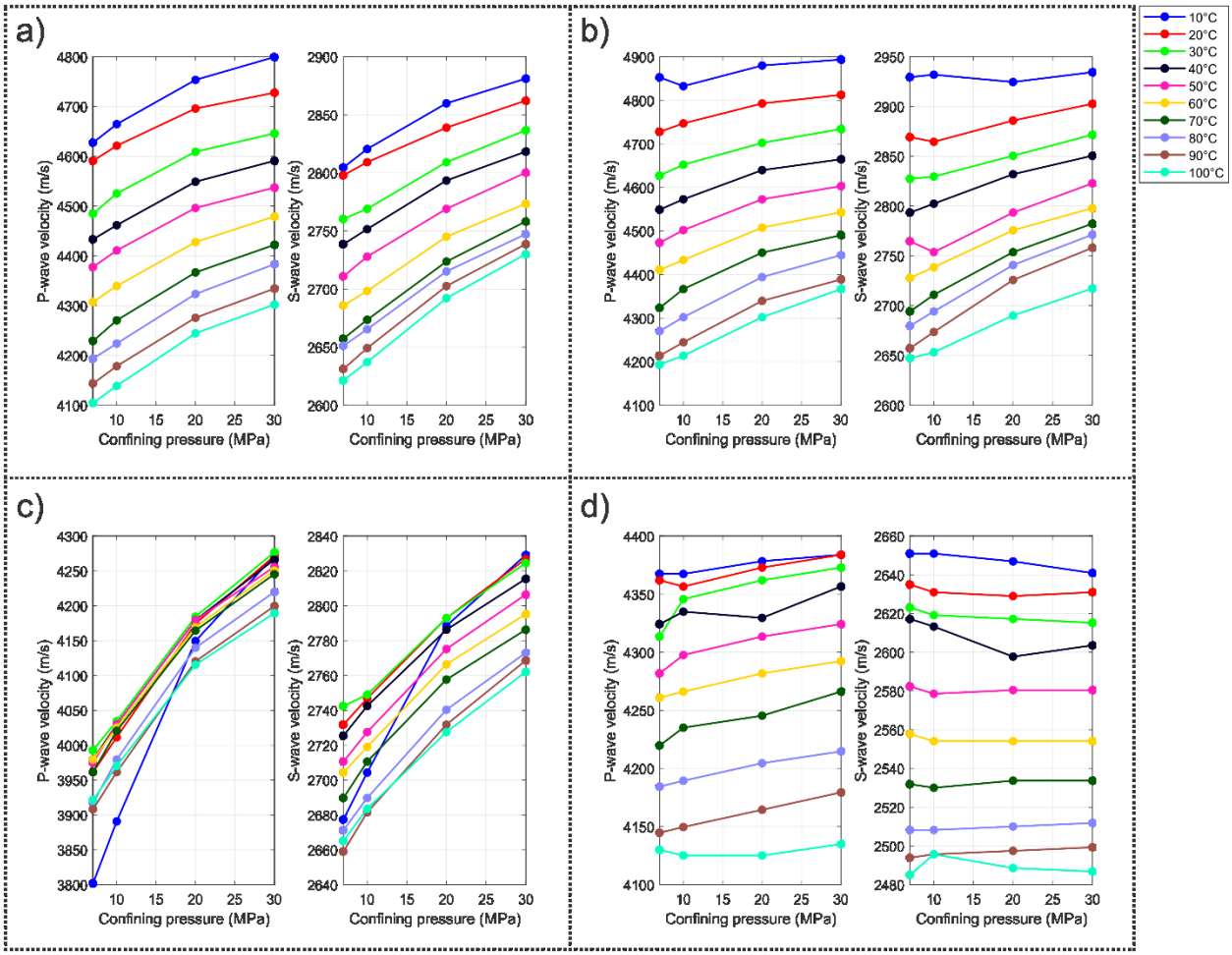

Figure 5.3: Plots for P- and S-wave velocities for Sample 8 as a function of confining pressure under conditions of a) naturally-preserved state with P_p = 0 MPa, b) naturally-preserved state with P_e = 7 MPa, c) dry state with P_p = 0 MPa, and d) water-saturated state with P_e = 7 MPa

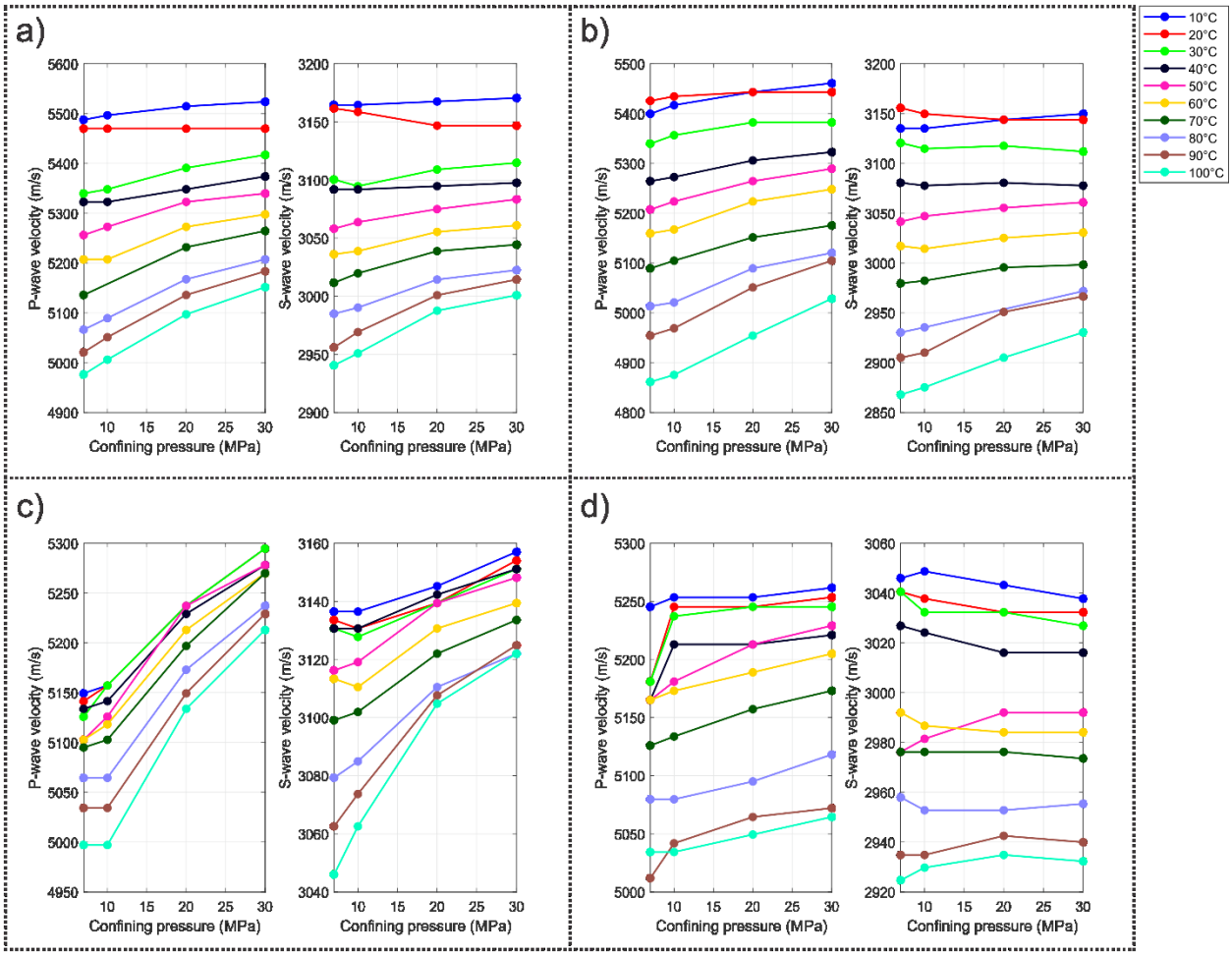

Figure 5.4: Plots for P- and S-wave velocities for Sample 15 as a function of confining pressure under conditions of a) naturally-preserved state with P_p = 0 MPa, b) naturally-preserved state with P_e = 7 MPa, c) dry state with P_p = 0 MPa, and d) water-saturated state with P_e = 7 MPa

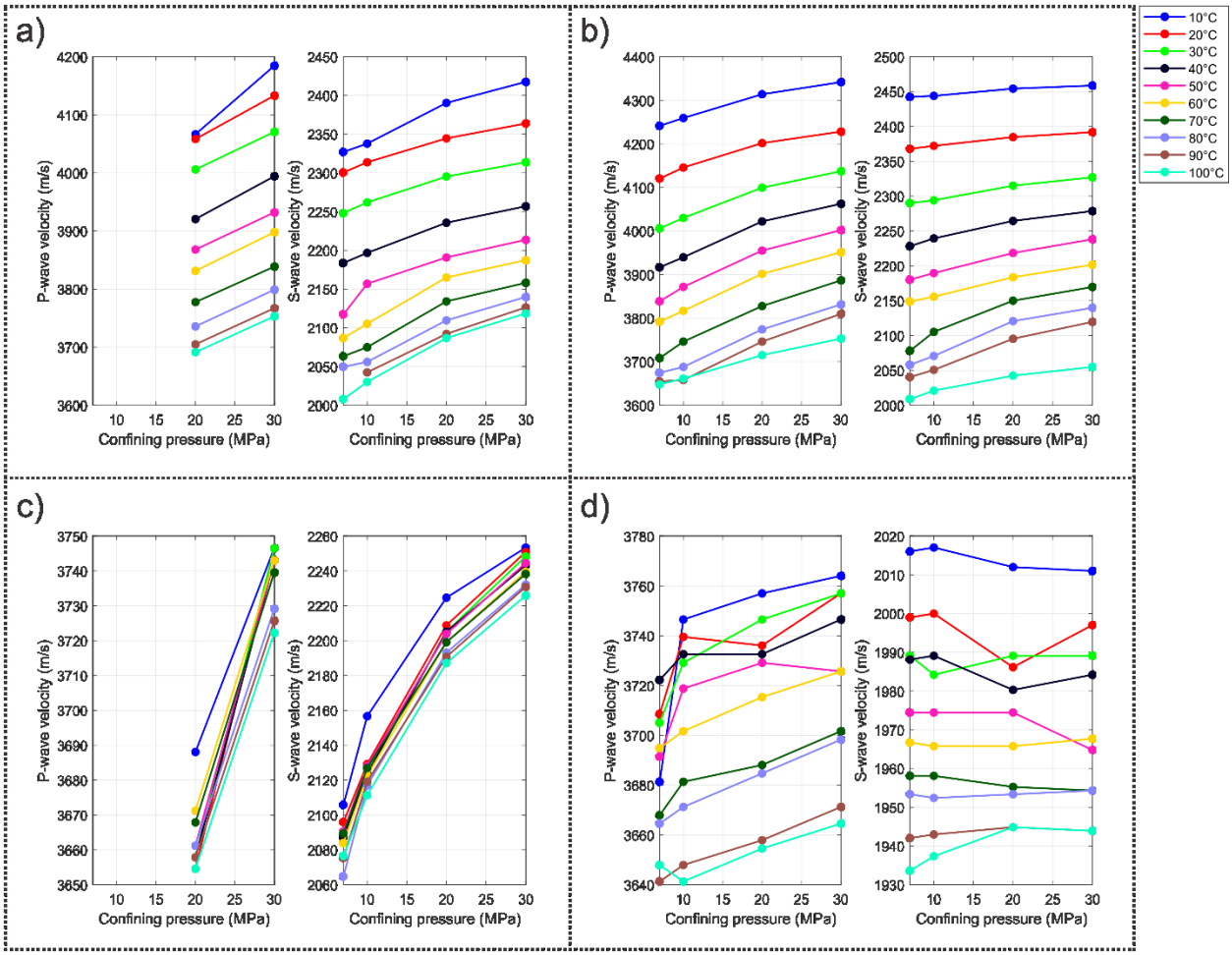

Figure 5.5: Plots for P- and S-wave velocities for Sample 17 as a function of confining pressure under conditions of a) naturally-preserved state with P_p = 0 MPa, b) naturally-preserved state with P_e = 7 MPa, c) dry state with P_p = 0 MPa, and d) water-saturated state with P_e = 7 MPa

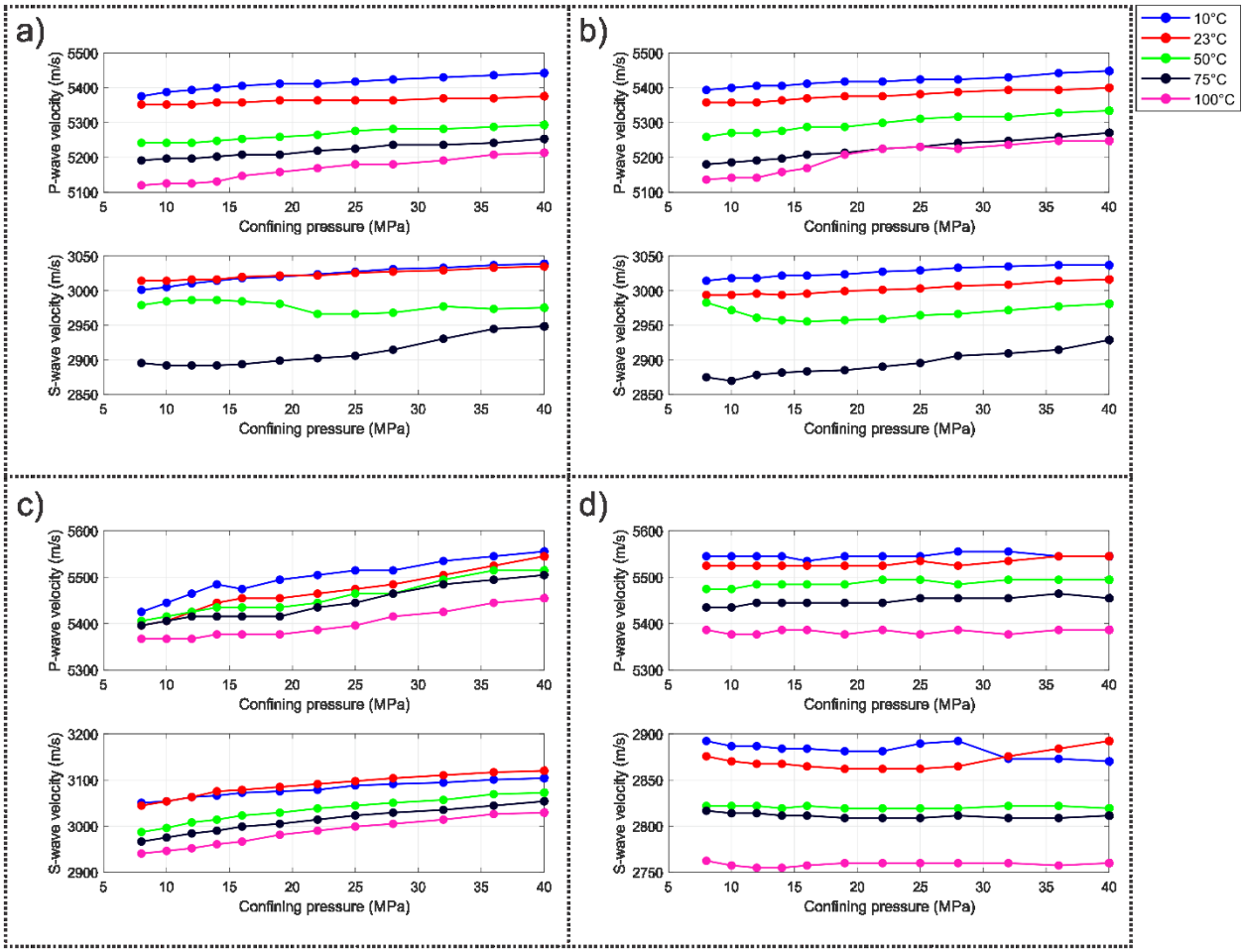

Figure 5.6: Plots for P- and S-wave velocities for Sample A1 as a function of confining pressure under conditions of a) naturally-preserved state with P_p = 0 MPa, b) naturally-preserved state with P_e = 7 MPa, c) dry state with P_p = 0 MPa, and d) water-saturated state with P_e = 7 MPa

5.2 Effects of saturation conditions

The common trend for the majority of samples show the decrease of P- and S-wave velocities with removal of the saturating bitumen, with the exception of Sample A1, which shows the inverse effect. Upon saturation of the dry frame with water, for all samples, P-wave velocity increases while S-wave velocity decreases. These observations are consistent with trends anticipated with the well-known Gassmann relations (Equations 3.40 - 3.41) as the bulk modulus (and consequently, P-wave velocity) for water saturated samples are expected to be higher than for the dry frame. Similarly, since it is assumed that water cannot sustain shear forces, the saturated shear modulus is expected to be equal to the dry shear modulus. However, since the overall bulk density of the sample has increased with saturation, the S-wave velocity decreases according to Equation 3.2. In addition, velocity variations with increasing confining pressure for the water-saturated samples are minimal due to the rock frame presumably not changing when held at constant differential pressure.

The applications of fluid substitution techniques, including, but not limited to the formulations for Gassmann, Biot, Ciz and Shapiro (2007), and Saxena and Mavko (2014) are of great importance in the context of time-lapse seismic methods, although Rabbani et al. (2015) could not reconcile his observed wave speeds with these theoretical models. These models are used to explore how the overall mechanical response of heavy oil saturated rocks is influenced by the properties of its solid and fluid constituents as well as small scale heterogeneity. However, due to the scope of this thesis, these topics will be explored in future contributions.

5.3 Summary

P- and S-wave velocities were measured for 6 Grosmont formation carbonate samples in a variety of pressure, temperature, and saturation conditions. Wave speeds were observed to decrease dramatically with increasing temperature for naturally-saturated samples. The large

decrease in P- and S-wave velocities is likely attributed to the changes in physical properties of the saturating fluid. Pressure-dependent effects are also observed within the dataset showing an increase in velocity with confining pressure. Saturation effects are only briefly discussed in this chapter and will be explored in future contributions.

6 Empirical relations and multi-variate analysis of wave speed measurements

6.1 Introduction

The bitumen reserves of Canada play a significant role in meeting the global demand for energy, which is expected to be in demand for the foreseeable future (ExxonMobil, 2016). The bulk of these reserves are contained within the three major producing oil sands deposits in the Athabasca, Cold Lake, and Peace River areas of northern Alberta (Nasr and Ayodele, 2005; Shin and Polikar, 2005). However, a substantial portion of Canada's remaining reserves lies within the largely untouched carbonate reservoir of the Grosmont Formation (Ardakani et al., 2014). The formation is estimated to hold more than 64.5 billion m^3 (406 billion bbl) of bitumen in place (Burrowes et al., 2010), however, due to the complexity of the reservoir and the need for in-situ recovery, this resource has been left unexploited aside from several small test pilots (McDougall et al., 2008; Yang et al., 2014; Yuan et al., 2010).

As with the immediately overlying Athabasca oil sands, the viscous heavy oil that is hosted within the Grosmont Formation is characterized by a low API gravities (5 – 9°) and proves difficult to recover by conventional methods (Zhao and Machel, 2012). Thermal processes such as cyclic steam stimulation (CSS) and steam-assisted gravity drainage (SAGD) are often employed to reduce the viscosity of the reservoir fluid to the point where in-situ production is possible (Jiang et al., 2010; Mohebati et al., 2014; Rabbani and Schmitt, 2018). Along with the elevated temperature of the reservoir fluid, these techniques can also cause variations in pore pressure, effective stress, and fluid saturation conditions within the reservoir (Bianco et al., 2008). These variations induce a change in seismic response and can be monitored using time-lapse methods (Kato et al., 2008; Schmitt, 1999; Zhang et al., 2007), however, the proper interpretation of the observed data requires knowledge of how thermal enhanced recovery processes influence the physical properties of the reservoir rocks.

In early studies of clastic rocks saturated with heavy oil, laboratory measurements of compressional and shear velocities were shown to significantly decrease with increasing temperature (Nur et al., 1984; Wang and Nur, 1988) and the authors suggested the application of seismic methods to map out the fluid effects within heated reservoirs. Subsequent work by Batzle and Wang (1992) and Wang et al. (1990) came to similar conclusions through the study of rocks saturated with oils of varying densities. Eastwood (1993) studied the dependence of ultrasonic velocity on temperature and found the results to be consistent with theoretical model predictions. Both theoretical and experimental results showed a decrease of compressional velocity with increasing temperature attributed by the change in fluid bulk modulus. Further studies into the properties of the heavy oil itself include the works of Wang and Nur (1990), Daridon et al.(1998), Batzle et al. (2006), Han et al. (2008), and Rabbani et al. (2015), which confirmed the temperature dependence of the fluid. The studies also postulated that at sufficiently low temperatures, the heavy oil acts as a solid with a non-negligible shear modulus (Rabbani and Schmitt, 2018).

In more recent developments, the temperature dependence of heavy oil unconsolidated sands have been reconfirmed in the laboratory measurements of Martinez et al. (2012) and Yuan and Han (2013). In addition to the experimental work, there have been efforts to model the changes in acoustic response of heavy oil bearing rocks in order to further the understanding of time-lapse seismic data (Guo and Han, 2016; Gurevich et al., 2008; Makarynska et al., 2010; Wang et al., 2015; Yuan et al., 2016).

Despite the substantial amount of work completed on oil sands, studies on heavy oil hosted carbonates are still relatively sparse. Rabbani et al. (2017) studied the ultrasonic velocity and attenuation of a bitumen-saturated carbonates from the Grosmont formation under various pressure, saturation, and temperature conditions. The study showed a decrease in P- and S-wave velocities of 12% and 9% respectively, over a temperature range of 10°C – 102°C. In a similar study, Yuan et al. (2017) compared the velocity and attenuation trends of bitumen

saturated sands and carbonates in conditions analogous to a heated reservoir. P- and S-wave velocities were observed to decrease under 10% over a temperature range of 10°C – 120°C for the bitumen-saturated carbonate. Comparatively, over the same temperature range, the bitumen-saturated sand showed a decrease in velocities of 33%.

In this contribution, we build on the initial work of Johnston (2010), Yuan et al. (2018, 2017b) and Rabbani et al. (2017) to further focus on the physical properties of bitumen-saturated carbonates taken from the Grosmont Formation. We describe an extensive series of ultrasonic velocity measurements made on naturally-saturated candidate Grosmont Formation samples subject to ranges of temperature, pore and confining pressures, and saturations analogous to a heavy oil reservoir that is subjected thermal enhanced recovery processes. We organize this paper into sections that briefly review the regional geology, characterize the samples, describe the experimental configuration, and finally the presentation and discussion of the results. In order to maintain clarity, this contribution will emphasize development of a template for P- and S-wave behavior of the bitumen-saturated Grosmont carbonates. The template is developed on the basis of a principal component analysis of the major factors controlling the wave speeds.

6.2 Geologic framework

The primary focus of this contribution is the temperature and pressure dependence of the physical properties of bitumen-hosted carbonate rocks, and as such, we only briefly review the geology of the Grosmont Formation. A more comprehensive review of the regional geology can be found in the discussions of Buschkuehle et al. (2007), Machel et al. (2012), Ardakani et al. (2014) among others.

The Upper Devonian Grosmont Formation is a bitumen-bearing carbonate complex that spans approximately 150 km in width, and 600 km in length across central and north-east Alberta.

The Grosmont Formation consists of limestone and dolomite of different degrees of dolomitization, interbedded with basin-filling shales and marls (Buschkuehle et al., 2007). In its western section, the formation is overlain by the Devonian Upper Ireton and Nisku formations. To the east, however, it subcrops beneath much younger Cretaceous siliclastics deposits progressively thinning out to and eventually disappearing to the northeast. This subcrop surface was a highly eroded karst environment prior to deposition of the overlying McMurray Formation in the Lower Cretaceous.

The Grosmont Formation itself is commonly subdivided into four informal carbonate units, which are called in ascending order (from oldest to youngest) as A, B, C, and D (Machel et al., 2012). Hereafter, we will refer to each unit of the Grosmont formation respectively as GMA, GMB, GMC, and GMD. Conveniently, each carbonate unit is separated by regionally extensive shales and marls, which are easily distinguishable in geophysical logs and are known as the "Grosmont shale breaks" (Ardakani et al., 2014; Jones et al., 2003). Due to the high degree of dolomitization, GMC and GMD exhibit the greatest reservoir potential with high porosity (a combination of matrix porosity and karstification) and bitumen saturation (Hoffmann and Strausz, 1986). Regionally, the degree of karstification is greatest near the sub-Cretaceous unconformity in the North-eastern limit (Luo and Machel, 1995).

The rock samples used in this study were taken from cores obtained from the Saleski Pilot, described by Edmunds et al. (2009), Mohebati et al. (2014), Russel-Houston and Gray (2014), and Yang et al. (2014). Figure 6.1 highlights the main reservoir units of the Grosmont formation along with the overlying Ireton formation on the representative well log. Interpretation of the logs were based mainly on the gamma ray spikes associated with the marl layers separating each unit. Five of the six samples tested in this study were retrieved from this well and are marked on the figure at their corresponding depths. The 6th sample was taken from the well 101/10-26-85-19W4 at a depth of 360.79 m within unit C. All samples were taken from within GMC, GMD, and the marl layer separating the two units.

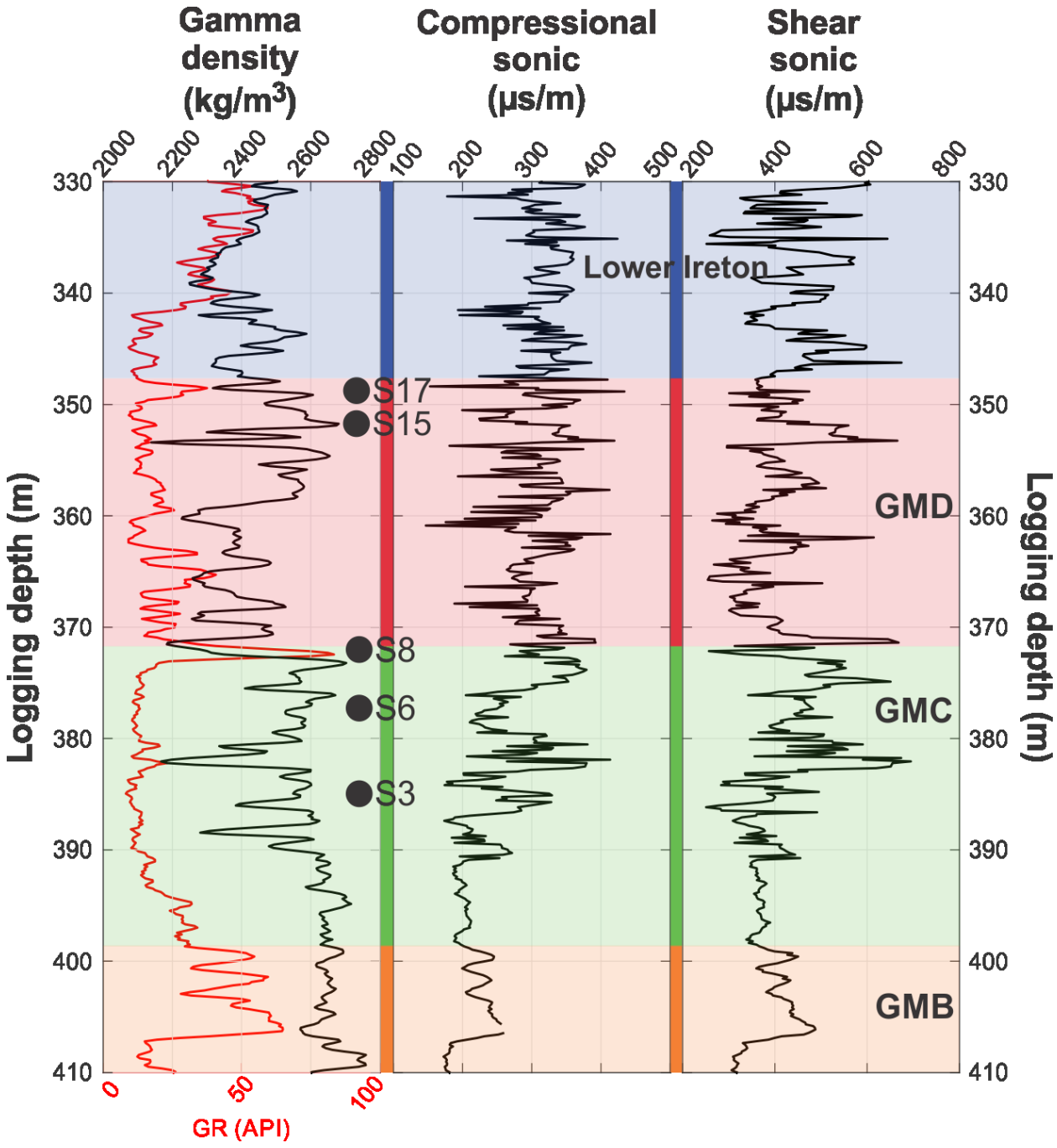

Figure 6.1: Gamma-ray, density, and sonic (monopole compressional and shear) well logs of well 100/01-27-85-19W4 highlighting the tops of major subdivisions of the Grosmont formation along with overlaying strata. Each unit is separated by marl layers often referred to as "shale breaks". Samples used in ultrasonic testing are showed at corresponding depths.

6.3 Sample Characterization

In total, 6 representative samples were collected and prepared for ultrasonic testing. These ultrasonic measurements were first carried out on the naturally-saturated samples taken from frozen core material as provided by our industry partner (Figure 6.2). During the sample selection process, careful consideration was taken to find samples which were both representative of the formation unit and had a high chance of success during ultrasonic testing. However, due to the heterogeneity and heavily karsted nature of the formation, this proved more difficult than expected. Many of the cores taken from the main exploration well exhibit large vugs or are poorly consolidated, consisting of dolomite powder and / or breccia clasts supported by bitumen. Such samples, descriptively referred to as 'Grosmont fudge', are highly attenuative and would not be ideal for ultrasonic testing. In addition, many of the bitumen supported rocks would likely fall apart when subjected to the high temperature conditions during testing or if the pore fluids are removed in subsequent parts of the study. As such, the bias of the sampling possible for testing need to be considered by workers hoping to employ these results.

An extensive suite of ultrasonic measurements was carried out on each of these naturally-saturated samples first. Once this was completed, the hydrocarbons within the pore spaces were removed using a Soxhlet extraction process allowing for petrophysical analysis on the dry frames of the rock. Analysis techniques used in the study include mercury intrusion porosimetry (MIP), helium pycnometry, scanning electron microscopy (SEM), and x-ray diffractometry (XRD). Further series of ultrasonic measurements under the same set of conditions were then made on the dry and then water saturated samples. Presentation of these results are delayed to later contributions in order to focus on development of the bitumen saturated template here, however.

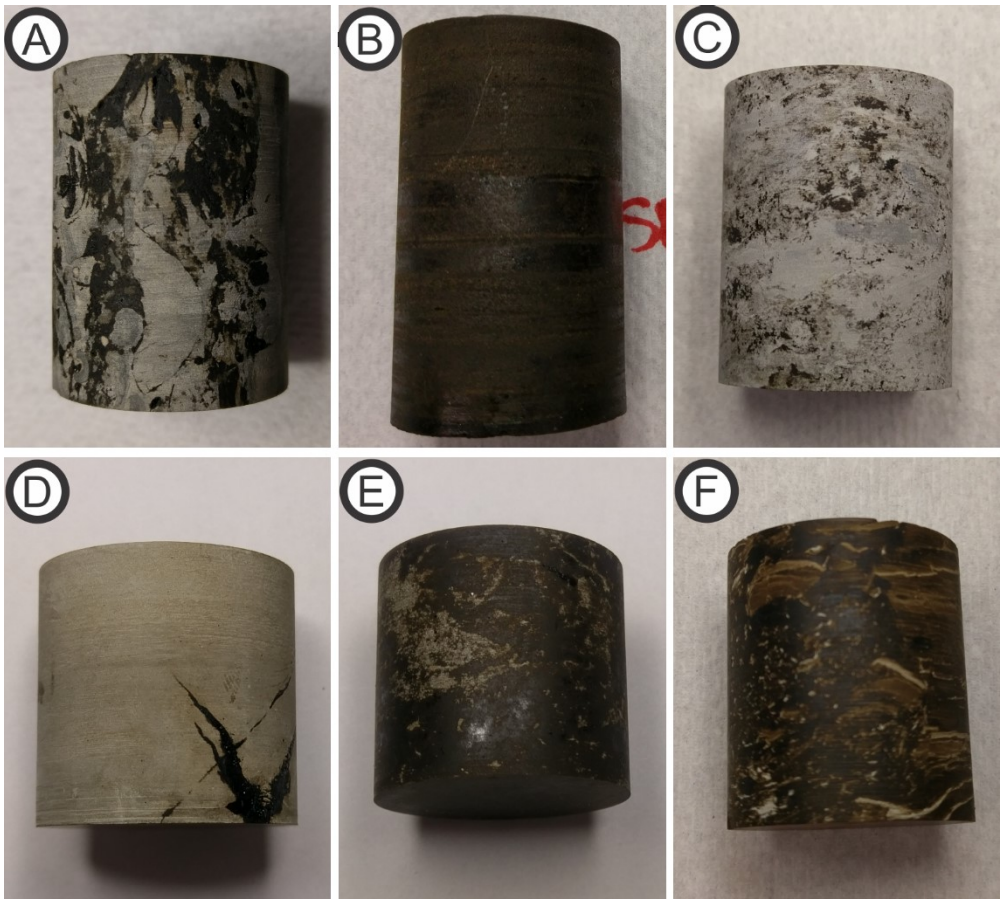

Figure 6.2: Core images of samples used for ultrasonic velocity study; a) Sample A1, b) Sample 3, c) Sample 6, d) Sample 8, e) Sample 15, f) Sample 17

Table 6-1. Petrophysical properties

Sample	Porosity (%)		Grain density (kg/m^3)		Dry bulk density (kg/m^3)		Bitumen saturated bulk density (kg/m^3)
	He Pyc	MIP	He Pyc	MIP	Dim.[1]	MIP	
SA1	10.9	8.7	2830	2781	2492	2540	2588
S3	15.8	17.3	2712	2689	2257	2224	2460
S6	9.0	7.7	2826	2787	2572	2573	2637
S8	10.0	11.4	2798	2816	2541	2495	2563
S15	10.5	12.7	2802	2803	2510	2447	2613
S17		22.9		2767	2106	2132	2305

1. Dry bulk density calculated from mass and dimensions of cleaned cores

Table 6-2. Sample information and composition

			X-ray Diffraction Analysis					
Sample	**Well**	**Depth (m)**	Dolomite	Quartz	Kaolinite	Illite	Pyrite	Sanidine
SA1	101/10-26-85-19W4	360.79	■	■	■		■	
S3	100/01-27-85-19W4	384.46	■	■				
S6		374.66	■	■	■	■		
S8		371.09	■	■		■	■	■
S15		349.97	■	■				
S17		347.27	■	■	■		■	■

The petrophysical properties summarized in Table 6-1 include values determined from two different analytical techniques: helium pycnometry and mercury intrusion porosimetry (MIP). The latter of the techniques was performed using a Micromeritics AutoPore IV capable of resolving pores of diameters between 360 μm and 0.003 μm. In short, this technique relies on the properties of non-wetting liquids such as mercury to probe the pore space of materials. Non-wetting liquids have the property of not intruding pores without any external force or pressure. In contrast, water and other wetting liquids will flow into the spaces of porous material at atmospheric pressure by capillary action whereas liquid mercury will resist this force. The volume of mercury forced into the sample is proportional to the pressure applied and is represented by the Washburn equation

$$D = -\frac{4}{P}\gamma \cos\theta \ , \tag{5.1}$$

where D is the pore diameter, γ is the surface tension of the liquid, θ is the contact angle, and P is the applied pressure (Wardlaw and McKellar, 1981). Through analysis of the volume of mercury injected, the technique can provide a distribution of pore sizes within the samples

(Figure 6.4). Porosity values obtained from MIP range from 7.7% to 22.9%, differing slightly from the values calculated from the pycnometry measurements this is not unexpected due to differences in the methodologies (see for example Njiekak et al. (2018)) .

It is important to note two important limitations of the MIP method in the context of porosity determination. The first being that the mercury is only capable of intruding into the pore space that is connected to the surface of the sample material. The second limitation is that MIP analysis, much like the other laboratory methods, can only measure the properties of a small volume of sample material, which may not be representative of the rock as a whole. The first limitation suggests that closed pore space is not considered in the estimation of the total porosity, which is to say that only the connected porosity is measured. The second limitation is a particularly important consideration for this study as the Grosmont formation is an especially inhomogeneous reservoir. In order to have a representative estimate of the reservoir porosity, the volume of rock material needed would be beyond the capabilities of MIP analysis. In addition, many of the pores, including the vug porosity seen throughout the cores, have dimensions larger than the upper limit of resolution for the porosimeter. Therefore, the pore volume measured through MIP only include intercrystalline and interparticular porosity, small fractures, and other micro-scale features.

X-ray powder diffraction (XRD) analysis was conducted using a Rigaku Ultima IV diffractometer to qualitatively identify major constituent minerals (Table 6-2). The samples from both wells are composed mainly of dolomite and quartz with trace amounts of the other minerals. The pore structure in oil bearing rocks is an important property when it comes to hydrocarbon production and as such, the characterization of such properties is a significant aspect of reservoir analysis. There have been numerous efforts to study the microstructure through scanning electron microscopy (SEM) and thin sections (Luo et al., 1994; Luo and Machel, 1995), however, due to the high degree of heterogeneity in the Grosmont Formation, it is imperative that we study these properties on a sample-to-sample basis. As such, high

resolution SEM images were acquired of the samples using a Zeiss EVO LS15 EP-SEM (Figure 6.3). Commonly observed within the samples are large euhedral dolomite crystals surrounded by intercrystal porosity as well as intracrystal dissolution porosity within the crystals themselves. These pore sizes associated with these types of porosity appear to be evenly distributed within each sample. In addition, vuggy porosity can be observed by the unaided eye and are readily seen in samples SA1, S6, S8, and to a smaller degree, S15.

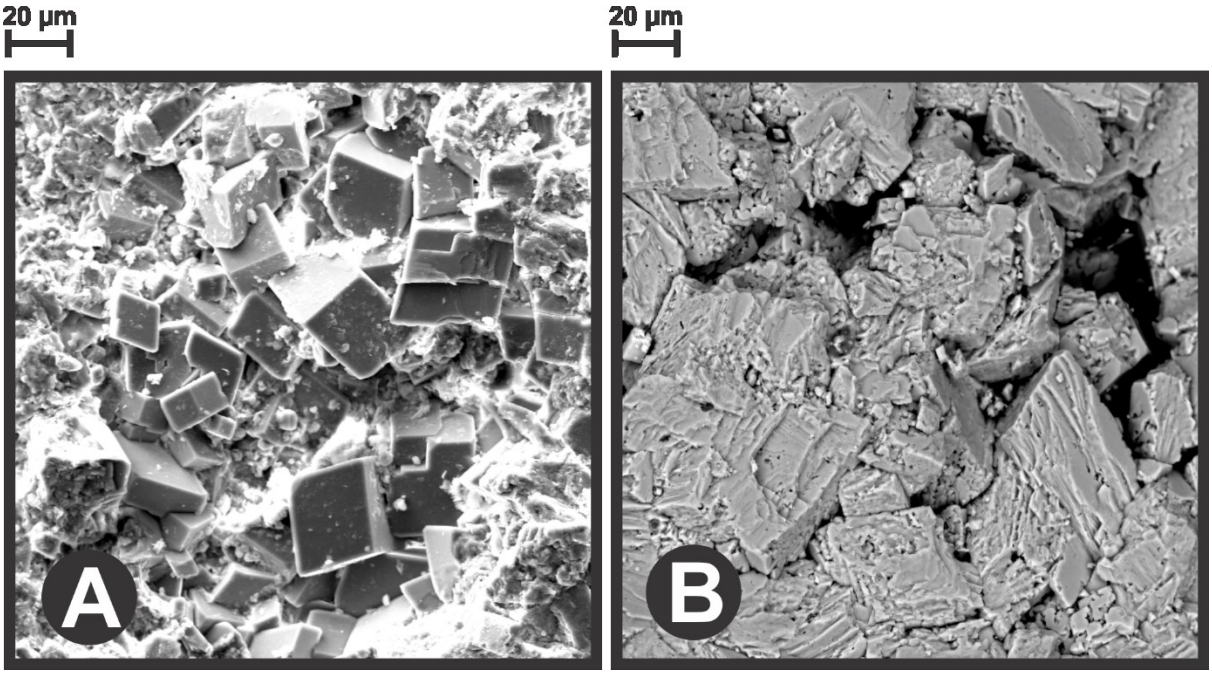

Figure 6.3. Scanning electron microscopy images of porosity found in samples. (A) Sample 3, showing euhedral dolomite crystals and intercrystal porosity. (B) Sample 6, showing intracrystal dissolution porosity in dolomite crystals and intercrystal porosity

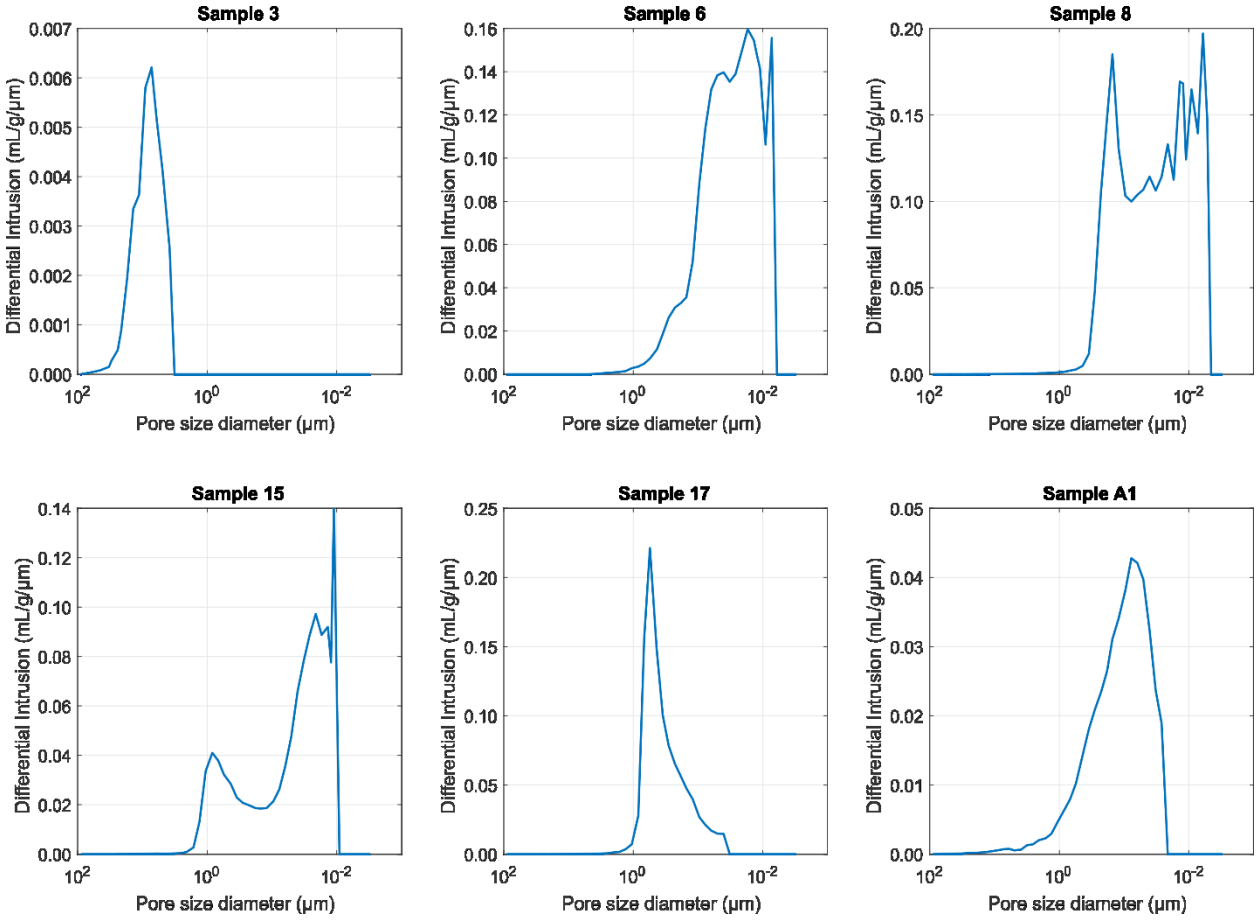

Figure 6.4. Differential mercury intrusion curves as a function of pore size diameter for samples

6.4 Ultrasonic measurements

In this contribution, the velocity of the core samples is measured directly through the widely-used Pulse Transmission Method. Since its inception, this technique has been extensively employed to estimate the ultrasonic velocity and associated dynamic moduli of geologic material subject to varying conditions.

Experimental Configuration

The main components for our experimental setup consists of an ultrasonic measurement system, a cylindrical pressure vessel, and heating / cooling system (Figure 6.5) first described in Njiekak et al. (2013). The ultrasonic measurement system comprises a pulser / receiver

(Panametrics-NDT 5800), digital oscilloscope, digitizer (NI USB-5133), and a pairs of lead zirconate titanate (PZT) ceramics manufactured by APC International Ltd. The heating / cooling system consists of a refrigerated water bath (NESLAB Endocal RTE-8DD) that circulates a water-glycol mixture around the pressure vessel through a copper tube. A "K"-type thermocouple is fed into the pressure vessel and measures the temperature of the confining fluid (internal temperature) with an accuracy of ±0.5°C.

The experimental configuration also allows for the confining and pore pressure to be adjusted independently through a combination of manual high pressure generators (HIP Model 37) and precision pumps (Quizix Q5000). It is of particular importance that we discuss such details as the elastic properties and corresponding wave speeds of the rock material are significantly dependent on the differential pressure

$$P_d = P_c - P_p \,, \tag{5.2}$$

where P_c is the confining or overburden pressure and the pore pressure, P_p is often referred to as the fluid or reservoir pressure depending on context. It is presumed that there is little change in the rock frame at constant differential pressure. As such, velocity variations observed during constant differential pressure runs can be directly attributed to the temperature and pressure dependent fluid properties.

Control of pore pressure for our samples, faces numerous challenges due to the complex structure of the rock material and viscoelasticity of the saturating fluid. One such experimental challenge is due to the time needed for pore pressure to equilibrate throughout the sample. Zimmerman (1991) estimated this amount of time needed for a local region with

$$\tau = \frac{\phi \mu \beta L^2}{k} \,, \tag{5.3}$$

where ϕ is the porosity, μ is the fluid viscosity, β is the total compressibility ($\beta_{\text{fluid}} + \beta_{\text{pore}}$), L is the characteristic length considered, and k is the permeability. This relaxation time can vary significantly between rock cores due to the large ranges of permeability, porosity, and pore types covered in our selection of samples. To complicate matters even further, the viscosity of the saturating bitumen is significantly dependently on the temperature at the time of measurement. As such, theoretical relaxation times can vary from 6 seconds to 80 hours over the course of a measurement suite. However, due to time constraints, only a maximum of 20 minutes can be allowed between measurements in practicality. Further discussions of these complications and other related challenges can be found in Rabbani et al. (2017).

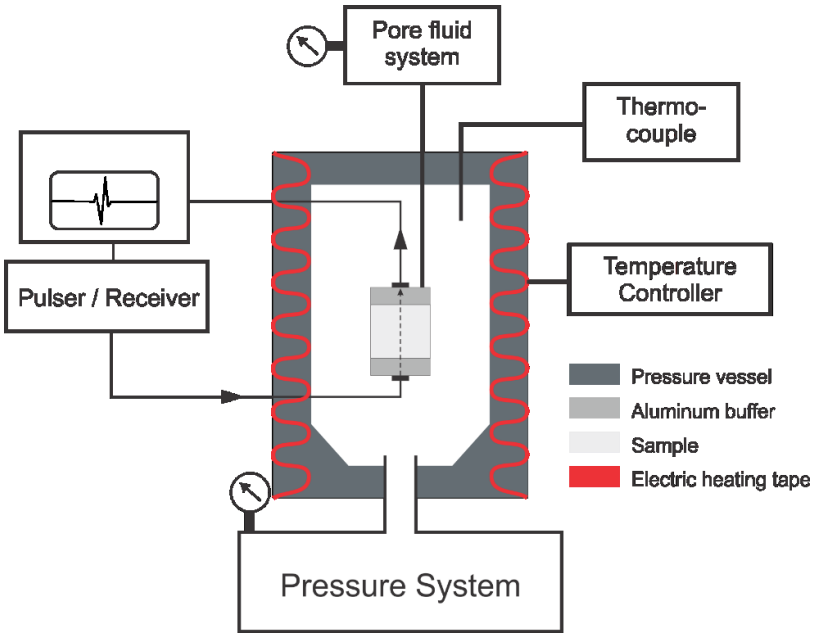

Figure 6.5: A simplified schematic of the experimental configuration. Figure from Rabbani et al. (2016) with permission granted from the Society of Exploration Geophysicists through their Fair Use Policy.

Sample preparation

Bitumen-bearing samples are preserved in deep refrigeration prior to the commencing of measurements to prevent the bitumen, which although is highly viscous, can leak out of the sample at normal room temperatures. The sample is cored to a diameter of approximately 38 mm (1.5 inches) and faces are ground on a surface grinder parallel to a tolerance of 0.1 mm. The sample, along with ultrasonic transducers, are placed together and jacketed with Kuri-Tec Klearon 73 PVC tubing.

Measurement sequence

In this study, ultrasonic velocities are measured on the samples subjected to various conditions of temperature, pressure, and saturation states. The measurement sequence for each sample consisted of the determining of P- and S-wave velocities in 4 distinct runs adapting the procedures described in Rabbani et al. (2017)

1. Initial measurement of velocities on sample with all preserved pore fluids. In this run, the pore pressure is subjected to atmospheric conditions while the confining pressure is varied up to 40 MPa.
2. Measurement of velocities on sample subjected to a constant differential pressure. Similar to the initial run, the confining pressure is increased up to 40 MPa, however in this run, the pore pressure is controlled to maintain a constant differential pressure of 7 MPa (in-situ pressure at reservoir depths).
3. Before proceeding to the dry frame run, the bitumen and other associated pore fluids are extracted from the sample through a Soxhlet extraction method using toluene as the solvent. Depending on pore and permeability of the rock material, extraction times range from a minimum of 2 weeks up to 4 weeks. Samples were determined to be void of bitumen and other pore fluids when the solvent ceases to change colour. After removal of solvent, velocities were then measured on dry frame of the rock. Pore pressure is subjected to atmospheric conditions (drained conditions) while the confining pressure is varied up to 40 MPa.

Samples are then re-saturated with water and measurements of velocities are repeated in the same conditions as run 2 (constant differential pressure of 7 MPa).

Velocity calculation and error analysis

In the Pulse Transmission Method, the pulser / receiver system produces a continuously pulsing excitation voltage to drive the piezoelectric elements in the transmitting transducer. The resulting impulse produced by the element then propagates through the sample as an ultrasonic elastic wave, which is then converted back into an electric signal through the receiving transducer. The electric signal passes through an 8-bit digitizer before being stacked and recorded on the digital oscilloscope at a rate of 10 ns/sample.

Transit times are picked from the first extremum of the waveform and calibrated to account for the transmission through the aluminum buffer of the transducers. Furthermore, this calibration step also accounts for the thermal expansion of the aluminum buffer and a system response delay associated with the excitation of the piezoelectric elements. The velocity of the sample is then simply the ratio of the sample length to the calibrated transit time.

The largest sources of error associated with this method are the determining of the sample length and transit time. As previously mentioned, the parallelism of the sample's faces is accurate to a tolerance of 0.1 mm; thus the error in sample length is the sum of that value and the uncertainty in the resolution of the instrument used to measure the sample. The error associated with picking transit times are largely dependent on the quality of the signal. In general, the quality of the signal increases with confining pressure. Despite this, the quality of the signal can vary widely from sample to sample due to the attenuative nature of the saturating bitumen.

Other sources of error may be attributed to the length shortening of samples under different pressure states as well as the hardening of the aluminum transducer buffer from temperature cycling.

6.5 Results and Discussion

The main objective of this study is to investigate the relationships between seismic properties and the changes in reservoir pressure, temperature, and saturation conditions typically observed during reservoir steaming. Ultrasonic velocity data was collected on 6 naturally-saturated carbonate samples from the Grosmont Formation under these varying reservoir conditions and then repeated for dry and water-saturated states in order to test the validity of standard fluid substitution models. As previously mentioned, this study will focus primarily on the naturally-saturated measurements while the results for the other saturation states will be delayed for future contributions. Table 6-3 shows the total number of valid velocity measurements recorded for each saturation condition after quality control checks. Due to attenuation and poor signal quality at higher temperatures, many of the measurements were discarded. Figure 6.6 shows an example of the P- and S-waveforms from which the transit times were picked. It is important to note that much of the decrease in waveform amplitude, especially in the S-wave data, is largely attributed to transducer temperature effects in addition to the changes in physical properties of the measured samples. Consequently, to properly estimate the degree of attenuation as a result of changes in the rock and fluid properties, this transducer effect must be accounted for.

Table 6-3. Total number of valid velocity measurements for various saturation conditions

	P-wave					
	SA1	**S3**	**S6**	**S8**	**S15**	**S17**
Natural saturation	230	237	80	80	79	60
Dry frame	115	115	40	40	40	20
Water saturation	115	115	40	40	40	40

	S-wave					
	SA1	**S3**	**S6**	**S8**	**S15**	**S17**
Natural saturation	184	144	80	80	79	79
Dry frame	115	92	39	40	40	40
Water saturation	115	69	40	40	40	40

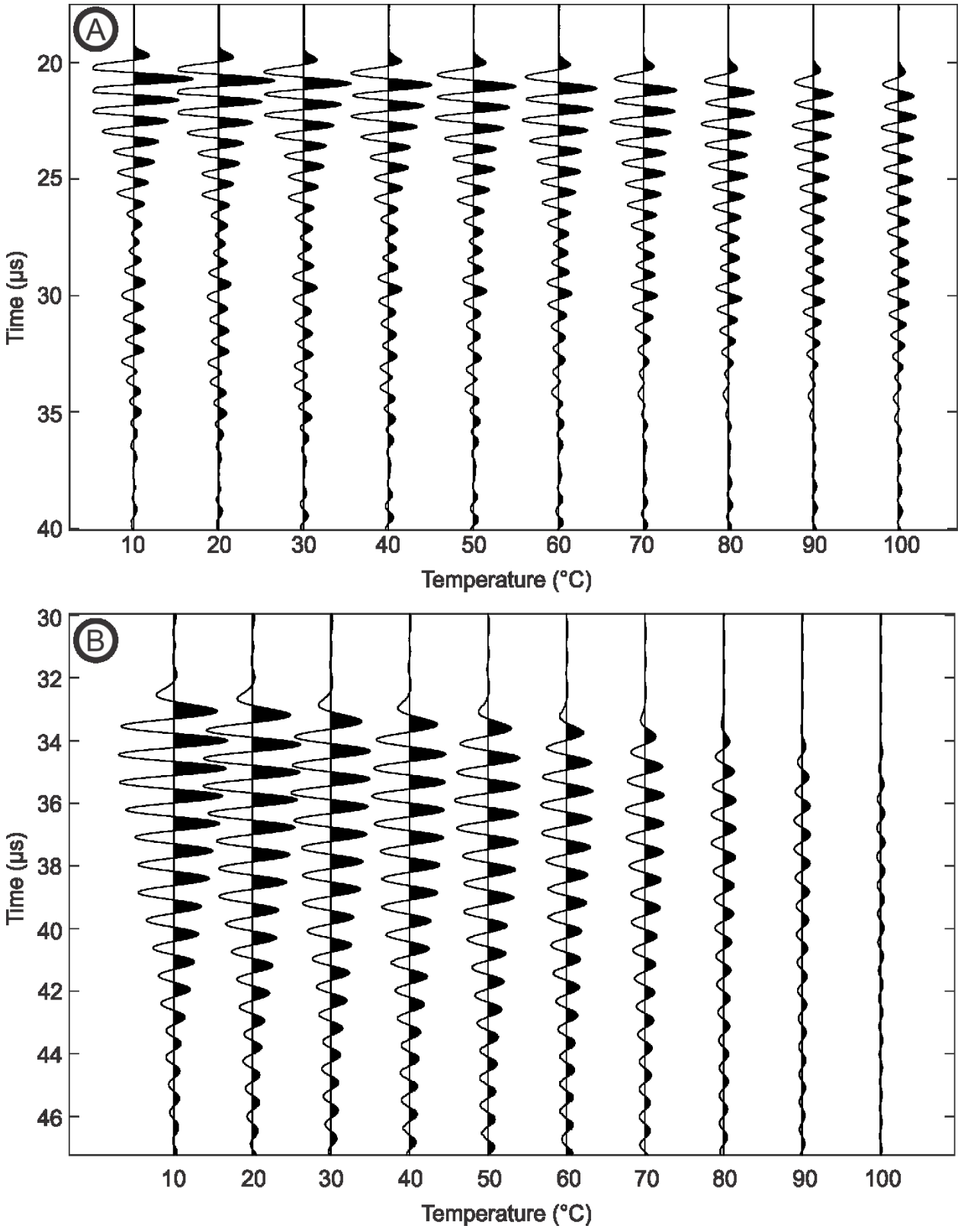

Figure 6.6: Example of a) P-wave and b) S-wave waveforms for the temperature range 10°C – 100°C for naturally saturated sample 15 subjected to 20 MPa differential pressure

Figure 6.7 shows the velocity measurements plotted as a function of temperature and differential pressure for all samples under drained conditions. Due to the large number of data points, the effects due to temperature and pressure changes are not readily apparent when visualized in a 3D plot. As such, the effects resulting from temperature and pressure variations will be analyzed and discussed independently around Figures 6.8 - 6.10.

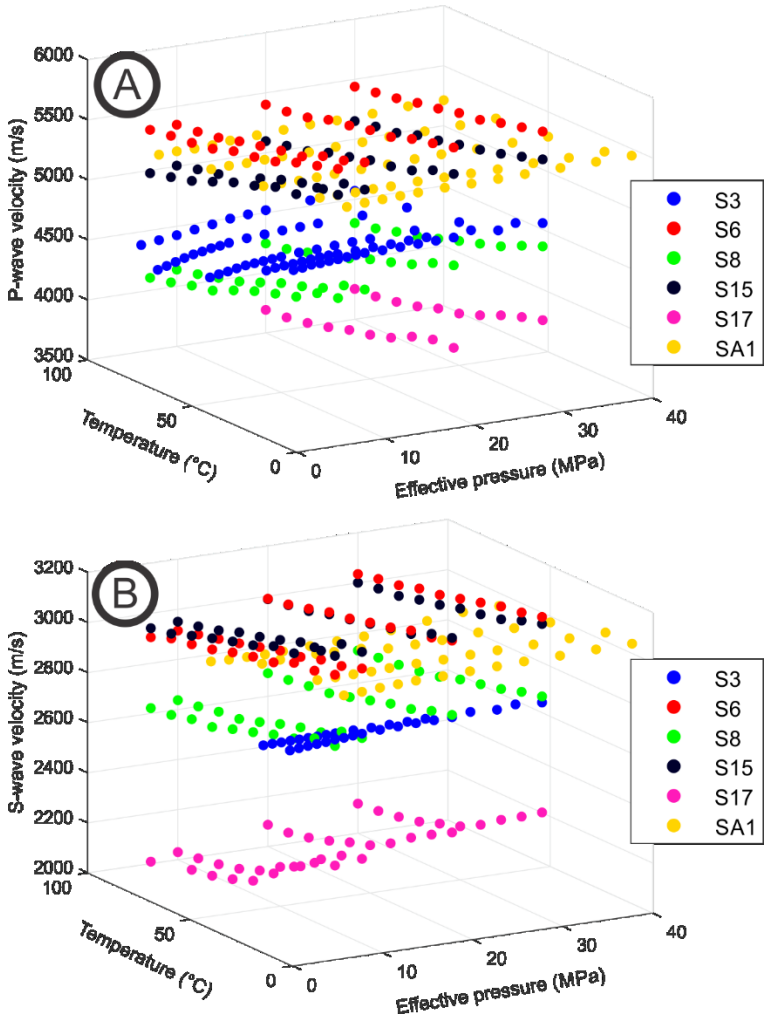

Figure 6.7. Plots of ultrasonic a) P-wave and b) S-wave velocities as a function of temperature and differential pressure for bitumen-saturated sample runs

Temperature dependence

As previously mentioned, the seismic velocity of bitumen-bearing rocks are highly temperature dependent due in part due to the large changes in the physical properties of the saturating fluid. With increasing temperature, bitumen viscosity drops significantly resulting in a decrease in fluid bulk and shear moduli. These fluid effects can be seen directly through sample measurements in Figure 6.8, where the P- and S-wave velocities, as well as associated moduli are plotted for all bitumen-saturated samples subjected to 20 MPa differential pressure. For an isotropic medium, we define the P- and S-wave velocities in terms of the bulk density and the bulk and shear moduli using the following relations

$$V_P = \sqrt{\frac{K + \frac{4}{3}\mu}{\rho_b}}\,, \tag{5.4}$$

$$V_S = \sqrt{\frac{\mu}{\rho_b}}\,. \tag{5.5}$$

Trends show all velocities and moduli show a steady monotonic decrease with increasing temperature. Over the range of 10°C – 100°C, average P- and S-wave velocities decreased by 8.3% and 7.7% respectively. In contrast, for measurements conducted on the dry frame of the sample (all pore fluids removed), both P- and S-wave velocities decreased by 1.8% over the same range of temperatures. These values are consistent with theory as we would expect the temperature dependence of the rock frame to be insignificant in comparison to that attributed to fluid effects. However, the slight temperature dependence on velocity and moduli should still be carefully considered in the context of fluid substitution models.

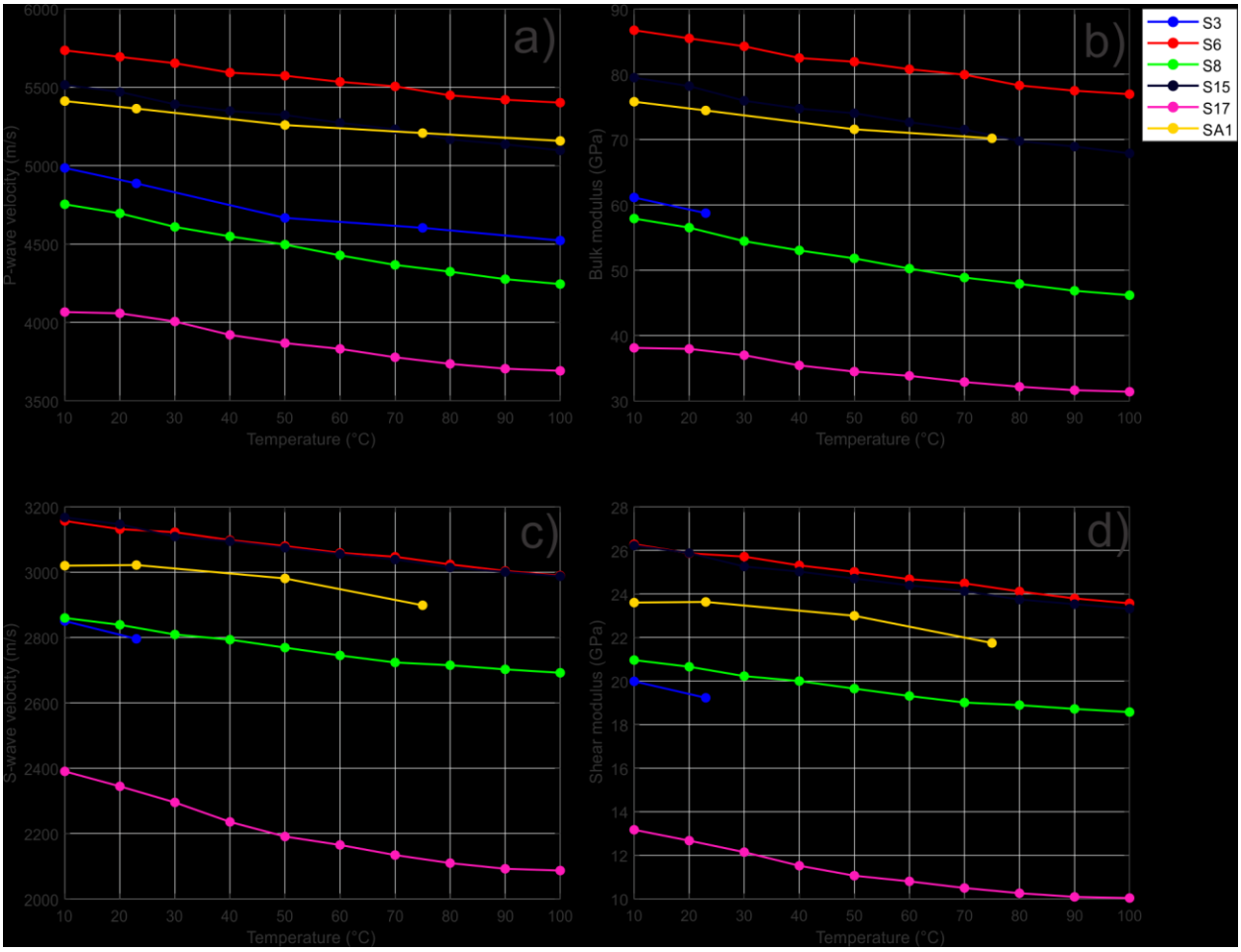

Figure 6.8. Effects of temperature under 20 MPa differential pressure on a) P-wave velocity, b) bulk modulus, c) S-wave velocity, and d) shear modulus for bitumen-saturated samples under drained conditions

Pressure dependence

In addition to the temperature dependence of samples, the effect of varying pressure conditions on the rocks should be thoroughly characterized. Heavy oil reservoirs are often subjected to elevated levels of pore pressure during steaming operation and the resulting changes in the stress state can drastically affect the seismic velocity of the reservoir. Figure 6.9 shows the P- and S-wave velocities and well as moduli for bitumen-saturated samples for a range of confining pressures. Generally speaking, the increase in confining pressures will result in the closure of cracks and other compliant pore spaces. Consequently, these closures

increase the efficiency for acoustic wave propagation through the material, resulting in an increase in bulk and shear moduli, and P- and S-wave velocities. This effect is typically associated with a non-linear upward trend in velocity at low levels of confining pressure with the closure of cracks, followed by a linear increase at high pressures. This effect appears to be relatively weak in our samples and may be indicative of low concentrations of compliant pore space in the rock material.

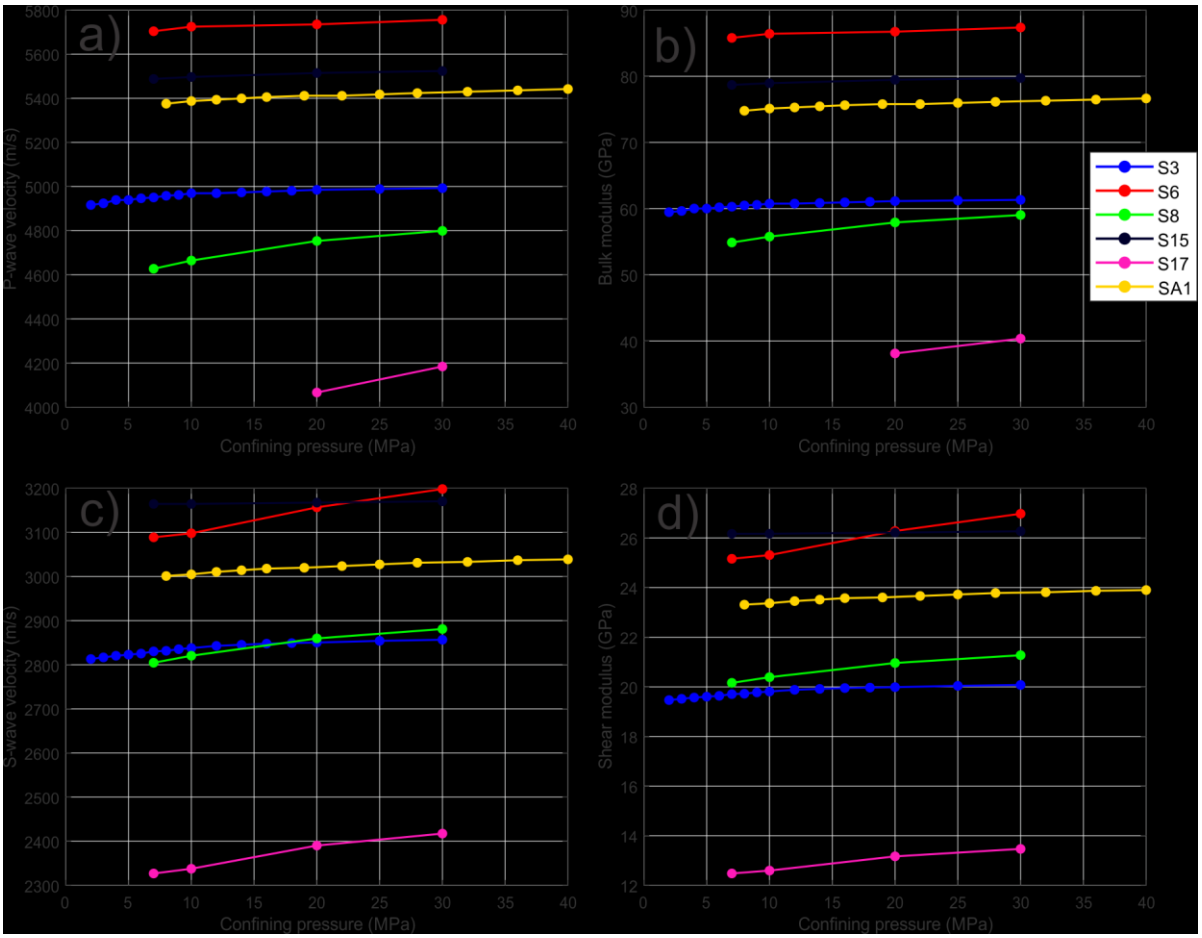

Figure 6.9. Effects of confining pressure at 10°C for a) P-wave velocity, b) bulk modulus, c) S-wave velocity, and d) shear modulus for bitumen-saturated samples under drained conditions

Changes in pore pressure can also drastically affect the seismic velocity due to its effect on the fluid moduli and density, and indirectly, the rock frame. Figure 6.10 shows the P- and S-wave velocities for sample 3 plotted as a function of confining pressure, however, for this

measurement run, the sample was held at a constant 7 MPa differential pressure (the approximate in-situ pressure condition at depth in the actual reservoir). The properties of the rock frame are presumed to be dependent only on the differential pressure, therefore by varying the confining and pore pressure by the same amount (i.e. by maintaining the sample at constant differential pressure), the fluid effect within the rock is more readily observed. Both P- and S-wave velocities increase linearly with pore pressure and is most likely attributed to the increase in bulk and shear modulus of the bitumen.

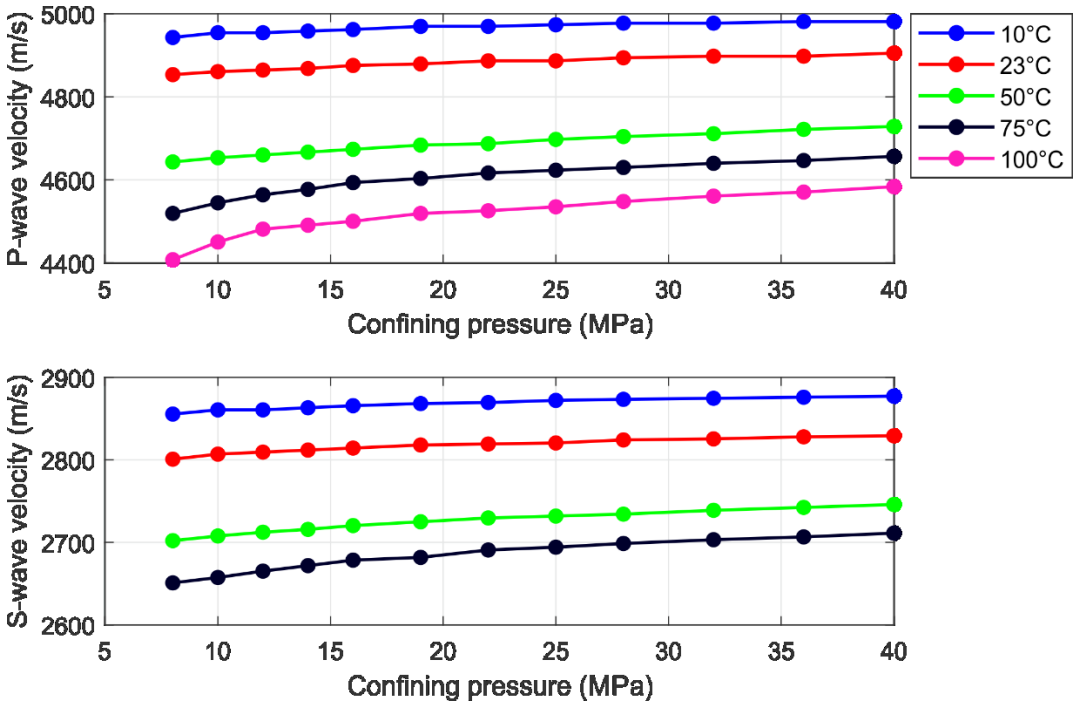

Figure 6.10. P- and S-wave velocities as a function of confining pressure for sample 3. Sample was held at a constant differential pressure of 7 MPa (i.e pore pressure Pp = Pc – Pe)

6.6 Principal component analysis (PCA)

One of the major goals of this contribution is to establish a predictive relationship between the observed ultrasonic velocities and the petrophysical parameters, pressures, and temperatures which influence said velocities. This is typically achieved by performing multiple regressions on the dataset, however, one should have a thorough understanding of the

relationships that exist between the predictors that are input to the model. In multiple regression, one major difficulty with the typical least squares estimators is the problem of "multicollinearity", which arises when two or more of the predictor variables are highly correlated (Montgomery et al., 2001). Multicollinearity can lead to issues where the regression may output incorrect estimations of the regression coefficients among other statistical problems (Gunst, 1983).

There are many ways to address the issue of multicollinearity and one common method is to input only a subset of predictor variables into the regression model. By carefully selecting a subset of variables that do not contain multicollinearities, we can avoid the problem all together. To select these variables, and study the statistical relationships between them, we employ the use of *principal component analysis* (PCA). Within the field of geophysics, PCA has a wide range of applications for the processing and interpretation of geophysical datasets (Davydenko and Grayver, 2014; Guo et al., 2009; Roden et al., 2015; Xie et al., 2017), however, to the best of our knowledge reported instances of its use on ultrasonic rock physics data are limited (Akarapatima and Prasad, 2017).

Principal component analysis is most commonly used in multi-variate analysis as a tool to reduce the dimensionality of a given data set while retaining as much as possible the trends and patterns currently present in said data set. PCA accomplishes this by projecting the data onto lower dimensions called "principal components (PC)" with the goal of describing the dataset using a limited number of PCs. In this new coordinate system, the dimensions are orthogonal (and hence linearly independent) and ranked according to the greatest variance projected by the dataset. This means the first principal component (PC1) explains the largest variance, followed by the second principal component (PC2) with the second largest variance, and so forth. Assuming that variance is a significant factor in how important a variable is with respect to a given dataset, this effectively means that the most important PCs occur first.

In short, PCA is performed by computing a set of eigenvectors (principal components) and its associated eigenvalues for the covariance matrix of the dataset. Each eigenvalue is proportional to the total variance represented by its corresponding PC. At this step, regression can then be applied directly to the transformed dataset by inputting PCs as predictor variables, reducing the effects of multicollinearity. This technique of performing regression directly on the transformed dataset is often referred to as *principal component regression*. It is important to note that this method is not used in this contribution as we want the predictors of the outputted regression model to contain the original variables we started out with (pressure, temperature, petrophysical parameters). Thus, principal components are only used for the selection of variables to be inputted into our regression. A full mathematical description of PCA and its applications can be found in (Jolliffe, 2002).

Our full-dimension dataset includes the following potential predictor variables: temperature, differential pressure, porosity, grain density, as well as dry and bitumen-saturated bulk densities. The values of these variables are organized into a data matrix X of order $n \times p$,

$$X = \begin{pmatrix} x_{11} & x_{12} & \cdots & x_{1p} \\ x_{21} & x_{22} & \cdots & x_{2p} \\ \vdots & \vdots & \ddots & \vdots \\ x_{n1} & x_{n2} & \cdots & x_{np} \end{pmatrix}, \tag{5.6}$$

where rows of the matrix correspond to observations and columns correspond to variables. Due to the difference in units, each variable is first normalized by their mean and standard deviation. The covariance matrix C is then calculated as

$$C = \frac{1}{n-1}(X - \bar{X})(X - \bar{X})^T, \tag{5.7}$$

This symmetric covariance matrix can then be diagonalized as:

$$C = ULU^T, \tag{5.8}$$

where U is an orthonormal matrix of eigenvectors, and L is a diagonal matrix containing eigenvalues λ_i on the diagonal elements. The values of the eigenvectors make up the principal components and are often referred to as *component loadings*. The eigenvalues are called PC scores and represent the variance corresponding to each principal component axis.

Principal component analysis was performed on the P-wave bitumen-saturated dataset to identify potential predictor variables for the regression model. The next step is to determine the number of variables needed to adequately account for the variation in the original dataset. The method in which this is achieved varies between disciplines, with both numerical and qualitative approaches employed to determine this number. In practice, the criteria and its justification are generally intuitive, although they will typically make use of a number of statistically based rules. A detailed discussion of these rules and methods is covered by Jolliffe (2002).

One common way to determine the number of variables needed is to analyze the proportion of variance represented by each principal component. This value is calculated by dividing each individual PC score (eigenvalues) by the its total sum and is shown in Table 6-4. Examination of the table will show that the first PC accounts for more than half the total variance present in the dataset. The second, third, and fourth PCs contribute much less to the total variance of the dataset, however are still significant. The rest of the PCs account for 1% or less of the variance and one might suggest that it is reasonable to discard those components.

Similar variance-based methods include analyzing the shape of the log of eigenvalues plotted as a function of PC number (Farmer, 1971), as well as the cumulative variance represented by the PCs (Figure 6.11). To determine the cutoff point, authors have historically outlined a variety of rules, which include looking for changes in slope, picking the "elbow" of the curve, or picking the point in which the curve transitions to a straight line. For our study, we choose to follow the procedure of picking the elbow of the curve, which would suggest the retention

of 4 or 5 principal components. Combined with the earlier notion of discarding the last two PCs, we will choose to settle with retaining 4 total PCs.

Now that we've determined how many principal components to retain, we will analyze which predictor variables significant, and just as important, which predictor variables are correlated. The component loadings in which are substantial are highlighted in Table 6-4 for the first four PCs, which are determined by analyzing the magnitude of the loadings (higher magnitudes are more likely to be significant). This suggests that porosity, and the dry and saturated bulk densities contribute most to the velocity variations within the dataset as well as their strong correlation with one another. This is expected as the porosity directly controls the fraction of solid and fluid phases within the rock. However, this would mean that only one of these variables can be input as a predictor into the regression model. Analysis of the other significant PCs would suggest that temperature and pressure are both significant variables that contribute to the velocity variations in approximately equal amounts. It also suggests that grain density is a relatively important factor that should be included as it will be related to the frame modulus of the rock.

Table 6-4. Loadings (eigenvalues) for each principal component (eigenvectors)

	PC1	PC2	PC3	PC4	PC5	PC6
T	0.01	0.93	0.37	-0.08	0.00	0.00
P_c	0.08	-0.37	0.93	0.01	0.03	0.00
ϕ	-0.53	0.02	0.03	0.29	0.47	0.64
ρ_g	0.39	0.09	-0.02	0.89	0.11	-0.17
ρ_b (dry)	0.54	0.00	-0.03	-0.04	-0.37	0.75
ρ_b (bitumen-saturated)	0.52	-0.00	-0.07	-0.33	0.79	-0.01

							Total
Variance Explained (%)	55.55	16.76	16.39	10.28	1.02	0.00	100

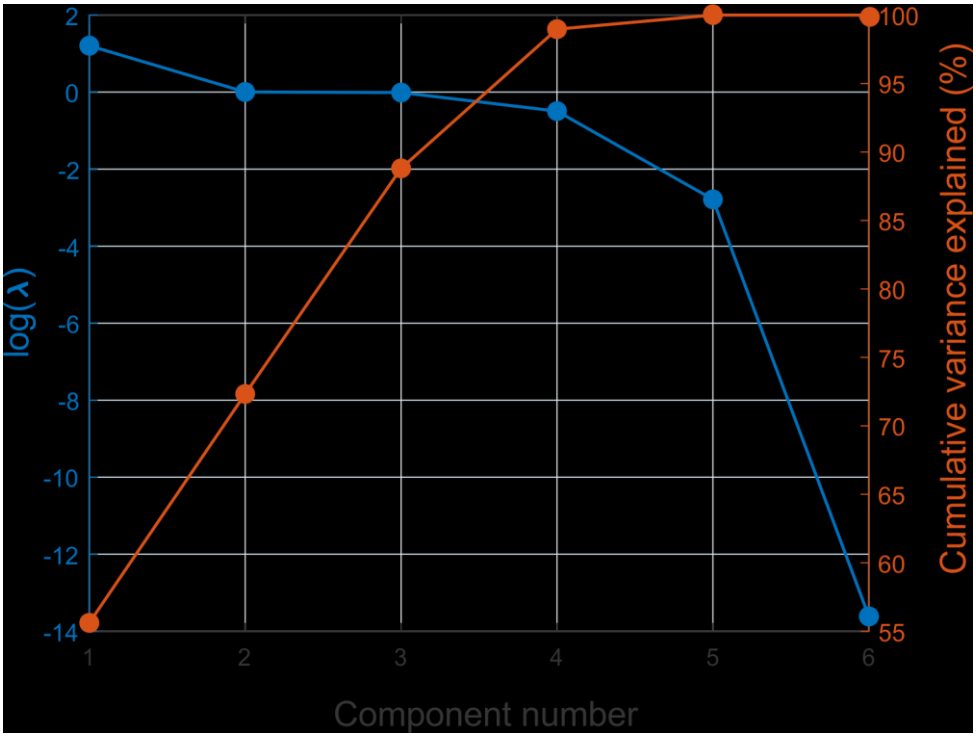

Figure 6.11: Plot of cumulative variance explained in percentage (orange) and log of eigenvalues (blue) corresponding to each principal component

6.7 Empirical relationships

With our chosen predictor variables, a linear multiple regression model was created to produce an empirical relationship of the form

$$V_{P/S} = \mathrm{B}_1 + \mathrm{B}_2 T + \mathrm{B}_3 P_c + \mathrm{B}_4 \phi + \mathrm{B}_5 \rho_g \,, \tag{5.9}$$

where $V_{P/S}$ is the ultrasonic P- or S-wave velocity in (m/s), T is the temperature in (°C), P_d is the confining pressure in (MPa), ϕ is the porosity in percentage, ρ_g is the grain density (kg/m^3), and B_N are the coefficients to be determined by the multiple linear regression. As all predictor variables that are used in the model show relatively linear relationships with both P- and S-wave velocities, a simple linear model was used. Typically, an exponential term is used to describe the non-linear behaviour of wave velocities with differential or confining

pressure (Eberhart-Phillips et al., 1989; Zimmerman et al., 1986), however, this effect is observed to be weak in our samples over the range of pressures they were subject to. The inclusion of an exponential term in the regression model only marginally increased the R^2 value, therefore it can be argued that simple linear model can adequately describe the variations in wave velocities.

A total number of 553 and 494 observations were used in the P-wave and S-wave regression models, respectively. Differences in the number of observations were primarily due to the contrast in data quality between P-wave and S-wave data. The resulting coefficients produced by the regression for bitumen-saturated samples are displayed in Table 6-5, and when input into Equation 9, can describe the P- and S-wave velocities as a function of the temperature, pressure, and petrophysical properties of the individual rocks.

Table 6-5. Multiple linear regression model for bitumen-saturated samples

		Predictor	Coefficient	P-value	R^2
P-wave	B_1		1.56E+04		0.78
	B_2	Temperature (°C)	-4.66E+00	2.5E-36	
	B_3	Confining pressure (MPa)	3.30E+00	2.3E-03	
	B_4	Porosity (%)	-1.03E+04	5.7E-164	
	B_5	Grain density (kg/m^3)	-3.31E+00	6.2E-30	
S-wave	B_1		6.99E+03		0.82
	B_2	Temperature (°C)	-2.51E+00	8.9E-29	
	B_3	Confining pressure (MPa)	1.08E+00	7.3E-02	
	B_4	Porosity (%)	-5.30E+03	9.3E-163	
	B_5	Grain density (kg/m^3)	-1.22E+00	3.65E-12	

Assuming a significance level of 0.05, analysis of the p-values for each computed coefficient suggests that out of the four predictors input into our regression model, confining pressure is the least significant contributor to the velocity changes. This hypothesis is consistent with theory as the largest velocity changes in the bitumen-saturated samples are expected to be

due to the changes in fluid properties (e.g. Rabbani and Schmitt, 2018). From initial observations, the influence of confining pressure in these samples is smaller than that typically observed in clastic rocks. The lower pressure dependence may be the result of post-depositional processes such as cementation and recrystallization, which can increase the rigidity and competence of the rock frame (Anselmetti and Eberli, 1993). This effect can also be attributed to inclusion of high aspect ratio pores as opposed to the more compliant low aspect ratio cracks (Bakhorji, 2010; Wang et al., 2018).

In addition to the analysis of the p-values, it can also be useful to directly compare the regression coefficients of the standardized data set (Table 6-6). In this type of regression, velocity and predictor variables are standardized by subtracting its mean and dividing by its standard deviation. Standardized regression models are particularly useful when dealing with the issue of multicollinearity, however, since this issue was addressed prior to the initial regression, this model is most useful for interpreting the significance of predictor variables. As a result, p-values output from the regression do not change from the standardization of the dependent and independent variables.

Table 6-6. Standardized Multiple linear regression model for bitumen-saturated samples

		Predictor	Coefficient	P-value	R^2
P-wave	B_1		-0.08		0.78
	B_2	Temperature (°C)	-0.27	2.5E-36	
	B_3	Confining pressure (MPa)	0.06	2.3E-03	
	B_4	Porosity (%)	-1.00	5.7E-164	
	B_5	Grain density (kg/m^3)	-0.29	6.2E-30	
S-wave	B_1		-0.06		0.82
	B_2	Temperature (°C)	-0.26	8.9E-29	
	B_3	Confining pressure (MPa)	0.04	7.3E-02	
	B_4	Porosity (%)	-0.90	9.3E-163	
	B_5	Grain density (kg/m^3)	-0.18	3.65E-12	

Similar to the observations from PCA, the coefficients output by the standardized regression suggests that porosity and grain density are the most statistically significant, followed by temperature and confining pressure.

6.8 Conclusion

An ultrasonic velocity study was conducted on a set of 6 bitumen-saturated carbonate rocks taken from the Grosmont Formation of Alberta, Canada. Samples were measured under a variety of pressure, temperature, and fluid saturation conditions similar to that expected during reservoir steaming operations in order to study their effects on the seismic velocity.

As expected, for bitumen-saturated samples, substantial changes in P- and S-wave velocities were observed in relation to temperature variations. These effects are likely attributed to the strong temperature dependence of the fluid properties as experiments under similar conditions for the dry rock frame exhibited little velocity variations. The effects of different pressure conditions were also analyzed and concluded that due to the stiff frame of the rock, variations in velocities due to confining pressure changes were minimal in comparison to the response in clastic rocks. However, for bitumen-saturated samples, increases in pore pressure can increase both P- and S-wave velocities due to its effects on the pore fluid.

In addition to the velocity measurements, each sample underwent sample characterization and basic petrophysical properties were measured in the laboratory. Multivariate analysis was performed on the entire dataset and empirical relationships were established between P- and S-wave velocities and basic parameters such as temperature, confining pressure, and porosity. These relationships are summarized in the last section.

The relationships established in this study are a reasonable fit for this data set, however, due to the high heterogeneity of the Grosmont Formation, it is unlikely that any one model will describe entire reservoir at formation scale. Despite this, these empirical relationships can

still be useful for the interpretation of 4D seismic monitoring data. Future work to improve this model includes a more thorough sample characterization process that classifies different porosity types as well as further study of the rock matrix and fluid composition. Furthermore, these measurements were conducted at ultrasonic frequency range, however, measurements at seismic frequencies should be completed before the application of this model for seismic data.

7 Conclusions

The Devonian Grosmont formation is a large carbonate platform complex which holds a significant portion of Canada's bitumen reserves. The heterogeneity of the reservoir, arising from its complicated diagenetic history, makes the Grosmont formation an extremely difficult resource to exploit. Time-lapse seismic methods can potentially play a role in reducing the economic and environmental risks associated with production of such a reservoir, however, quantitative interpretation of 4D seismic data requires a solid understanding of the reservoir's rock properties. Specifically, one must understand how the physical properties of the rocks change in response to the high temperature and pressure conditions commonly observed during steam injection into heavy oil reservoirs. It is also necessary to develop a comprehension of how the changes in those physical properties govern the overall seismic response. This thesis aimed to contribute to that understanding through ultrasonic velocity measurements of Grosmont formation rocks, carried out under various temperature, pressure, and saturation conditions.

Significant decreases in P- and S-wave velocities with increasing temperatures were observed for samples with natural-saturation of bitumen. In comparison, for the dry frame, the velocity decrease over the same temperature range were minimal, however, is still significant and should be considered during fluid substitution modelling. These observations were consistent with the presumption that fluid effects govern the changes observed in time-lapse seismic data. P- and S-wave velocities were observed to increase with confining pressure for all samples with the exception of the dry run for Sample 6. The increase is likely attributed to the closure of microcracks and fractures within the rock material. Additionally, P- and S-wave velocities increase with pore pressure for both naturally-saturated and water-saturated samples. Differential pressure for these runs is maintained at a constant 7 MPa, and as such, suggests that the increase in velocities is primarily attributed to an increase in fluid bulk and shear moduli as a result of increased pore pressure.

In Chapter 6, a version of Ong et al. (2018) is given in its entirety, which focuses on the development of a rock physics template using the ultrasonic velocity measurements completed for this thesis. Prior to regression of measurements, principal component analysis (PCA) was completed for the dataset to highlight correlations and potential multi-collinearity issues. As expected, PCA showed that porosity, temperature, pressure, and grain density were the main factors that contributed to the velocity variations within and between samples for the dataset. Empirical relations were established through multiple linear regressions of the dataset with the final relationship in the form of Equation 6.9 and coefficients listed in Table 6-5.

7.1 Suggestions for future research

An important area of research not extensively covered in this thesis is the topic of fluid substitution. The effects of fluid saturation on ultrasonic velocities were only briefly discussed due to the scope of this thesis, however, future contributions will focus on these topics. In particularly, the wide range of laboratory measurements provide an excellent opportunity for comparison with the responses of common fluid substitution models.

Furthermore, the suite of measurements discussed in this thesis were conducted in the ultrasonic frequency range. The viscoelastic properties of heavy oil bearing rocks are significantly frequency dependent with velocity dispersion commonly observed within the seismic bandwidth (Das and Batzle, 2010). While these measurements can provide insight into the behavior of heavy oil saturated rocks under various conditions, there is an absolute necessity to complete these measurements for the full frequency spectrum. In addition, the topic of attenuation is also of great importance for the interpretation of time-lapse seismic data due to its relationship with heavy oil viscosity. However, due to the temperature dependent transducer effects, this property cannot be studied directly from this suite of measurements without a prior calibration step to account for the decrease in wave amplitudes.

As such, an investigation into the degree of attenuation in these samples will be left for future research.

8 References

Adam, L., Batzle, M., Brevik, I., 2006. Gassmann's fluid substitution and shear modulus variability in carbonates at laboratory seismic and ultrasonic frequencies. Geophysics 71, F173–F183.

Ahr, W.M., 2011. Geology of Carbonate Reservoirs The Identification, Description and Characterization of Hydrocarbon Reservoirs in Carbonate Rocks. John Wiley & Sons.

Akarapatima, T., Prasad, M., 2017. Multivariate Analysis of Physical and Elastic Properties in Sandstones, in: AGU Fall Meeting 2017.

Anselmetti, F.S., Eberli, G.P., 1993. Controls on sonic velocity in carbonates. Pure Appl. Geophys. PAGEOPH 141, 287–323. https://doi.org/10.1007/BF00998333

Ardakani, E.P., Schmitt, D.R., Bown, T.D., 2014. Case History Detailed topography of the Devonian Grosmont Formation surface from legacy high-resolution seismic profiles , Northeast Alberta. Geophysics 79.

Assefa, S., McCann, C., Sothcott, J., 2003. Velocities of compressional and shear waves in limestones. Geophys. Prospect. 51, 1–13. https://doi.org/10.1046/j.1365-2478.2003.00349.x

Baechle, G.T., Eberli, G.P., Weger, R.J., Massaferro, J.L., 2009. Changes in dynamic shear moduli of carbonate rocks with fluid substitution. Geophysics 74, E135–E147. https://doi.org/10.1190/1.3111063

Bakhorji, A.M., 2010. Laboratory Measurements of Static and Dynamic Elastic Properties in Carbonate.

Barrett, K.R., 2016. Reservoir geology of the Grosmont Formation Bitumen Steam Pilot, Saleski, Alberta. Bull. Can. Pet. Geol. 64, 147–165.

https://doi.org/10.2113/gscpgbull.64.2.147

Bass, J.D., 1995. Elasticity of minerals, glasses, and melts. American Geophysical Union (AGU), pp. 45–63. https://doi.org/10.1029/RF002p0045

Batzle, M., Hofmann, R., Han, D.-H., 2006. Heavy Oils – Seismic Properties. Lead. Edge 25, 750–756. https://doi.org/10.1190/1.1851162

Batzle, M., Wang, Z., 1992. Seismic properties of pore fluids. Geophysics 57, 1396–1408. https://doi.org/10.1190/1.1443207

Belyea, H.R., 1952. Notes on the Devonian system of hte north-centra plains of Alberta, Geological Survey of Canada.

Berryman, J.G., 1981. Elastic wave propagation in fluid-saturated porous media. J. Acoust. Soc. Am. 69, 416. https://doi.org/10.1121/1.385457

Best, A.I., 1997. The effect of pressure on ultrasonic velocity and attenuation in near-surface sedimentary rocks. Geophys. Prospect. 45, 345–364. https://doi.org/10.1046/j.1365-2478.1997.00344.x

Bhatia, A.B. (Avadh B., Singh, R.N., 1986. Mechanics of deformable media. A. Hilger, published in association with the University of Sussex Press.

Bianco, E., Kaplan, S., Schmitt, D., 2008. Seismic rock physics of steam injection in bituminous oil reservoirs. Lead. Edge 27, 1132–1137.

Biot, M.A., 1956a. Theory of Propagation of Elastic Waves in a Fluid-Saturated Porous Solid. I. Low-Frequency Range. J. Acoust. Soc. Am. 28, 168. https://doi.org/10.1121/1.1908239

Biot, M.A., 1956b. Theory of Propagation of Elastic Waves in a Fluid Saturated Porous Solid. II. Higher Frequency Range. J. Acoust. Soc. Am. 28, 179–191.

https://doi.org/10.1121/1.1908241

Birch, F., 1961. The Velocity of Compressional Waves in Rocks to 10 kilobars, Part 2. J. Geophys. Res. 66, 2199–2224. https://doi.org/10.1029/JZ066i007p02199

Birch, F., 1960. The Velocity of Compressional Waves in Rocks to 10 Kilobars, Part 1. J. Geophys. Res. 95, 1083–1102.

Bos, L., Gibson, P., Kotchetov, M., Slawinski, M., 2004. Classes of anisotropic media: A tutorial. Stud. Geophys. Geod. 48, 265–287. https://doi.org/10.1023/B:SGEG.0000015596.68104.31

Bouzidi, Y., 2003. The acoustic reflectivity and transmissivity of liquid saturated porous media: experimental tests of theoretical concepts.

Bown, T.D., 2011. Legacy Seismic Investigations of Karst Surfaces: Implications for Heavy Oil Extraction From the Devonian Grosmont Formation, Northeastern Alberta, Canada.

Bukhari, S., Islam, M., Haziot, A., Beamish, J., 2014. Shear piezoelectric coefficients of PZT, LiNbO3and PMN-PT at cryogenic temperatures. J. Phys. Conf. Ser. 568. https://doi.org/10.1088/1742-6596/568/3/032004

Burrowes, A., Marsh, R., Teare, M., Evans, C., Ramos, S., Rokosh, D., Rahnama, F., Kirsch, M.-A., Philp, L., Stenson, J., Yemane, M., Horne, J. Van, Fong, J., Ashrafi, B., Sankey, G., 2010. Alberta's Energy Reserves 2009 and Supply/Demand Outlook.

Buschkuehle, B.E., Hein, F.J., Grobe, M., 2007. An Overview of the Geology of the Upper Devonian Grosmont Carbonate Bitumen Deposit, Northern Alberta, Canada. Nat. Resour. Res. 16, 3–15. https://doi.org/10.1007/s11053-007-9032-y

Cadoret, T., Poirier, J.-P., 1993. Effet de la saturation eau-gaz sur les proprietes acoustiques des roches : Etude aux frequences sonores et ultrasonores. http://www.theses.fr.

Chadwick, A., Williams, G., Delepine, N., Clochard, V., Labat, K., Sturton, S., Buddensiek, M.-L., Dillen, M., Nickel, M., Lima, A.L., Arts, R., Neele, F., Rossi, G., 2010. Quantitative analysis of time-lapse seismic monitoring data at the Sleipner CO2 storage operation. Lead. Edge 29, 170–177. https://doi.org/10.1190/1.3304820

Christensen, R.M., 1982. Theory of viscoelasticity : An introduction. Academic Press.

Ciz, R., Shapiro, S.A., 2007. Generalization of Gassmann equations for porous media saturated with a solid material. Geophysics 72, A75–A79.

Cutler, W.G., 1983. Stratigraphy and sedimentology of the Upper Devonian Grosmont formation, Northern Alberta. Bull. Can. Pet. Geol. 31, 282–325.

Daridon, J.L., Lagourette, B., Xans, P., Montel, F., 1998. Petroleum characterization from ultrasonic measurement. J. Pet. Sci. Eng. 19, 281–293. https://doi.org/10.1016/S0920-4105(97)00050-8

Das, A., Batzle, M., 2010. Frequency dependent elastic properties and attenuation in heavy-oil sands : comparison between mea- sured and modeled data SEG Denver 2010 Annual Meeting SEG Denver 2010 Annual Meeting 2547–2551.

Davydenko, A.Y., Grayver, A. V., 2014. Principal component analysis for filtering and leveling of geophysical data. J. Appl. Geophys. 109, 266–280. https://doi.org/10.1016/j.jappgeo.2014.08.006

Dawson, M., Kalkreuth, W., 1994. Coal rank and coalbed methane potential of Cretaceous/Tertiary coals in the Canadian Rocky Mountain foothills and adjacent foreland: 1. Hinton and Grande Cache areas, Alberta. Bull. Can. Pet. Geol. 42, 544–561.

Donato, I.D., Lazzara, G., 2012. Porosity determination with helium pycnometry as a method to characterize waterlogged woods and the efficacy of the conservation

treatments. Archaeometry 54, 906–915. https://doi.org/10.1111/j.1475-4754.2011.00657.x

Eastwood, J., 1993. Temperature-dependent propagation of P- and S-waves in Cold Lake oil sands: Comparison of theory and experiment. Geophysics 58, 863–872.

Eberhart-Phillips, D., Han, D.-H., Zoback, M.D., 1989. Empirical relationships among seismic velocity, effective pressure, porosity, and clay content in sandstone. Geophysics 54, 82–89.

Edmunds, N., Barret, K., Solanki, S., Cimolai, M., Wong, A., 2009. Prospects for Commercial Bitumen Recovery from the Grosmont Carbonate, Alberta. J. Can. Pet. Technol. 48, 26–32.

ExxonMobil, 2016. The Outlook for Energy: A View to 2040. https://doi.org/10.1080/01998595.2012.10491656

Farmer, S.A., 1971. An Investigation into the Results of Principal Component Analysis of Data Derived from Random Numbers. J. R. Stat. Soc. 20, 63–72.

Gegenhuber, N., Pupos, J., 2015. Rock physics template from laboratory data for carbonates. J. Appl. Geophys. 114, 12–18. https://doi.org/10.1016/j.jappgeo.2015.01.005

Ghanbarian, B., Hunt, A.G., Ewing, R.P., Sahimi, M., 2013. Tortuosity in Porous Media: A Critical Review. Soil Sci. Soc. Am. J. 77, 1461. https://doi.org/10.2136/sssaj2012.0435

Giesche, H., 2006. Mercury porosimetry: A general (practical) overview. Part. Part. Syst. Charact. 23, 9–19. https://doi.org/10.1002/ppsc.200601009

Gunst, R.F., 1983. Regression Analysis With Multicollinear Predictor Variables: Definition, Detection, And Effects, Communications in Statistics - Theory and Methods. https://doi.org/10.1080/03610928308828603

Guo, H., Marfurt, K.J., Liu, J., 2009. Principal component spectral analysis. Geophysics 74, P35–P43.

Guo, J., Han, X., 2016. Journal of Petroleum Science and Engineering Rock physics modelling of acoustic velocities for heavy oil sand. J. Pet. Sci. Eng. 145, 436–443. https://doi.org/10.1016/j.petrol.2016.05.028

Gurevich, B., Osypov, K., Ciz, R., Makarynska, D., 2008. Modeling elastic wave velocities and attenuation in rocks saturated with heavy oil. Geophysics 73, E115–E122.

Han, D.-H., Liu, J., Batzle, M., 2008. Seismic properties of heavy oils - measured data. Lead. Edge 27, 1108–1115.

Hashin, Z., Shtrikman, S., 1963. A variational approach to the theory of the elastic behaviour of multiphase materials. J. Mech. Phys. Solids 11, 127–140. https://doi.org/10.1016/0022-5096(63)90060-7

Higley, D.K., Lewan, M.D., Roberts, L.N.R., Henry, M., 2009. Timing and petroleum sources for the Lower Cretaceous Mannville Group oil sands of northern Alberta based on 4-D modeling. Am. Assoc. Pet. Geol. Bull. 93, 203–230. https://doi.org/10.1306/09150808060

Hill, R., 1952. The Elastic Behaviour of a Crystalline Aggregate. Proc. Phys. Soc. Sect. A 65, 349–354. https://doi.org/10.1088/0370-1298/65/5/307

Hitchon, B., Filby, R.H., 1984. Use of trace elements for classification of crude oils into families-example from Alberta, Canada. Am. Assoc. Pet. Geol. Bull. 68, 838–849. https://doi.org/10.1306/AD461435-16F7-11D7-8645000102C1865D

Hoffmann, C.R., Strausz, O.P., 1986. Bitumen Accumulation in Grosmont Platform Complex, Upper Devonian, Alberta, Canada. Am. Assoc. Pet. Geol. Bull. 70, 1113–1128.

Huebscher, H., Machel, H.G., 1997. Paleokarst in the Grosmont Formation, northeastern

Alberta, Canada, in: CSPG-SEPM Joint Convention Core Conference. pp. 129–152.

Ikelle, L.T., Amundsen, L., 2005. Introduction to Petroleum Seismology. Society of Exploration Geophysicists. https://doi.org/10.1190/1.9781560801702

Islam, M.S., 2018. Temperature Dependence Piezoelectric and Dielectric Properties of LiNbO3, PMN-PT and PZT-5A Materials.

Jiang, Q., Yuan, J., Russel-Houston, J., Thornton, B., Squires, A., 2010. Evaluation of Recovery Technologies for the Grosmont Carbonate Reservoirs. J. Can. Pet. Technol. 49, 56–64. https://doi.org/10.2118/137779-PA

Johnson, D.L., Plona, T.J., 1982. Acoustic slow waves and the consolidation transition. J. Acoust. Soc. Am. 72, 556–565. https://doi.org/10.1121/1.388036

Johnston, M., 2010. Temperature and frequency dependence of viscoelasticity in bitumen : lab measurements on heavy oil and bitumen. Lambert academic.

Jolliffe, I.T., 2002. Principal Component Analysis, Inflammatory Bowel Diseases. https://doi.org/10.1002/ibd.21544

Jones, G.D., Smart, P.L., Whitaker, F.F., Rostron, B.J., Machel, H.G., 2003. Numerical modeling of reflux dolomitization in the Grosmont platform complex (Upper Devonian), Western Canada sedimentary basin. Am. Assoc. Pet. Geol. Bull. 87, 1273–1298. https://doi.org/10.1306/03260302007

Kato, A., Onozuka, S., Nakayama, T., 2008. Elastic property changes in a bitumen reservoir during steam injection. Lead. Edge 27, 1124–1131.

Lakes, R., 2009. Viscoelastic Materials, Cambridge University Press. Cambridge University Press.

Lamb, H., 1945. Hydrodynamics. Dover publications.

Lavina, B., Dera, P., Downs, R.T., 2014. Modern X-ray Diffraction Methods in Mineralogy and Geosciences. Rev. Mineral. Geochemistry 78, 1–31. https://doi.org/10.2138/rmg.2014.78.1

Law, J., 1955. Geology of Northwestern Alberta and Adjacent Areas. Bull. Am. Assoc. Pet. Geol. 39, 1927–1975.

Lay, T., Wallace, T.C., 1995. Modern global seismology. Academic Press.

Lithium Niobate - Physical Properties [WWW Document], 2018. . Bost. Piezo-Optics Inc. URL https://www.bostonpiezooptics.com/lithium-niobate (accessed 4.22.18).

Luo, P., Machel, H.G., 1995. Pore Size and Pore Throat Types in a Heterogeneous Dolostone Reservoir, Devonian Grosmont Formation, Western Canada Sedimentary Basin. Am. Assoc. Pet. Geol. Bull. 79, 1698–1720.

Luo, P., Machel, H.G., Shaw, J., 1994. Petrophysical properties of matrix blocks of a heterogeneous dolostone reservoir - the Upper Devonian Grosmont Formation , Alberta , Canada. Bull. Can. Pet. Geol. 42, 465–481.

Machel, H.G., Borrero, M.L., Dembicki, E., Huebscher, H., Ping, L., Zhao, Y., 2012. The Grosmont : the world's largest unconventional oil reservoir hosted in carbonate rocks. Geol. Soc. London, Spec. Publ. 370, 49–81.

Makarynska, D., Gurevich, B., Behura, J., Batzle, M., 2010. Fluid substitution in rocks saturated with viscoelastic fluids. Geophysics 75, E115–E122.

Martinez, F.J., Batzle, M.L., Revil, A., 2012. Influence of temperature on seismic velocities and complex conductivity of heavy oil-bearing sands. Geophysics 77, WA19-WA34. https://doi.org/10.1190/geo2011-0433.1

Martínez, J.M., Schmitt, D.R., 2013. Anisotropic elastic moduli of carbonates and evaporites from the Weyburn-Midale reservoir and seal rocks. Geophys. Prospect. 61, 363–379.

https://doi.org/10.1111/1365-2478.12032

Mavko, G., Mukerji, T., Dvorkin, J., 2009. The Rock Physics Handbook. Cambridge University Press, Cambridge. https://doi.org/10.1017/CBO9780511626753

McDougall, J., Isaacs, E., Alvarez, J.M., 2008. Alberta Carbonates - the Third Trillion. 19th World Pet. Congr. Spain 2008, Forum 06 Carbonate Reserv. 1–12.

Mikhaltsevitch, V., Lebedev, M., Gurevich, B., 2016. Laboratory measurements of the effect of fluid saturation on elastic properties of carbonates at seismic frequencies. Geophys. Prospect. 64, 799–809. https://doi.org/10.1111/1365-2478.12404

Mohebati, M.H., Yang, D., MacDonald, J., 2014. Thermal recovery of bitumen from the grosmont carbonate formation - Part 1: The Saleski Pilot. J. Can. Pet. Technol. 53, 200–211. https://doi.org/10.2118/171561-PA

Montgomery, D.C., Peck, E.A., Vining, G.G., 2001. Introduction to linear regression analysis. Wiley.

Mutual, E., Cho, D., Innanen, K., 2017. Rock physics and time-lapse seismic analysis of thermal heavy oil production. Geoconvention 2017 1–4.

Nasr, T.N., Ayodele, O.R., 2005. Thermal Techniques for the Recovery of Heavy Oil and Bitumen, in: SPE International Improved Oil Recovery Conference in Asia Pacific. pp. 1–15. https://doi.org/10.2118/97488-ms

Njiekak, G., Schmitt, D.R., Kofman, R.S., 2018. Pore systems in carbonate formations, Weyburn field, Saskatchewan, Canada: Micro-tomography, helium porosimetry and mercury intrusion porosimetry characterization. J. Pet. Sci. Eng. 171, 1496–1513. https://doi.org/10.1016/J.PETROL.2018.08.029

Njiekak, G., Schmitt, D.R., Yam, H., Kofman, R.S., 2013. CO2 rock physics as part of the Weyburn-Midale geological storage project. Int. J. Greenh. Gas Control 16, S118–S133.

https://doi.org/10.1016/J.IJGGC.2013.02.007

Nur, A., Tosaya, C., Vo-Thanh, D., 1984. Seismic monitoring of thermal enhanced oil recovery processes, in: SEG Technical Program Expanded Abstracts 1984. pp. 337–340.

Oldenziel, T., 2003. Time-lapse seismic within reservoir engineering.

Ong, O.N., Schmitt, D.R., Rabbani, A., Kofman, R.S., 2018. Wave speed measurements of bitumen-saturated carbonates under thermal recovery conditions – Empirical relations and multi-variate analysis. Submitt. Geophys. Prospect.

Physical and Piezoelectric Properties of APC Materials [WWW Document], 2016. . APC Int. Ltd. URL https://www.americanpiezo.com/apc-materials/physical-piezoelectric-properties.html (accessed 4.22.18).

Piezoelectricity [WWW Document], 2016. . APC Int. Ltd. URL https://www.americanpiezo.com/knowledge-center/piezo-theory/piezoelectricity.html (accessed 4.16.18).

Putnam, P., Russel-Houston, J., Christensen, S., 2016. Comparison of McMurray Formation (Lower Cretaceous) and Grosmont Formation (Upper Devonian) bitumen reservoirs with some speculations, from a geological perspective, on the future of Canadian thermal recovery. Bull. Can. Pet. Geol. 64, 324–353. https://doi.org/10.2113/gscpgbull.64.2.324

Rabbani, A., Ong, O.N., Chen, X., Schmitt, D.R., Nycz, J., Gray, K., 2016. Rock Physics Laboratory Experiments on Bitumen Saturated Carbonates from the Grosmont Formation, Alberta, in: SEG Technical Program Expanded Abstracts 2016. pp. 3464–3467. https://doi.org/10.1103/PhysRevB.80.115331

Rabbani, A., Schmitt, D.R., 2018. Ultrasonic shear wave reflectometry applied to the

determination of the shear moduli and viscosity of a viscoelastic bitumen. Submitt. Fuel 40 pp.

Rabbani, A., Schmitt, D.R., Nycz, J., Gray, K., 2017. Pressure and temperature dependence of acoustic wave speeds in bitumen-saturated carbonates: Implications for seismic monitoring of the Grosmont Formation. Geophysics 82, MR133-MR151. https://doi.org/10.1190/geo2016-0667.1

Rabbani, A., Schmitt, D.R., Nycz, J., Gray, K., 2015. Velocity Measurements of Pore Fluids at Pressure and Temperature : Application to bitumen, in: GeoConvention 2015. pp. 1–5.

Rafavich, F., Kendall, C.H.S.C., Todd, T.P., 1984. The relationship between acoustic properties and the petrographic character of carbonate rocks. Geophysics. https://doi.org/10.1190/1.1441570

Reuss, A., 1929. Berechnung der Fließgrenze von Mischkristallen auf Grund der Plastizitätsbedingung für Einkristalle . ZAMM - Zeitschrift für Angew. Math. und Mech. 9, 49–58. https://doi.org/10.1002/zamm.19290090104

Roden, R., Smith, T., Sacrey, D., 2015. Geologic pattern recognition from seismic attributes: Principal component analysis and self-organizing maps. Interpretation 3, SAE59-SAE83. https://doi.org/10.1190/INT-2015-0037.1

Russel-Houston, J., Gray, K., 2014a. Paleokarst in the Grosmont Formation and reservoir implications, Saleski, Alberta, Canada. Interpretation 2, SF29-SF50. https://doi.org/10.1190/INT-2013-0187.1

Russel-Houston, J., Gray, K., 2014b. Paleokarst in the Grosmont Formation and reservoir implications, Saleski, Alberta, Canada. Interpretation 2, SF29-SF50.

Saxena, N., Mavko, G., 2014. Exact equations for fluid and solid substitution. Geophysics

79, L21–L32. https://doi.org/10.1190/geo2013-0187.1

Schmitt, D.R., 1999. Seismic attributes for monitoring of a shallow heated heavy oil reservoir: A case study. Geophysics 64, 368–377. https://doi.org/10.1190/1.1444541

Shabelansky, A.H., Malcolm, A., Fehler, M., 2015. Monitoring viscosity changes from time-lapse seismic attenuation : case study from a heavy oil reservoir. Geophys. Prospect. 1–16. https://doi.org/10.1111/1365-2478.12229

Shin, H., Polikar, M., 2005. Optimizing the SAGD Process in Three Major Canadian Oil-Sands Areas. 2005 SPE Annu. Tech. Conf. Exhib. 1. https://doi.org/10.2118/95754-ms

Smith, T.M., Sondergeld, C.H., Rai, C.S., 2003. Gassmann fluid substitutions: A tutorial. Geophysics 68, 430. https://doi.org/10.1190/1.1567211

Stoakes, F.A., Creaney, S., 1984. Sedimentology of a carbonate source rock: the Duvernay Formation of Central Alberta. Can. Soc. Pet. Geol. Core Conf. 132–143.

Thomsen, L., 1986. Weak elastic anisotropy. Geophysics 51, 1954. https://doi.org/10.1190/1.1442051

Tosaya, C., Nur, A., 1982. Effects of diagenesis and clays on compressional velocities in rocks. Geophys. Res. Lett. 9, 5–8. https://doi.org/10.1029/GL009i001p00005

van Dalen, K.N., 2013. Multi-Component Acoustic Characterization of Porous Media. https://doi.org/10.1007/978-3-642-34845-7

Voigt, W., 1907. Bestimmung der Elastizitätskonstanten von Eisenglanz. Ann. Phys. 327, 129–140. https://doi.org/10.1002/andp.19063270108

Wang, Z., 1997. 3. Seismic Properties of Carbonate Rocks, in: Carbonate Seismology. Society of Exploration Geophysicists, pp. 29–52. https://doi.org/10.1190/1.9781560802099.ch3

Wang, Z., Batzle, M., Nur, A., 1990. Effect of different pore fluids on seismic velocities in rocks. Can. J. Explor. Geophys. 26, 104–112. https://doi.org/10.1190/1.1892405

Wang, Z., Nur, A., 1990. Wave Velocities in Hydrocarbon-Saturated Rocks - Experimental Results. Geophysics 55, 723–733. https://doi.org/10.1190/1.1442884

Wang, Z., Nur, A., 1988. Effect of temperature on wave velocities in sands and sandstones with heavy hydrocarbons. SPE Reserv. Eng. 3, 154–168. https://doi.org/10.2118/15646-PA

Wang, Z., Schmitt, D.R., Zhou, W., Wang, R., Zang, Y., Zeng, Y., 2018. The stress dependence of velocities and its influencing factors for carbonate rocks in Arab formation, Saudi Arabia. Revis. J. Pet. Sci. Eng. https://doi.org/10.1016/J.MARPETGEO.2009.01.017

Wang, Z., Wang, R., Schmitt, D.R., 2015. The Elastic Moduli and Velocities of Artificial Carbonate rocks with Known Pore Structure at Different Saturation Conditions, in: Geoconvention 2015: New Horizons. pp. 1–5.

Wardlaw, N.C., McKellar, M., 1981. Mercury porosimetry and the interpretation of pore geometry in sedimentary rocks and artificial models. Powder Technol. 29, 127–143. https://doi.org/10.1016/0032-5910(81)85011-5

Webb, P., 2001. An Introduction To The Physical Characterization of Materials by Mercury Intrusion Porosimetry with Emphasis On Reduction And Presentation of Experimental Data. https://doi.org/10.1177/004057368303900411

Xie, J., Chen, W., Zhang, D., Zu, S., Chen, Y., 2017. Application of principal component analysis in weighted stacking of seismic data. IEEE Geosci. Remote Sens. Lett. 14, 1213–1217. https://doi.org/10.1109/LGRS.2017.2703611

Yam, H., 2011. CO2 rock physics: a laboratory study. Thesis.

https://doi.org/10.1016/S0022-3913(12)00047-9

Yang, D., Mohebati, M.H., Brand, S., Bennett, C., 2014. Thermal Recovery of Bitumen from the Grosmont Carbonate Formation - Part 2: Pilot Interpretation and Development Strategy. J. Can. Pet. Technol. 53, 212–223. https://doi.org/10.2118/171561-PA

Yuan, H., Han, D.-H., Zhang, W., 2016. Heavy oil sands measurement and rock-physics modeling. Geophysics 81, D57–D70. https://doi.org/10.1190/geo2014-0573.1

Yuan, H., Han, D.-H., Zhao, L., Huang, Q., Zhang, W., 2018. Rock-physics characterization of bitumen carbonates: A case study. Geophysics 83, B119–B132. https://doi.org/10.1190/geo2017-0319.1

Yuan, H., Han, D., 2013. Pressure and Temperature Effect on Heavy Oil Sands Properties, in: SEG Technical Program Expanded Abstracts 2013. pp. 2984–2988.

Yuan, H., Han, D., Li, H., Zhang, W., 2017a. A comparison of bitumen sands and bitumen carbonates: Measured data. Geophysics 82, MR39-MR50. https://doi.org/10.1190/geo2015-0657.1

Yuan, H., Han, D., Zhang, W., 2017b. Case History Seismic characterization of heavy oil reservoir during thermal production : A case study. Geophysics 82, B13–B27. https://doi.org/10.1190/geo2016-0155.1

Yuan, J.-Y., Jiang, Q., Russel-Houston, J., Thornton, B., Putnam, P., Putman, P.E., 2010. Evolving Recovery Technologies Directed Towards Commercial Development of the Grosmont Carbonate Reservoirs. Can. Unconv. Resour. Int. Pet. Conf. 1–21. https://doi.org/http://dx.doi.org/10.2118/137941-MS

Zhang, W., Youn, S., Doan, Q., 2007. Understanding Reservoir Architectures and Steam-Chamber Growth at Christina Lake, Alberta, by Using 4D Seismic and Crosswell Seismic Imaging. SPE Reserv. Eval. Eng. 10, 1–3. https://doi.org/10.2118/97808-PA

Zhao, Y., Machel, H.G., 2012. Viscosity and other rheological properties of bitumen from the Upper Devonian Grosmont reservoir, Alberta, Canada. Am. Assoc. Pet. Geol. Bull. 96, 133–153. https://doi.org/10.1306/04261110180

Zimmerman, R.W., 1991. Chapter 6. Undrained Compression, in: Developments in Petroleum Science. pp. 57–65.

Zimmerman, R.W., Somerton, W.H., King, M.S., 1986. Compressibility of Porous Rocks. J. Geophys. Res. 91, 12,765-12,777. https://doi.org/10.1029/JB091iB12p12765

Appendix

Sample dimensions

	Natural saturation					
	SA1	S3	S6	S8	S15	S17
Diameter (mm)	37.3	38.8	35.7	35.6	35.6	35.7
Length (mm)	48.4	64.3	31.6	34.9	33.6	40.4
Mass (g)	136.8	186.9	83.4	89.2	87.7	93.0

	Dry frame					
	SA1	S3	S6	S8	S15	S17
Diameter (mm)	37.4	38.6	35.8	35.7	35.7	35.7
Length (mm)	30.1	36.1	31.7	34.9	33.8	40.2
Mass (g)	82.3	95.2	81.9	88.9	85.0	84.5

Velocity measurements

Sample name	Sample state	Confining pressure (MPa)	Pore Pressure (MPa)	Temp. (°C)	Up-cycle / Down-cycle	P-wave velocity (m/s)	S-wave velocity (m/s)
SA1	Natural saturation	8	0	10	Up-cycle	5376	3001
SA1	Natural saturation	10	0	10	Up-cycle	5388	3005
SA1	Natural saturation	12	0	10	Up-cycle	5394	3011
SA1	Natural saturation	14	0	10	Up-cycle	5400	3014
SA1	Natural saturation	16	0	10	Up-cycle	5406	3018
SA1	Natural saturation	19	0	10	Up-cycle	5412	3020

SA1	Natural saturation	22	0	10	Up-cycle	5412	3024
SA1	Natural saturation	25	0	10	Up-cycle	5418	3028
SA1	Natural saturation	28	0	10	Up-cycle	5424	3031
SA1	Natural saturation	32	0	10	Up-cycle	5430	3033
SA1	Natural saturation	36	0	10	Up-cycle	5436	3037
SA1	Natural saturation	40	0	10	Up-cycle	5442	3039
SA1	Natural saturation	36	0	10	Down-cycle	5436	3039
SA1	Natural saturation	32	0	10	Down-cycle	5436	3037
SA1	Natural saturation	28	0	10	Down-cycle	5430	3035
SA1	Natural saturation	25	0	10	Down-cycle	5424	3031
SA1	Natural saturation	22	0	10	Down-cycle	5424	3029
SA1	Natural saturation	19	0	10	Down-cycle	5418	3028
SA1	Natural saturation	16	0	10	Down-cycle	5418	3026
SA1	Natural saturation	14	0	10	Down-cycle	5412	3024
SA1	Natural saturation	12	0	10	Down-cycle	5412	3022
SA1	Natural saturation	10	0	10	Down-cycle	5406	3018
SA1	Natural saturation	8	0	10	Down-cycle	5400	3014
SA1	Natural saturation	8	0	23	Up-cycle	5352	3014
SA1	Natural saturation	10	0	23	Up-cycle	5352	3014
SA1	Natural saturation	12	0	23	Up-cycle	5352	3016
SA1	Natural saturation	14	0	23	Up-cycle	5358	3016
SA1	Natural saturation	16	0	23	Up-cycle	5358	3020
SA1	Natural saturation	19	0	23	Up-cycle	5364	3022
SA1	Natural saturation	22	0	23	Up-cycle	5364	3022
SA1	Natural saturation	25	0	23	Up-cycle	5364	3026
SA1	Natural saturation	28	0	23	Up-cycle	5364	3028
SA1	Natural saturation	32	0	23	Up-cycle	5370	3029
SA1	Natural saturation	36	0	23	Up-cycle	5370	3033
SA1	Natural saturation	40	0	23	Up-cycle	5376	3035
SA1	Natural saturation	36	0	23	Down-cycle	5370	3033
SA1	Natural saturation	32	0	23	Down-cycle	5370	3031
SA1	Natural saturation	28	0	23	Down-cycle	5370	3029
SA1	Natural saturation	25	0	23	Down-cycle	5370	3029
SA1	Natural saturation	22	0	23	Down-cycle	5364	3028
SA1	Natural saturation	19	0	23	Down-cycle	5358	3024
SA1	Natural saturation	16	0	23	Down-cycle	5352	3020
SA1	Natural saturation	14	0	23	Down-cycle	5352	3016
SA1	Natural saturation	12	0	23	Down-cycle	5346	3014
SA1	Natural saturation	10	0	23	Down-cycle	5346	3014
SA1	Natural saturation	8	0	23	Down-cycle	5340	3012
SA1	Natural saturation	8	0	50	Up-cycle	5242	2979

SA1	Natural saturation	10	0	50	Up-cycle	5242	2985
SA1	Natural saturation	12	0	50	Up-cycle	5242	2986
SA1	Natural saturation	14	0	50	Up-cycle	5247	2986
SA1	Natural saturation	16	0	50	Up-cycle	5253	2985
SA1	Natural saturation	19	0	50	Up-cycle	5259	2981
SA1	Natural saturation	22	0	50	Up-cycle	5264	2966
SA1	Natural saturation	25	0	50	Up-cycle	5276	2966
SA1	Natural saturation	28	0	50	Up-cycle	5282	2968
SA1	Natural saturation	32	0	50	Up-cycle	5282	2977
SA1	Natural saturation	36	0	50	Up-cycle	5287	2974
SA1	Natural saturation	40	0	50	Up-cycle	5293	2975
SA1	Natural saturation	36	0	50	Down-cycle	5287	2975
SA1	Natural saturation	32	0	50	Down-cycle	5276	2966
SA1	Natural saturation	28	0	50	Down-cycle	5259	2963
SA1	Natural saturation	25	0	50	Down-cycle	5242	2945
SA1	Natural saturation	22	0	50	Down-cycle	5236	2929
SA1	Natural saturation	19	0	50	Down-cycle	5225	2914
SA1	Natural saturation	16	0	50	Down-cycle	5213	2899
SA1	Natural saturation	14	0	50	Down-cycle	5202	2890
SA1	Natural saturation	12	0	50	Down-cycle	5191	2885
SA1	Natural saturation	10	0	50	Down-cycle	5185	2880
SA1	Natural saturation	8	0	50	Down-cycle	5174	2873
SA1	Natural saturation	8	0	75	Up-cycle	5191	2895
SA1	Natural saturation	10	0	75	Up-cycle	5197	2892
SA1	Natural saturation	12	0	75	Up-cycle	5197	2892
SA1	Natural saturation	14	0	75	Up-cycle	5202	2892
SA1	Natural saturation	16	0	75	Up-cycle	5208	2894
SA1	Natural saturation	19	0	75	Up-cycle	5208	2899
SA1	Natural saturation	22	0	75	Up-cycle	5219	2902
SA1	Natural saturation	25	0	75	Up-cycle	5225	2906
SA1	Natural saturation	28	0	75	Up-cycle	5236	2914
SA1	Natural saturation	32	0	75	Up-cycle	5236	2930
SA1	Natural saturation	36	0	75	Up-cycle	5242	2945
SA1	Natural saturation	40	0	75	Up-cycle	5253	2948
SA1	Natural saturation	36	0	75	Down-cycle	5247	2945
SA1	Natural saturation	32	0	75	Down-cycle	5242	2943
SA1	Natural saturation	28	0	75	Down-cycle	5236	2936
SA1	Natural saturation	25	0	75	Down-cycle	5230	2925
SA1	Natural saturation	22	0	75	Down-cycle	5219	2911
SA1	Natural saturation	19	0	75	Down-cycle	5208	2900
SA1	Natural saturation	16	0	75	Down-cycle	5197	2890

SA1	Natural saturation	14	0	75	Down-cycle	5197	2892
SA1	Natural saturation	12	0	75	Down-cycle	5185	2883
SA1	Natural saturation	10	0	75	Down-cycle	5174	2880
SA1	Natural saturation	8	0	75	Down-cycle	5163	2880
SA1	Natural saturation	8	0	100	Up-cycle	5120	NaN
SA1	Natural saturation	10	0	100	Up-cycle	5125	NaN
SA1	Natural saturation	12	0	100	Up-cycle	5125	NaN
SA1	Natural saturation	14	0	100	Up-cycle	5130	NaN
SA1	Natural saturation	16	0	100	Up-cycle	5147	NaN
SA1	Natural saturation	19	0	100	Up-cycle	5158	NaN
SA1	Natural saturation	22	0	100	Up-cycle	5169	NaN
SA1	Natural saturation	25	0	100	Up-cycle	5180	NaN
SA1	Natural saturation	28	0	100	Up-cycle	5180	NaN
SA1	Natural saturation	32	0	100	Up-cycle	5191	NaN
SA1	Natural saturation	36	0	100	Up-cycle	5208	NaN
SA1	Natural saturation	40	0	100	Up-cycle	5213	NaN
SA1	Natural saturation	36	0	100	Down-cycle	5208	NaN
SA1	Natural saturation	32	0	100	Down-cycle	5208	NaN
SA1	Natural saturation	28	0	100	Down-cycle	5197	NaN
SA1	Natural saturation	25	0	100	Down-cycle	5191	NaN
SA1	Natural saturation	22	0	100	Down-cycle	5185	NaN
SA1	Natural saturation	19	0	100	Down-cycle	5174	NaN
SA1	Natural saturation	16	0	100	Down-cycle	5163	NaN
SA1	Natural saturation	14	0	100	Down-cycle	5152	NaN
SA1	Natural saturation	12	0	100	Down-cycle	5141	NaN
SA1	Natural saturation	10	0	100	Down-cycle	5130	NaN
SA1	Natural saturation	8	0	100	Down-cycle	5120	NaN
SA1	Natural saturation	8	1	10	Up-cycle	5394	3014
SA1	Natural saturation	10	3	10	Up-cycle	5400	3018
SA1	Natural saturation	12	5	10	Up-cycle	5406	3018
SA1	Natural saturation	14	7	10	Up-cycle	5406	3022
SA1	Natural saturation	16	9	10	Up-cycle	5412	3022
SA1	Natural saturation	19	12	10	Up-cycle	5418	3024
SA1	Natural saturation	22	15	10	Up-cycle	5418	3028
SA1	Natural saturation	25	18	10	Up-cycle	5424	3029
SA1	Natural saturation	28	21	10	Up-cycle	5424	3033
SA1	Natural saturation	32	25	10	Up-cycle	5430	3035
SA1	Natural saturation	36	29	10	Up-cycle	5442	3037
SA1	Natural saturation	40	33	10	Up-cycle	5448	3037
SA1	Natural saturation	36	29	10	Down-cycle	5442	3039
SA1	Natural saturation	32	25	10	Down-cycle	5436	3035

SA1	Natural saturation	28	21	10	Down-cycle	5430	3033
SA1	Natural saturation	25	18	10	Down-cycle	5430	3029
SA1	Natural saturation	22	15	10	Down-cycle	5424	3028
SA1	Natural saturation	19	12	10	Down-cycle	5418	3026
SA1	Natural saturation	16	9	10	Down-cycle	5418	3024
SA1	Natural saturation	14	7	10	Down-cycle	5418	3022
SA1	Natural saturation	12	5	10	Down-cycle	5412	3018
SA1	Natural saturation	10	3	10	Down-cycle	5406	3016
SA1	Natural saturation	8	1	10	Down-cycle	5400	3011
SA1	Natural saturation	8	1	23	Up-cycle	5358	2994
SA1	Natural saturation	10	3	23	Up-cycle	5358	2994
SA1	Natural saturation	12	5	23	Up-cycle	5358	2996
SA1	Natural saturation	14	7	23	Up-cycle	5364	2994
SA1	Natural saturation	16	9	23	Up-cycle	5370	2996
SA1	Natural saturation	19	12	23	Up-cycle	5376	2999
SA1	Natural saturation	22	15	23	Up-cycle	5376	3001
SA1	Natural saturation	25	18	23	Up-cycle	5382	3003
SA1	Natural saturation	28	21	23	Up-cycle	5388	3007
SA1	Natural saturation	32	25	23	Up-cycle	5394	3009
SA1	Natural saturation	36	29	23	Up-cycle	5394	3014
SA1	Natural saturation	40	33	23	Up-cycle	5400	3016
SA1	Natural saturation	36	29	23	Down-cycle	5394	3016
SA1	Natural saturation	32	25	23	Down-cycle	5388	3012
SA1	Natural saturation	28	21	23	Down-cycle	5388	3009
SA1	Natural saturation	25	18	23	Down-cycle	5388	3009
SA1	Natural saturation	22	15	23	Down-cycle	5382	3007
SA1	Natural saturation	19	12	23	Down-cycle	5376	3003
SA1	Natural saturation	16	9	23	Down-cycle	5370	2999
SA1	Natural saturation	14	7	23	Down-cycle	5364	2999
SA1	Natural saturation	12	5	23	Down-cycle	5358	2999
SA1	Natural saturation	10	3	23	Down-cycle	5358	2996
SA1	Natural saturation	8	1	23	Down-cycle	5352	2994
SA1	Natural saturation	8	1	50	Up-cycle	5259	2983
SA1	Natural saturation	10	3	50	Up-cycle	5270	2972
SA1	Natural saturation	12	5	50	Up-cycle	5270	2961
SA1	Natural saturation	14	7	50	Up-cycle	5276	2957
SA1	Natural saturation	16	9	50	Up-cycle	5287	2955
SA1	Natural saturation	19	12	50	Up-cycle	5287	2957
SA1	Natural saturation	22	15	50	Up-cycle	5299	2959
SA1	Natural saturation	25	18	50	Up-cycle	5311	2964
SA1	Natural saturation	28	21	50	Up-cycle	5316	2966

SA1	Natural saturation	32	25	50	Up-cycle	5316	2972
SA1	Natural saturation	36	29	50	Up-cycle	5328	2977
SA1	Natural saturation	40	33	50	Up-cycle	5334	2981
SA1	Natural saturation	36	29	50	Down-cycle	5328	2977
SA1	Natural saturation	32	25	50	Down-cycle	5322	2974
SA1	Natural saturation	28	21	50	Down-cycle	5316	2972
SA1	Natural saturation	25	18	50	Down-cycle	5311	2968
SA1	Natural saturation	22	15	50	Down-cycle	5305	2964
SA1	Natural saturation	19	12	50	Down-cycle	5293	2963
SA1	Natural saturation	16	9	50	Down-cycle	5287	2961
SA1	Natural saturation	14	7	50	Down-cycle	5282	2968
SA1	Natural saturation	12	5	50	Down-cycle	5270	2979
SA1	Natural saturation	10	3	50	Down-cycle	5259	2979
SA1	Natural saturation	8	1	50	Down-cycle	5247	2974
SA1	Natural saturation	8	1	75	Up-cycle	5180	2875
SA1	Natural saturation	10	3	75	Up-cycle	5185	2870
SA1	Natural saturation	12	5	75	Up-cycle	5191	2878
SA1	Natural saturation	14	7	75	Up-cycle	5197	2881
SA1	Natural saturation	16	9	75	Up-cycle	5208	2883
SA1	Natural saturation	19	12	75	Up-cycle	5213	2885
SA1	Natural saturation	22	15	75	Up-cycle	5225	2890
SA1	Natural saturation	25	18	75	Up-cycle	5230	2895
SA1	Natural saturation	28	21	75	Up-cycle	5242	2906
SA1	Natural saturation	32	25	75	Up-cycle	5247	2909
SA1	Natural saturation	36	29	75	Up-cycle	5259	2914
SA1	Natural saturation	40	33	75	Up-cycle	5270	2929
SA1	Natural saturation	36	29	75	Down-cycle	5264	2930
SA1	Natural saturation	32	25	75	Down-cycle	5259	2923
SA1	Natural saturation	28	21	75	Down-cycle	5247	2906
SA1	Natural saturation	25	18	75	Down-cycle	5247	2900
SA1	Natural saturation	22	15	75	Down-cycle	5236	2897
SA1	Natural saturation	19	12	75	Down-cycle	5225	2892
SA1	Natural saturation	16	9	75	Down-cycle	5208	2883
SA1	Natural saturation	14	7	75	Down-cycle	5202	2876
SA1	Natural saturation	12	5	75	Down-cycle	5191	2871
SA1	Natural saturation	10	3	75	Down-cycle	5185	2866
SA1	Natural saturation	8	1	75	Down-cycle	5169	2863
SA1	Natural saturation	8	1	100	Up-cycle	5136	NaN
SA1	Natural saturation	10	3	100	Up-cycle	5141	NaN
SA1	Natural saturation	12	5	100	Up-cycle	5141	NaN
SA1	Natural saturation	14	7	100	Up-cycle	5158	NaN

SA1	Natural saturation	16	9	100	Up-cycle	5169	NaN
SA1	Natural saturation	19	12	100	Up-cycle	5208	NaN
SA1	Natural saturation	22	15	100	Up-cycle	5225	NaN
SA1	Natural saturation	25	18	100	Up-cycle	5230	NaN
SA1	Natural saturation	28	21	100	Up-cycle	5225	NaN
SA1	Natural saturation	32	25	100	Up-cycle	5236	NaN
SA1	Natural saturation	36	29	100	Up-cycle	5247	NaN
SA1	Natural saturation	40	33	100	Up-cycle	5247	NaN
SA1	Natural saturation	36	29	100	Down-cycle	5236	NaN
SA1	Natural saturation	32	25	100	Down-cycle	5236	NaN
SA1	Natural saturation	28	21	100	Down-cycle	5225	NaN
SA1	Natural saturation	25	18	100	Down-cycle	5219	NaN
SA1	Natural saturation	22	15	100	Down-cycle	5219	NaN
SA1	Natural saturation	19	12	100	Down-cycle	5213	NaN
SA1	Natural saturation	16	9	100	Down-cycle	5208	NaN
SA1	Natural saturation	14	7	100	Down-cycle	5202	NaN
SA1	Natural saturation	12	5	100	Down-cycle	5202	NaN
SA1	Natural saturation	10	3	100	Down-cycle	5197	NaN
SA1	Natural saturation	8	1	100	Down-cycle	5191	NaN
SA1	Dry frame	8	0	10	Up-cycle	5425	3051
SA1	Dry frame	10	0	10	Up-cycle	5445	3054
SA1	Dry frame	12	0	10	Up-cycle	5465	3063
SA1	Dry frame	14	0	10	Up-cycle	5485	3066
SA1	Dry frame	16	0	10	Up-cycle	5475	3072
SA1	Dry frame	19	0	10	Up-cycle	5495	3076
SA1	Dry frame	22	0	10	Up-cycle	5505	3079
SA1	Dry frame	25	0	10	Up-cycle	5515	3088
SA1	Dry frame	28	0	10	Up-cycle	5515	3091
SA1	Dry frame	32	0	10	Up-cycle	5535	3095
SA1	Dry frame	36	0	10	Up-cycle	5545	3101
SA1	Dry frame	40	0	10	Up-cycle	5555	3104
SA1	Dry frame	36	0	10	Down-cycle	5555	3104
SA1	Dry frame	32	0	10	Down-cycle	5545	3098
SA1	Dry frame	28	0	10	Down-cycle	5535	3098
SA1	Dry frame	25	0	10	Down-cycle	5525	3095
SA1	Dry frame	22	0	10	Down-cycle	5515	3088
SA1	Dry frame	19	0	10	Down-cycle	5505	3082
SA1	Dry frame	16	0	10	Down-cycle	5495	3079
SA1	Dry frame	14	0	10	Down-cycle	5505	3072
SA1	Dry frame	12	0	10	Down-cycle	5485	3069
SA1	Dry frame	10	0	10	Down-cycle	5455	3057

SA1	Dry frame	8	0	10	Down-cycle	5425	3048
SA1	Dry frame	8	0	23	Up-cycle	5396	3044
SA1	Dry frame	10	0	23	Up-cycle	5406	3054
SA1	Dry frame	12	0	23	Up-cycle	5425	3063
SA1	Dry frame	14	0	23	Up-cycle	5445	3076
SA1	Dry frame	16	0	23	Up-cycle	5455	3079
SA1	Dry frame	19	0	23	Up-cycle	5455	3085
SA1	Dry frame	22	0	23	Up-cycle	5465	3091
SA1	Dry frame	25	0	23	Up-cycle	5475	3098
SA1	Dry frame	28	0	23	Up-cycle	5485	3104
SA1	Dry frame	32	0	23	Up-cycle	5505	3111
SA1	Dry frame	36	0	23	Up-cycle	5525	3117
SA1	Dry frame	40	0	23	Up-cycle	5545	3120
SA1	Dry frame	36	0	23	Down-cycle	5545	3123
SA1	Dry frame	32	0	23	Down-cycle	5535	3120
SA1	Dry frame	28	0	23	Down-cycle	5515	3114
SA1	Dry frame	25	0	23	Down-cycle	5505	3114
SA1	Dry frame	22	0	23	Down-cycle	5495	3104
SA1	Dry frame	19	0	23	Down-cycle	5475	3095
SA1	Dry frame	16	0	23	Down-cycle	5475	3088
SA1	Dry frame	14	0	23	Down-cycle	5465	3085
SA1	Dry frame	12	0	23	Down-cycle	5445	3069
SA1	Dry frame	10	0	23	Down-cycle	5425	3060
SA1	Dry frame	8	0	23	Down-cycle	5406	3044
SA1	Dry frame	8	0	50	Up-cycle	5406	2987
SA1	Dry frame	10	0	50	Up-cycle	5415	2996
SA1	Dry frame	12	0	50	Up-cycle	5425	3008
SA1	Dry frame	14	0	50	Up-cycle	5435	3014
SA1	Dry frame	16	0	50	Up-cycle	5435	3023
SA1	Dry frame	19	0	50	Up-cycle	5435	3029
SA1	Dry frame	22	0	50	Up-cycle	5445	3038
SA1	Dry frame	25	0	50	Up-cycle	5465	3044
SA1	Dry frame	28	0	50	Up-cycle	5465	3051
SA1	Dry frame	32	0	50	Up-cycle	5495	3057
SA1	Dry frame	36	0	50	Up-cycle	5515	3069
SA1	Dry frame	40	0	50	Up-cycle	5515	3072
SA1	Dry frame	36	0	50	Down-cycle	5515	3072
SA1	Dry frame	32	0	50	Down-cycle	5505	3069
SA1	Dry frame	28	0	50	Down-cycle	5485	3060
SA1	Dry frame	25	0	50	Down-cycle	5475	3054
SA1	Dry frame	22	0	50	Down-cycle	5465	3048

SA1	Dry frame	19	0	50	Down-cycle	5445	3038
SA1	Dry frame	16	0	50	Down-cycle	5445	3032
SA1	Dry frame	14	0	50	Down-cycle	5445	3020
SA1	Dry frame	12	0	50	Down-cycle	5425	3014
SA1	Dry frame	10	0	50	Down-cycle	5415	3002
SA1	Dry frame	8	0	50	Down-cycle	5406	2981
SA1	Dry frame	8	0	75	Up-cycle	5396	2967
SA1	Dry frame	10	0	75	Up-cycle	5406	2975
SA1	Dry frame	12	0	75	Up-cycle	5415	2984
SA1	Dry frame	14	0	75	Up-cycle	5415	2990
SA1	Dry frame	16	0	75	Up-cycle	5415	2999
SA1	Dry frame	19	0	75	Up-cycle	5415	3005
SA1	Dry frame	22	0	75	Up-cycle	5435	3014
SA1	Dry frame	25	0	75	Up-cycle	5445	3023
SA1	Dry frame	28	0	75	Up-cycle	5465	3029
SA1	Dry frame	32	0	75	Up-cycle	5485	3035
SA1	Dry frame	36	0	75	Up-cycle	5495	3044
SA1	Dry frame	40	0	75	Up-cycle	5505	3054
SA1	Dry frame	36	0	75	Down-cycle	5505	3048
SA1	Dry frame	32	0	75	Down-cycle	5495	3041
SA1	Dry frame	28	0	75	Down-cycle	5475	3041
SA1	Dry frame	25	0	75	Down-cycle	5475	3035
SA1	Dry frame	22	0	75	Down-cycle	5445	3029
SA1	Dry frame	19	0	75	Down-cycle	5425	3020
SA1	Dry frame	16	0	75	Down-cycle	5425	3011
SA1	Dry frame	14	0	75	Down-cycle	5425	3002
SA1	Dry frame	12	0	75	Down-cycle	5415	2996
SA1	Dry frame	10	0	75	Down-cycle	5406	2981
SA1	Dry frame	8	0	75	Down-cycle	5386	2961
SA1	Dry frame	8	0	100	Up-cycle	5367	2940
SA1	Dry frame	10	0	100	Up-cycle	5367	2946
SA1	Dry frame	12	0	100	Up-cycle	5367	2952
SA1	Dry frame	14	0	100	Up-cycle	5377	2961
SA1	Dry frame	16	0	100	Up-cycle	5377	2967
SA1	Dry frame	19	0	100	Up-cycle	5377	2981
SA1	Dry frame	22	0	100	Up-cycle	5386	2990
SA1	Dry frame	25	0	100	Up-cycle	5396	2999
SA1	Dry frame	28	0	100	Up-cycle	5415	3005
SA1	Dry frame	32	0	100	Up-cycle	5425	3014
SA1	Dry frame	36	0	100	Up-cycle	5445	3026
SA1	Dry frame	40	0	100	Up-cycle	5455	3029

SA1	Dry frame	36	0	100	Down-cycle	5455	3026
SA1	Dry frame	32	0	100	Down-cycle	5435	3023
SA1	Dry frame	28	0	100	Down-cycle	5435	3017
SA1	Dry frame	25	0	100	Down-cycle	5406	3011
SA1	Dry frame	22	0	100	Down-cycle	5406	3008
SA1	Dry frame	19	0	100	Down-cycle	5396	3002
SA1	Dry frame	16	0	100	Down-cycle	5386	2987
SA1	Dry frame	14	0	100	Down-cycle	5386	2978
SA1	Dry frame	12	0	100	Down-cycle	5377	2969
SA1	Dry frame	10	0	100	Down-cycle	5367	2955
SA1	Dry frame	8	0	100	Down-cycle	5367	2940
SA1	Water saturation	8	1	10	Up-cycle	5545	2892
SA1	Water saturation	10	3	10	Up-cycle	5545	2887
SA1	Water saturation	12	5	10	Up-cycle	5545	2887
SA1	Water saturation	14	7	10	Up-cycle	5545	2884
SA1	Water saturation	16	9	10	Up-cycle	5535	2884
SA1	Water saturation	19	12	10	Up-cycle	5545	2881
SA1	Water saturation	22	15	10	Up-cycle	5545	2881
SA1	Water saturation	25	18	10	Up-cycle	5545	2890
SA1	Water saturation	28	21	10	Up-cycle	5555	2892
SA1	Water saturation	32	25	10	Up-cycle	5555	2873
SA1	Water saturation	36	29	10	Up-cycle	5545	2873
SA1	Water saturation	40	33	10	Up-cycle	5545	2870
SA1	Water saturation	36	29	10	Down-cycle	5535	2873
SA1	Water saturation	32	25	10	Down-cycle	5545	2873
SA1	Water saturation	28	21	10	Down-cycle	5545	2876
SA1	Water saturation	25	18	10	Down-cycle	5535	2876
SA1	Water saturation	22	15	10	Down-cycle	5545	2876
SA1	Water saturation	19	12	10	Down-cycle	5545	2881
SA1	Water saturation	16	9	10	Down-cycle	5535	2884
SA1	Water saturation	14	7	10	Down-cycle	5545	2884
SA1	Water saturation	12	5	10	Down-cycle	5545	2887
SA1	Water saturation	10	3	10	Down-cycle	5545	2884
SA1	Water saturation	8	1	10	Down-cycle	5545	2887
SA1	Water saturation	8	1	23	Up-cycle	5525	2876
SA1	Water saturation	10	3	23	Up-cycle	5525	2870
SA1	Water saturation	12	5	23	Up-cycle	5525	2868
SA1	Water saturation	14	7	23	Up-cycle	5525	2868
SA1	Water saturation	16	9	23	Up-cycle	5525	2865
SA1	Water saturation	19	12	23	Up-cycle	5525	2862
SA1	Water saturation	22	15	23	Up-cycle	5525	2862

SA1	Water saturation	25	18	23	Up-cycle	5535	2862
SA1	Water saturation	28	21	23	Up-cycle	5525	2865
SA1	Water saturation	32	25	23	Up-cycle	5535	2876
SA1	Water saturation	36	29	23	Up-cycle	5545	2884
SA1	Water saturation	40	33	23	Up-cycle	5545	2892
SA1	Water saturation	36	29	23	Down-cycle	5555	2887
SA1	Water saturation	32	25	23	Down-cycle	5545	2876
SA1	Water saturation	28	21	23	Down-cycle	5535	2865
SA1	Water saturation	25	18	23	Down-cycle	5535	2865
SA1	Water saturation	22	15	23	Down-cycle	5535	2865
SA1	Water saturation	19	12	23	Down-cycle	5525	2865
SA1	Water saturation	16	9	23	Down-cycle	5535	2868
SA1	Water saturation	14	7	23	Down-cycle	5535	2868
SA1	Water saturation	12	5	23	Down-cycle	5525	2868
SA1	Water saturation	10	3	23	Down-cycle	5525	2870
SA1	Water saturation	8	1	23	Down-cycle	5525	2873
SA1	Water saturation	8	1	50	Up-cycle	5475	2822
SA1	Water saturation	10	3	50	Up-cycle	5475	2822
SA1	Water saturation	12	5	50	Up-cycle	5485	2822
SA1	Water saturation	14	7	50	Up-cycle	5485	2819
SA1	Water saturation	16	9	50	Up-cycle	5485	2822
SA1	Water saturation	19	12	50	Up-cycle	5485	2819
SA1	Water saturation	22	15	50	Up-cycle	5495	2819
SA1	Water saturation	25	18	50	Up-cycle	5495	2819
SA1	Water saturation	28	21	50	Up-cycle	5485	2819
SA1	Water saturation	32	25	50	Up-cycle	5495	2822
SA1	Water saturation	36	29	50	Up-cycle	5495	2822
SA1	Water saturation	40	33	50	Up-cycle	5495	2819
SA1	Water saturation	36	29	50	Down-cycle	5495	2822
SA1	Water saturation	32	25	50	Down-cycle	5495	2822
SA1	Water saturation	28	21	50	Down-cycle	5485	2822
SA1	Water saturation	25	18	50	Down-cycle	5495	2825
SA1	Water saturation	22	15	50	Down-cycle	5495	2822
SA1	Water saturation	19	12	50	Down-cycle	5485	2822
SA1	Water saturation	16	9	50	Down-cycle	5495	2825
SA1	Water saturation	14	7	50	Down-cycle	5485	2825
SA1	Water saturation	12	5	50	Down-cycle	5485	2827
SA1	Water saturation	10	3	50	Down-cycle	5475	2827
SA1	Water saturation	8	1	50	Down-cycle	5475	2830
SA1	Water saturation	8	1	75	Up-cycle	5435	2817
SA1	Water saturation	10	3	75	Up-cycle	5435	2814

SA1	Water saturation	12	5	75	Up-cycle	5445	2814
SA1	Water saturation	14	7	75	Up-cycle	5445	2811
SA1	Water saturation	16	9	75	Up-cycle	5445	2811
SA1	Water saturation	19	12	75	Up-cycle	5445	2809
SA1	Water saturation	22	15	75	Up-cycle	5445	2809
SA1	Water saturation	25	18	75	Up-cycle	5455	2809
SA1	Water saturation	28	21	75	Up-cycle	5455	2811
SA1	Water saturation	32	25	75	Up-cycle	5455	2809
SA1	Water saturation	36	29	75	Up-cycle	5465	2809
SA1	Water saturation	40	33	75	Up-cycle	5455	2811
SA1	Water saturation	36	29	75	Down-cycle	5465	2809
SA1	Water saturation	32	25	75	Down-cycle	5455	2806
SA1	Water saturation	28	21	75	Down-cycle	5455	2809
SA1	Water saturation	25	18	75	Down-cycle	5455	2809
SA1	Water saturation	22	15	75	Down-cycle	5445	2811
SA1	Water saturation	19	12	75	Down-cycle	5445	2809
SA1	Water saturation	16	9	75	Down-cycle	5455	2811
SA1	Water saturation	14	7	75	Down-cycle	5445	2811
SA1	Water saturation	12	5	75	Down-cycle	5445	2811
SA1	Water saturation	10	3	75	Down-cycle	5435	2811
SA1	Water saturation	8	1	75	Down-cycle	5435	2811
SA1	Water saturation	8	1	100	Up-cycle	5386	2762
SA1	Water saturation	10	3	100	Up-cycle	5377	2757
SA1	Water saturation	12	5	100	Up-cycle	5377	2755
SA1	Water saturation	14	7	100	Up-cycle	5386	2755
SA1	Water saturation	16	9	100	Up-cycle	5386	2757
SA1	Water saturation	19	12	100	Up-cycle	5377	2760
SA1	Water saturation	22	15	100	Up-cycle	5386	2760
SA1	Water saturation	25	18	100	Up-cycle	5377	2760
SA1	Water saturation	28	21	100	Up-cycle	5386	2760
SA1	Water saturation	32	25	100	Up-cycle	5377	2760
SA1	Water saturation	36	29	100	Up-cycle	5386	2757
SA1	Water saturation	40	33	100	Up-cycle	5386	2760
SA1	Water saturation	36	29	100	Down-cycle	5386	2762
SA1	Water saturation	32	25	100	Down-cycle	5377	2762
SA1	Water saturation	28	21	100	Down-cycle	5386	2765
SA1	Water saturation	25	18	100	Down-cycle	5377	2765
SA1	Water saturation	22	15	100	Down-cycle	5386	2765
SA1	Water saturation	19	12	100	Down-cycle	5386	2765
SA1	Water saturation	16	9	100	Down-cycle	5386	2762
SA1	Water saturation	14	7	100	Down-cycle	5386	2762

SA1	Water saturation	12	5	100	Down-cycle	5377	2762
SA1	Water saturation	10	3	100	Down-cycle	5377	2760
SA1	Water saturation	8	1	100	Down-cycle	5386	2760
S3	Natural saturation	2	0	10	Up-cycle	4916	2813
S3	Natural saturation	3	0	10	Up-cycle	4924	2817
S3	Natural saturation	4	0	10	Up-cycle	4939	2820
S3	Natural saturation	5	0	10	Up-cycle	4939	2823
S3	Natural saturation	6	0	10	Up-cycle	4947	2825
S3	Natural saturation	7	0	10	Up-cycle	4951	2830
S3	Natural saturation	8	0	10	Up-cycle	4958	2832
S3	Natural saturation	9	0	10	Up-cycle	4962	2835
S3	Natural saturation	10	0	10	Up-cycle	4970	2838
S3	Natural saturation	12	0	10	Up-cycle	4970	2843
S3	Natural saturation	14	0	10	Up-cycle	4973	2845
S3	Natural saturation	16	0	10	Up-cycle	4977	2848
S3	Natural saturation	18	0	10	Up-cycle	4981	2849
S3	Natural saturation	20	0	10	Up-cycle	4985	2850
S3	Natural saturation	25	0	10	Up-cycle	4989	2854
S3	Natural saturation	30	0	10	Up-cycle	4993	2857
S3	Natural saturation	25	0	10	Down-cycle	4989	2856
S3	Natural saturation	20	0	10	Down-cycle	4985	2852
S3	Natural saturation	18	0	10	Down-cycle	4989	2853
S3	Natural saturation	16	0	10	Down-cycle	4985	2852
S3	Natural saturation	14	0	10	Down-cycle	4985	2850
S3	Natural saturation	12	0	10	Down-cycle	4977	2849
S3	Natural saturation	10	0	10	Down-cycle	4977	2847
S3	Natural saturation	8	0	10	Down-cycle	4970	2844
S3	Natural saturation	5	0	10	Down-cycle	4958	2837
S3	Natural saturation	2	0	10	Down-cycle	4935	2825
S3	Natural saturation	2	0	23	Up-cycle	4813	2785
S3	Natural saturation	3	0	23	Up-cycle	4824	2786
S3	Natural saturation	4	0	23	Up-cycle	4831	2786
S3	Natural saturation	5	0	23	Up-cycle	4835	2787
S3	Natural saturation	6	0	23	Up-cycle	4842	2787
S3	Natural saturation	7	0	23	Up-cycle	4850	2789
S3	Natural saturation	8	0	23	Up-cycle	4857	2789
S3	Natural saturation	9	0	23	Up-cycle	4861	2790
S3	Natural saturation	10	0	23	Up-cycle	4861	2791
S3	Natural saturation	12	0	23	Up-cycle	4864	2792
S3	Natural saturation	14	0	23	Up-cycle	4872	2792
S3	Natural saturation	16	0	23	Up-cycle	4875	2794

S3	Natural saturation	18	0	23	Up-cycle	4883	2795
S3	Natural saturation	20	0	23	Up-cycle	4887	2796
S3	Natural saturation	25	0	23	Up-cycle	4890	2797
S3	Natural saturation	30	0	23	Up-cycle	4894	2801
S3	Natural saturation	25	0	23	Down-cycle	4894	2800
S3	Natural saturation	20	0	23	Down-cycle	4887	2798
S3	Natural saturation	18	0	23	Down-cycle	4890	2798
S3	Natural saturation	16	0	23	Down-cycle	4887	2798
S3	Natural saturation	14	0	23	Down-cycle	4883	2797
S3	Natural saturation	12	0	23	Down-cycle	4883	2796
S3	Natural saturation	10	0	23	Down-cycle	4879	2795
S3	Natural saturation	8	0	23	Down-cycle	4875	2794
S3	Natural saturation	5	0	23	Down-cycle	4875	2794
S3	Natural saturation	2	0	23	Down-cycle	4872	2794
S3	Natural saturation	2	0	50	Up-cycle	4548	NaN
S3	Natural saturation	3	0	50	Up-cycle	4564	NaN
S3	Natural saturation	4	0	50	Up-cycle	4575	NaN
S3	Natural saturation	5	0	50	Up-cycle	4590	NaN
S3	Natural saturation	6	0	50	Up-cycle	4603	NaN
S3	Natural saturation	7	0	50	Up-cycle	4610	NaN
S3	Natural saturation	8	0	50	Up-cycle	4616	NaN
S3	Natural saturation	9	0	50	Up-cycle	4623	NaN
S3	Natural saturation	10	0	50	Up-cycle	4630	NaN
S3	Natural saturation	12	0	50	Up-cycle	4643	NaN
S3	Natural saturation	14	0	50	Up-cycle	4646	NaN
S3	Natural saturation	16	0	50	Up-cycle	4657	NaN
S3	Natural saturation	18	0	50	Up-cycle	4663	NaN
S3	Natural saturation	20	0	50	Up-cycle	4667	NaN
S3	Natural saturation	25	0	50	Up-cycle	4680	NaN
S3	Natural saturation	30	0	50	Up-cycle	4694	NaN
S3	Natural saturation	25	0	50	Down-cycle	4687	NaN
S3	Natural saturation	20	0	50	Down-cycle	4677	NaN
S3	Natural saturation	18	0	50	Down-cycle	4673	NaN
S3	Natural saturation	16	0	50	Down-cycle	4670	NaN
S3	Natural saturation	14	0	50	Down-cycle	4663	NaN
S3	Natural saturation	12	0	50	Down-cycle	4657	NaN
S3	Natural saturation	10	0	50	Down-cycle	4646	NaN
S3	Natural saturation	8	0	50	Down-cycle	4640	NaN
S3	Natural saturation	5	0	50	Down-cycle	4616	NaN
S3	Natural saturation	2	0	50	Down-cycle	4574	NaN
S3	Natural saturation	2	0	75	Up-cycle	4420	NaN

S3	Natural saturation	3	0	75	Up-cycle	4441	NaN
S3	Natural saturation	4	0	75	Up-cycle	4463	NaN
S3	Natural saturation	5	0	75	Up-cycle	4484	NaN
S3	Natural saturation	6	0	75	Up-cycle	4503	NaN
S3	Natural saturation	7	0	75	Up-cycle	4516	NaN
S3	Natural saturation	8	0	75	Up-cycle	4532	NaN
S3	Natural saturation	9	0	75	Up-cycle	4541	NaN
S3	Natural saturation	10	0	75	Up-cycle	4554	NaN
S3	Natural saturation	12	0	75	Up-cycle	4571	NaN
S3	Natural saturation	14	0	75	Up-cycle	4580	NaN
S3	Natural saturation	16	0	75	Up-cycle	4590	NaN
S3	Natural saturation	18	0	75	Up-cycle	4597	NaN
S3	Natural saturation	20	0	75	Up-cycle	4603	NaN
S3	Natural saturation	25	0	75	Up-cycle	4613	NaN
S3	Natural saturation	30	0	75	Up-cycle	4623	NaN
S3	Natural saturation	25	0	75	Down-cycle	4613	NaN
S3	Natural saturation	20	0	75	Down-cycle	4603	NaN
S3	Natural saturation	18	0	75	Down-cycle	4600	NaN
S3	Natural saturation	16	0	75	Down-cycle	4597	NaN
S3	Natural saturation	14	0	75	Down-cycle	4587	NaN
S3	Natural saturation	12	0	75	Down-cycle	4577	NaN
S3	Natural saturation	10	0	75	Down-cycle	4561	NaN
S3	Natural saturation	8	0	75	Down-cycle	4541	NaN
S3	Natural saturation	5	0	75	Down-cycle	4506	NaN
S3	Natural saturation	2	0	75	Down-cycle	4438	NaN
S3	Natural saturation	2	0	100	Up-cycle	NaN	NaN
S3	Natural saturation	3	0	100	Up-cycle	NaN	NaN
S3	Natural saturation	4	0	100	Up-cycle	NaN	NaN
S3	Natural saturation	5	0	100	Up-cycle	NaN	NaN
S3	Natural saturation	6	0	100	Up-cycle	4390	NaN
S3	Natural saturation	7	0	100	Up-cycle	NaN	NaN
S3	Natural saturation	8	0	100	Up-cycle	4408	NaN
S3	Natural saturation	9	0	100	Up-cycle	NaN	NaN
S3	Natural saturation	10	0	100	Up-cycle	4426	NaN
S3	Natural saturation	12	0	100	Up-cycle	4450	NaN
S3	Natural saturation	14	0	100	Up-cycle	4472	NaN
S3	Natural saturation	16	0	100	Up-cycle	4497	NaN
S3	Natural saturation	18	0	100	Up-cycle	4510	NaN
S3	Natural saturation	20	0	100	Up-cycle	4522	NaN
S3	Natural saturation	25	0	100	Up-cycle	4548	NaN
S3	Natural saturation	30	0	100	Up-cycle	4571	NaN

S3	Natural saturation	25	0	100	Down-cycle	4558	NaN
S3	Natural saturation	20	0	100	Down-cycle	4541	NaN
S3	Natural saturation	18	0	100	Down-cycle	4535	NaN
S3	Natural saturation	16	0	100	Down-cycle	4529	NaN
S3	Natural saturation	14	0	100	Down-cycle	4522	NaN
S3	Natural saturation	12	0	100	Down-cycle	4506	NaN
S3	Natural saturation	10	0	100	Down-cycle	4494	NaN
S3	Natural saturation	8	0	100	Down-cycle	4472	NaN
S3	Natural saturation	5	0	100	Down-cycle	NaN	NaN
S3	Natural saturation	2	0	100	Down-cycle	NaN	NaN
S3	Natural saturation	8	1	10	Up-cycle	4943	2856
S3	Natural saturation	10	3	10	Up-cycle	4954	2861
S3	Natural saturation	12	5	10	Up-cycle	4954	2861
S3	Natural saturation	14	7	10	Up-cycle	4958	2863
S3	Natural saturation	16	9	10	Up-cycle	4962	2866
S3	Natural saturation	19	12	10	Up-cycle	4970	2868
S3	Natural saturation	22	15	10	Up-cycle	4970	2870
S3	Natural saturation	25	18	10	Up-cycle	4973	2872
S3	Natural saturation	28	21	10	Up-cycle	4977	2873
S3	Natural saturation	32	25	10	Up-cycle	4977	2875
S3	Natural saturation	36	29	10	Up-cycle	4981	2876
S3	Natural saturation	40	33	10	Up-cycle	4981	2877
S3	Natural saturation	36	29	10	Down-cycle	4981	2877
S3	Natural saturation	32	25	10	Down-cycle	4981	2876
S3	Natural saturation	28	21	10	Down-cycle	4981	2877
S3	Natural saturation	25	18	10	Down-cycle	4981	2876
S3	Natural saturation	22	15	10	Down-cycle	4981	2876
S3	Natural saturation	19	12	10	Down-cycle	4981	2877
S3	Natural saturation	16	9	10	Down-cycle	4981	2876
S3	Natural saturation	14	7	10	Down-cycle	4977	2876
S3	Natural saturation	12	5	10	Down-cycle	4977	2875
S3	Natural saturation	10	3	10	Down-cycle	4973	2872
S3	Natural saturation	8	1	10	Down-cycle	4970	2870
S3	Natural saturation	8	1	23	Up-cycle	4853	2801
S3	Natural saturation	10	3	23	Up-cycle	4861	2807
S3	Natural saturation	12	5	23	Up-cycle	4864	2809
S3	Natural saturation	14	7	23	Up-cycle	4868	2812
S3	Natural saturation	16	9	23	Up-cycle	4875	2814
S3	Natural saturation	19	12	23	Up-cycle	4879	2818
S3	Natural saturation	22	15	23	Up-cycle	4887	2819
S3	Natural saturation	25	18	23	Up-cycle	4887	2820

S3	Natural saturation	28	21	23	Up-cycle	4894	2824
S3	Natural saturation	32	25	23	Up-cycle	4898	2825
S3	Natural saturation	36	29	23	Up-cycle	4898	2828
S3	Natural saturation	40	33	23	Up-cycle	4905	2829
S3	Natural saturation	36	29	23	Down-cycle	4901	2829
S3	Natural saturation	32	25	23	Down-cycle	4901	2828
S3	Natural saturation	28	21	23	Down-cycle	4898	2828
S3	Natural saturation	25	18	23	Down-cycle	4894	2827
S3	Natural saturation	22	15	23	Down-cycle	4894	2825
S3	Natural saturation	19	12	23	Down-cycle	4894	2825
S3	Natural saturation	16	9	23	Down-cycle	4890	2823
S3	Natural saturation	14	7	23	Down-cycle	4887	2822
S3	Natural saturation	12	5	23	Down-cycle	4883	2820
S3	Natural saturation	10	3	23	Down-cycle	4879	2818
S3	Natural saturation	8	1	23	Down-cycle	4872	2814
S3	Natural saturation	8	1	50	Up-cycle	4643	2702
S3	Natural saturation	10	3	50	Up-cycle	4653	2708
S3	Natural saturation	12	5	50	Up-cycle	4660	2712
S3	Natural saturation	14	7	50	Up-cycle	4667	2716
S3	Natural saturation	16	9	50	Up-cycle	4673	2720
S3	Natural saturation	19	12	50	Up-cycle	4684	2725
S3	Natural saturation	22	15	50	Up-cycle	4687	2729
S3	Natural saturation	25	18	50	Up-cycle	4697	2732
S3	Natural saturation	28	21	50	Up-cycle	4704	2734
S3	Natural saturation	32	25	50	Up-cycle	4711	2739
S3	Natural saturation	36	29	50	Up-cycle	4722	2742
S3	Natural saturation	40	33	50	Up-cycle	4728	2746
S3	Natural saturation	36	29	50	Down-cycle	4722	2743
S3	Natural saturation	32	25	50	Down-cycle	4718	2741
S3	Natural saturation	28	21	50	Down-cycle	4711	2738
S3	Natural saturation	25	18	50	Down-cycle	4704	2735
S3	Natural saturation	22	15	50	Down-cycle	4697	2732
S3	Natural saturation	19	12	50	Down-cycle	4691	2728
S3	Natural saturation	16	9	50	Down-cycle	4687	2724
S3	Natural saturation	14	7	50	Down-cycle	4680	2720
S3	Natural saturation	12	5	50	Down-cycle	4673	2718
S3	Natural saturation	10	3	50	Down-cycle	4667	2713
S3	Natural saturation	8	1	50	Down-cycle	4657	2708
S3	Natural saturation	8	1	75	Up-cycle	4519	2651
S3	Natural saturation	10	3	75	Up-cycle	4545	2657
S3	Natural saturation	12	5	75	Up-cycle	4564	2665

S3	Natural saturation	14	7	75	Up-cycle	4577	2672
S3	Natural saturation	16	9	75	Up-cycle	4593	2678
S3	Natural saturation	19	12	75	Up-cycle	4603	2682
S3	Natural saturation	22	15	75	Up-cycle	4616	2691
S3	Natural saturation	25	18	75	Up-cycle	4623	2694
S3	Natural saturation	28	21	75	Up-cycle	4630	2699
S3	Natural saturation	32	25	75	Up-cycle	4640	2703
S3	Natural saturation	36	29	75	Up-cycle	4646	2707
S3	Natural saturation	40	33	75	Up-cycle	4657	2711
S3	Natural saturation	36	29	75	Down-cycle	4650	2709
S3	Natural saturation	32	25	75	Down-cycle	4643	2705
S3	Natural saturation	28	21	75	Down-cycle	4633	2701
S3	Natural saturation	25	18	75	Down-cycle	4626	2696
S3	Natural saturation	22	15	75	Down-cycle	4620	2692
S3	Natural saturation	19	12	75	Down-cycle	4610	2687
S3	Natural saturation	16	9	75	Down-cycle	4603	2682
S3	Natural saturation	14	7	75	Down-cycle	4593	2679
S3	Natural saturation	12	5	75	Down-cycle	4580	2674
S3	Natural saturation	10	3	75	Down-cycle	4574	2667
S3	Natural saturation	8	1	75	Down-cycle	4554	2662
S3	Natural saturation	8	1	100	Up-cycle	4408	NaN
S3	Natural saturation	10	3	100	Up-cycle	4450	NaN
S3	Natural saturation	12	5	100	Up-cycle	4481	NaN
S3	Natural saturation	14	7	100	Up-cycle	4491	NaN
S3	Natural saturation	16	9	100	Up-cycle	4500	NaN
S3	Natural saturation	19	12	100	Up-cycle	4519	NaN
S3	Natural saturation	22	15	100	Up-cycle	4525	NaN
S3	Natural saturation	25	18	100	Up-cycle	4535	NaN
S3	Natural saturation	28	21	100	Up-cycle	4548	NaN
S3	Natural saturation	32	25	100	Up-cycle	4561	NaN
S3	Natural saturation	36	29	100	Up-cycle	4571	NaN
S3	Natural saturation	40	33	100	Up-cycle	4584	NaN
S3	Natural saturation	36	29	100	Down-cycle	4571	NaN
S3	Natural saturation	32	25	100	Down-cycle	4567	NaN
S3	Natural saturation	28	21	100	Down-cycle	4554	NaN
S3	Natural saturation	25	18	100	Down-cycle	4548	NaN
S3	Natural saturation	22	15	100	Down-cycle	4538	NaN
S3	Natural saturation	19	12	100	Down-cycle	4525	NaN
S3	Natural saturation	16	9	100	Down-cycle	4513	NaN
S3	Natural saturation	14	7	100	Down-cycle	4503	NaN
S3	Natural saturation	12	5	100	Down-cycle	4484	NaN

S3	Natural saturation	10	3	100	Down-cycle	4463	NaN
S3	Natural saturation	8	1	100	Down-cycle	4438	NaN
S3	Dry frame	8	0	10	Up-cycle	4323	2581
S3	Dry frame	10	0	10	Up-cycle	4333	2591
S3	Dry frame	12	0	10	Up-cycle	4333	2596
S3	Dry frame	14	0	10	Up-cycle	4344	2602
S3	Dry frame	16	0	10	Up-cycle	4349	2606
S3	Dry frame	19	0	10	Up-cycle	4359	2611
S3	Dry frame	22	0	10	Up-cycle	4370	2615
S3	Dry frame	25	0	10	Up-cycle	4375	2617
S3	Dry frame	28	0	10	Up-cycle	4381	2621
S3	Dry frame	32	0	10	Up-cycle	4386	2623
S3	Dry frame	36	0	10	Up-cycle	4381	2626
S3	Dry frame	40	0	10	Up-cycle	4381	2626
S3	Dry frame	36	0	10	Down-cycle	4381	2626
S3	Dry frame	32	0	10	Down-cycle	4386	2625
S3	Dry frame	28	0	10	Down-cycle	4381	2623
S3	Dry frame	25	0	10	Down-cycle	4375	2619
S3	Dry frame	22	0	10	Down-cycle	4370	2615
S3	Dry frame	19	0	10	Down-cycle	4365	2609
S3	Dry frame	16	0	10	Down-cycle	4354	2606
S3	Dry frame	14	0	10	Down-cycle	4344	2602
S3	Dry frame	12	0	10	Down-cycle	4333	2596
S3	Dry frame	10	0	10	Down-cycle	4328	2589
S3	Dry frame	8	0	10	Down-cycle	4318	2580
S3	Dry frame	8	0	23	Up-cycle	4247	2558
S3	Dry frame	10	0	23	Up-cycle	4272	2569
S3	Dry frame	12	0	23	Up-cycle	4292	2578
S3	Dry frame	14	0	23	Up-cycle	4308	2585
S3	Dry frame	16	0	23	Up-cycle	4328	2600
S3	Dry frame	19	0	23	Up-cycle	4333	2604
S3	Dry frame	22	0	23	Up-cycle	4344	2608
S3	Dry frame	25	0	23	Up-cycle	4354	2611
S3	Dry frame	28	0	23	Up-cycle	4365	2617
S3	Dry frame	32	0	23	Up-cycle	4375	2623
S3	Dry frame	36	0	23	Up-cycle	4381	2626
S3	Dry frame	40	0	23	Up-cycle	4375	2626
S3	Dry frame	36	0	23	Down-cycle	4381	2628
S3	Dry frame	32	0	23	Down-cycle	4375	2625
S3	Dry frame	28	0	23	Down-cycle	4370	2621
S3	Dry frame	25	0	23	Down-cycle	4365	2617

S3	Dry frame	22	0	23	Down-cycle	4354	2611
S3	Dry frame	19	0	23	Down-cycle	4344	2606
S3	Dry frame	16	0	23	Down-cycle	4328	2598
S3	Dry frame	14	0	23	Down-cycle	4323	2594
S3	Dry frame	12	0	23	Down-cycle	4308	2585
S3	Dry frame	10	0	23	Down-cycle	4297	2576
S3	Dry frame	8	0	23	Down-cycle	4277	2565
S3	Dry frame	8	0	50	Up-cycle	4237	2554
S3	Dry frame	10	0	50	Up-cycle	4257	2563
S3	Dry frame	12	0	50	Up-cycle	4272	2572
S3	Dry frame	14	0	50	Up-cycle	4287	2581
S3	Dry frame	16	0	50	Up-cycle	4302	2591
S3	Dry frame	19	0	50	Up-cycle	4313	2600
S3	Dry frame	22	0	50	Up-cycle	4328	2606
S3	Dry frame	25	0	50	Up-cycle	4339	2611
S3	Dry frame	28	0	50	Up-cycle	4349	2617
S3	Dry frame	32	0	50	Up-cycle	4354	2623
S3	Dry frame	36	0	50	Up-cycle	4354	2625
S3	Dry frame	40	0	50	Up-cycle	4359	2625
S3	Dry frame	36	0	50	Down-cycle	4354	2623
S3	Dry frame	32	0	50	Down-cycle	4354	2619
S3	Dry frame	28	0	50	Down-cycle	4349	2615
S3	Dry frame	25	0	50	Down-cycle	4344	2608
S3	Dry frame	22	0	50	Down-cycle	4333	2604
S3	Dry frame	19	0	50	Down-cycle	4323	2596
S3	Dry frame	16	0	50	Down-cycle	4308	2589
S3	Dry frame	14	0	50	Down-cycle	4297	2581
S3	Dry frame	12	0	50	Down-cycle	4282	2570
S3	Dry frame	10	0	50	Down-cycle	4262	2559
S3	Dry frame	8	0	50	Down-cycle	4237	2552
S3	Dry frame	8	0	75	Up-cycle	4178	2491
S3	Dry frame	10	0	75	Up-cycle	4207	2508
S3	Dry frame	12	0	75	Up-cycle	4232	2517
S3	Dry frame	14	0	75	Up-cycle	4247	2529
S3	Dry frame	16	0	75	Up-cycle	4262	2541
S3	Dry frame	19	0	75	Up-cycle	4282	2556
S3	Dry frame	22	0	75	Up-cycle	4297	2572
S3	Dry frame	25	0	75	Up-cycle	4308	2581
S3	Dry frame	28	0	75	Up-cycle	4318	2591
S3	Dry frame	32	0	75	Up-cycle	4328	2600
S3	Dry frame	36	0	75	Up-cycle	4328	2608

S3	Dry frame	40	0	75	Up-cycle	4333	2609
S3	Dry frame	36	0	75	Down-cycle	4339	2608
S3	Dry frame	32	0	75	Down-cycle	4333	2598
S3	Dry frame	28	0	75	Down-cycle	4323	2587
S3	Dry frame	25	0	75	Down-cycle	4313	2576
S3	Dry frame	22	0	75	Down-cycle	4308	2565
S3	Dry frame	19	0	75	Down-cycle	4292	2552
S3	Dry frame	16	0	75	Down-cycle	4272	2540
S3	Dry frame	14	0	75	Down-cycle	4257	2533
S3	Dry frame	12	0	75	Down-cycle	4242	2526
S3	Dry frame	10	0	75	Down-cycle	4217	2520
S3	Dry frame	8	0	75	Down-cycle	4188	2511
S3	Dry frame	8	0	100	Up-cycle	4107	NaN
S3	Dry frame	10	0	100	Up-cycle	4140	NaN
S3	Dry frame	12	0	100	Up-cycle	4168	NaN
S3	Dry frame	14	0	100	Up-cycle	4193	NaN
S3	Dry frame	16	0	100	Up-cycle	4212	NaN
S3	Dry frame	19	0	100	Up-cycle	4237	NaN
S3	Dry frame	22	0	100	Up-cycle	4257	NaN
S3	Dry frame	25	0	100	Up-cycle	4272	NaN
S3	Dry frame	28	0	100	Up-cycle	4282	NaN
S3	Dry frame	32	0	100	Up-cycle	4287	NaN
S3	Dry frame	36	0	100	Up-cycle	4292	NaN
S3	Dry frame	40	0	100	Up-cycle	4297	NaN
S3	Dry frame	36	0	100	Down-cycle	4297	NaN
S3	Dry frame	32	0	100	Down-cycle	4292	NaN
S3	Dry frame	28	0	100	Down-cycle	4287	NaN
S3	Dry frame	25	0	100	Down-cycle	4277	NaN
S3	Dry frame	22	0	100	Down-cycle	4272	NaN
S3	Dry frame	19	0	100	Down-cycle	4247	NaN
S3	Dry frame	16	0	100	Down-cycle	4227	NaN
S3	Dry frame	14	0	100	Down-cycle	4207	NaN
S3	Dry frame	12	0	100	Down-cycle	4188	NaN
S3	Dry frame	10	0	100	Down-cycle	4154	NaN
S3	Dry frame	8	0	100	Down-cycle	4116	NaN
S3	Water saturation	8	1	10	Up-cycle	4354	2506
S3	Water saturation	10	3	10	Up-cycle	4359	2508
S3	Water saturation	12	5	10	Up-cycle	4359	2510
S3	Water saturation	14	7	10	Up-cycle	4359	2510
S3	Water saturation	16	9	10	Up-cycle	4365	2508
S3	Water saturation	19	12	10	Up-cycle	4365	2510

S3	Water saturation	22	15	10	Up-cycle	4370	2510
S3	Water saturation	25	18	10	Up-cycle	4370	2510
S3	Water saturation	28	21	10	Up-cycle	4375	2511
S3	Water saturation	32	25	10	Up-cycle	4381	2510
S3	Water saturation	36	29	10	Up-cycle	4381	2511
S3	Water saturation	40	33	10	Up-cycle	4386	2511
S3	Water saturation	36	29	10	Down-cycle	4381	2511
S3	Water saturation	32	25	10	Down-cycle	4381	2510
S3	Water saturation	28	21	10	Down-cycle	4375	2510
S3	Water saturation	25	18	10	Down-cycle	4370	2510
S3	Water saturation	22	15	10	Down-cycle	4365	2508
S3	Water saturation	19	12	10	Down-cycle	4359	2506
S3	Water saturation	16	9	10	Down-cycle	4354	2508
S3	Water saturation	14	7	10	Down-cycle	4354	2506
S3	Water saturation	12	5	10	Down-cycle	4349	2505
S3	Water saturation	10	3	10	Down-cycle	4354	2506
S3	Water saturation	8	1	10	Down-cycle	4349	2505
S3	Water saturation	8	1	23	Up-cycle	4344	2506
S3	Water saturation	10	3	23	Up-cycle	4349	2506
S3	Water saturation	12	5	23	Up-cycle	4349	2506
S3	Water saturation	14	7	23	Up-cycle	4349	2506
S3	Water saturation	16	9	23	Up-cycle	4354	2505
S3	Water saturation	19	12	23	Up-cycle	4359	2505
S3	Water saturation	22	15	23	Up-cycle	4354	2505
S3	Water saturation	25	18	23	Up-cycle	4359	2505
S3	Water saturation	28	21	23	Up-cycle	4365	2505
S3	Water saturation	32	25	23	Up-cycle	4370	2508
S3	Water saturation	36	29	23	Up-cycle	4375	2508
S3	Water saturation	40	33	23	Up-cycle	4375	2508
S3	Water saturation	36	29	23	Down-cycle	4381	2510
S3	Water saturation	32	25	23	Down-cycle	4375	2508
S3	Water saturation	28	21	23	Down-cycle	4370	2508
S3	Water saturation	25	18	23	Down-cycle	4365	2506
S3	Water saturation	22	15	23	Down-cycle	4359	2505
S3	Water saturation	19	12	23	Down-cycle	4354	2505
S3	Water saturation	16	9	23	Down-cycle	4349	2503
S3	Water saturation	14	7	23	Down-cycle	4349	2503
S3	Water saturation	12	5	23	Down-cycle	4344	2503
S3	Water saturation	10	3	23	Down-cycle	4344	2501
S3	Water saturation	8	1	23	Down-cycle	4344	2499
S3	Water saturation	8	1	50	Up-cycle	4302	2480

S3	Water saturation	10	3	50	Up-cycle	4308	2480
S3	Water saturation	12	5	50	Up-cycle	4308	2480
S3	Water saturation	14	7	50	Up-cycle	4313	2480
S3	Water saturation	16	9	50	Up-cycle	4318	2482
S3	Water saturation	19	12	50	Up-cycle	4339	2482
S3	Water saturation	22	15	50	Up-cycle	4344	2487
S3	Water saturation	25	18	50	Up-cycle	4349	2492
S3	Water saturation	28	21	50	Up-cycle	4349	2492
S3	Water saturation	32	25	50	Up-cycle	4354	2491
S3	Water saturation	36	29	50	Up-cycle	4359	2491
S3	Water saturation	40	33	50	Up-cycle	4365	2489
S3	Water saturation	36	29	50	Down-cycle	4359	2487
S3	Water saturation	32	25	50	Down-cycle	4349	2487
S3	Water saturation	28	21	50	Down-cycle	4344	2489
S3	Water saturation	25	18	50	Down-cycle	4344	2489
S3	Water saturation	22	15	50	Down-cycle	4339	2489
S3	Water saturation	19	12	50	Down-cycle	4333	2486
S3	Water saturation	16	9	50	Down-cycle	4328	2482
S3	Water saturation	14	7	50	Down-cycle	4328	2479
S3	Water saturation	12	5	50	Down-cycle	4328	2479
S3	Water saturation	10	3	50	Down-cycle	4323	2479
S3	Water saturation	8	1	50	Down-cycle	4302	2477
S3	Water saturation	8	1	75	Up-cycle	4252	NaN
S3	Water saturation	10	3	75	Up-cycle	4257	NaN
S3	Water saturation	12	5	75	Up-cycle	4262	NaN
S3	Water saturation	14	7	75	Up-cycle	4277	NaN
S3	Water saturation	16	9	75	Up-cycle	4282	NaN
S3	Water saturation	19	12	75	Up-cycle	4287	NaN
S3	Water saturation	22	15	75	Up-cycle	4292	NaN
S3	Water saturation	25	18	75	Up-cycle	4292	NaN
S3	Water saturation	28	21	75	Up-cycle	4297	NaN
S3	Water saturation	32	25	75	Up-cycle	4308	NaN
S3	Water saturation	36	29	75	Up-cycle	4308	NaN
S3	Water saturation	40	33	75	Up-cycle	4318	NaN
S3	Water saturation	36	29	75	Down-cycle	4313	NaN
S3	Water saturation	32	25	75	Down-cycle	4308	NaN
S3	Water saturation	28	21	75	Down-cycle	4297	NaN
S3	Water saturation	25	18	75	Down-cycle	4292	NaN
S3	Water saturation	22	15	75	Down-cycle	4292	NaN
S3	Water saturation	19	12	75	Down-cycle	4282	NaN
S3	Water saturation	16	9	75	Down-cycle	4277	NaN

S3	Water saturation	14	7	75	Down-cycle	4272	NaN
S3	Water saturation	12	5	75	Down-cycle	4272	NaN
S3	Water saturation	10	3	75	Down-cycle	4267	NaN
S3	Water saturation	8	1	75	Down-cycle	4262	NaN
S3	Water saturation	8	1	100	Up-cycle	4173	NaN
S3	Water saturation	10	3	100	Up-cycle	4178	NaN
S3	Water saturation	12	5	100	Up-cycle	4178	NaN
S3	Water saturation	14	7	100	Up-cycle	4178	NaN
S3	Water saturation	16	9	100	Up-cycle	4183	NaN
S3	Water saturation	19	12	100	Up-cycle	4183	NaN
S3	Water saturation	22	15	100	Up-cycle	4193	NaN
S3	Water saturation	25	18	100	Up-cycle	4197	NaN
S3	Water saturation	28	21	100	Up-cycle	4202	NaN
S3	Water saturation	32	25	100	Up-cycle	4207	NaN
S3	Water saturation	36	29	100	Up-cycle	4222	NaN
S3	Water saturation	40	33	100	Up-cycle	4232	NaN
S3	Water saturation	36	29	100	Down-cycle	4222	NaN
S3	Water saturation	32	25	100	Down-cycle	4212	NaN
S3	Water saturation	28	21	100	Down-cycle	4202	NaN
S3	Water saturation	25	18	100	Down-cycle	4197	NaN
S3	Water saturation	22	15	100	Down-cycle	4193	NaN
S3	Water saturation	19	12	100	Down-cycle	4188	NaN
S3	Water saturation	16	9	100	Down-cycle	4178	NaN
S3	Water saturation	14	7	100	Down-cycle	4178	NaN
S3	Water saturation	12	5	100	Down-cycle	4173	NaN
S3	Water saturation	10	3	100	Down-cycle	4168	NaN
S3	Water saturation	8	1	100	Down-cycle	4164	NaN
S6	Natural saturation	7	0	10	Up-cycle	5704	3089
S6	Natural saturation	10	0	10	Up-cycle	5725	3098
S6	Natural saturation	20	0	10	Up-cycle	5735	3157
S6	Natural saturation	30	0	10	Up-cycle	5756	3198
S6	Natural saturation	7	0	20	Up-cycle	5653	3068
S6	Natural saturation	10	0	20	Up-cycle	5663	3071
S6	Natural saturation	20	0	20	Up-cycle	5694	3132
S6	Natural saturation	30	0	20	Up-cycle	5714	3179
S6	Natural saturation	7	0	30	Up-cycle	5603	3062
S6	Natural saturation	10	0	30	Up-cycle	5623	3059
S6	Natural saturation	20	0	30	Up-cycle	5653	3123
S6	Natural saturation	30	0	30	Up-cycle	5673	3166
S6	Natural saturation	7	0	40	Up-cycle	5534	3027
S6	Natural saturation	10	0	40	Up-cycle	5544	3033

S6	Natural saturation	20	0	40	Up-cycle	5593	3098
S6	Natural saturation	30	0	40	Up-cycle	5623	3144
S6	Natural saturation	7	0	50	Up-cycle	5496	3012
S6	Natural saturation	10	0	50	Up-cycle	5515	3021
S6	Natural saturation	20	0	50	Up-cycle	5573	3080
S6	Natural saturation	30	0	50	Up-cycle	5603	3123
S6	Natural saturation	7	0	60	Up-cycle	5467	2992
S6	Natural saturation	10	0	60	Up-cycle	5477	2998
S6	Natural saturation	20	0	60	Up-cycle	5534	3059
S6	Natural saturation	30	0	60	Up-cycle	5563	3101
S6	Natural saturation	7	0	70	Up-cycle	5411	2967
S6	Natural saturation	10	0	70	Up-cycle	5439	2976
S6	Natural saturation	20	0	70	Up-cycle	5505	3047
S6	Natural saturation	30	0	70	Up-cycle	5534	3089
S6	Natural saturation	7	0	80	Up-cycle	5383	2951
S6	Natural saturation	10	0	80	Up-cycle	5392	2956
S6	Natural saturation	20	0	80	Up-cycle	5448	3024
S6	Natural saturation	30	0	80	Up-cycle	5496	3065
S6	Natural saturation	7	0	90	Up-cycle	5365	2937
S6	Natural saturation	10	0	90	Up-cycle	5365	2937
S6	Natural saturation	20	0	90	Up-cycle	5420	3004
S6	Natural saturation	30	0	90	Up-cycle	5467	3053
S6	Natural saturation	7	0	100	Up-cycle	5338	2904
S6	Natural saturation	10	0	100	Up-cycle	5347	2915
S6	Natural saturation	20	0	100	Up-cycle	5402	2990
S6	Natural saturation	30	0	100	Up-cycle	5439	3036
S6	Natural saturation	7	0	10	Up-cycle	5766	3173
S6	Natural saturation	10	3	10	Up-cycle	5777	3176
S6	Natural saturation	20	13	10	Up-cycle	5788	3192
S6	Natural saturation	30	23	10	Up-cycle	5798	3202
S6	Natural saturation	7	0	20	Up-cycle	5694	3104
S6	Natural saturation	10	3	20	Up-cycle	5714	3113
S6	Natural saturation	20	13	20	Up-cycle	5725	3138
S6	Natural saturation	30	23	20	Up-cycle	5745	3157
S6	Natural saturation	7	0	30	Up-cycle	5643	3065
S6	Natural saturation	10	3	30	Up-cycle	5653	3065
S6	Natural saturation	20	13	30	Up-cycle	5683	3095
S6	Natural saturation	30	23	30	Up-cycle	5694	3116
S6	Natural saturation	7	0	40	Up-cycle	5573	3036
S6	Natural saturation	10	3	40	Up-cycle	5583	3041
S6	Natural saturation	20	13	40	Up-cycle	5613	3071

S6	Natural saturation	30	23	40	Up-cycle	5633	3089
S6	Natural saturation	7	0	50	Up-cycle	5524	3012
S6	Natural saturation	10	3	50	Up-cycle	5534	3018
S6	Natural saturation	20	13	50	Up-cycle	5573	3044
S6	Natural saturation	30	23	50	Up-cycle	5593	3068
S6	Natural saturation	7	0	60	Up-cycle	5486	2998
S6	Natural saturation	10	3	60	Up-cycle	5486	3001
S6	Natural saturation	20	13	60	Up-cycle	5524	3024
S6	Natural saturation	30	23	60	Up-cycle	5554	3044
S6	Natural saturation	7	0	70	Up-cycle	5420	2970
S6	Natural saturation	10	3	70	Up-cycle	5439	2978
S6	Natural saturation	20	13	70	Up-cycle	5486	3004
S6	Natural saturation	30	23	70	Up-cycle	5515	3033
S6	Natural saturation	7	0	80	Up-cycle	5420	2976
S6	Natural saturation	10	3	80	Up-cycle	5430	2978
S6	Natural saturation	20	13	80	Up-cycle	5467	2995
S6	Natural saturation	30	23	80	Up-cycle	5496	3012
S6	Natural saturation	7	0	90	Up-cycle	5329	2923
S6	Natural saturation	10	3	90	Up-cycle	5329	2929
S6	Natural saturation	20	13	90	Up-cycle	5392	2951
S6	Natural saturation	30	23	90	Up-cycle	5430	2970
S6	Natural saturation	7	0	100	Up-cycle	5311	2904
S6	Natural saturation	10	3	100	Up-cycle	5311	2921
S6	Natural saturation	20	13	100	Up-cycle	5365	2934
S6	Natural saturation	30	23	100	Up-cycle	5402	2951
S6	Dry frame	7	0	10	Up-cycle	5426	3024
S6	Dry frame	10	0	10	Up-cycle	5454	3030
S6	Dry frame	20	0	10	Up-cycle	5426	3062
S6	Dry frame	30	0	10	Up-cycle	5408	3144
S6	Dry frame	7	0	20	Up-cycle	5454	3033
S6	Dry frame	10	0	20	Up-cycle	5464	3030
S6	Dry frame	20	0	20	Up-cycle	5426	3077
S6	Dry frame	30	0	20	Up-cycle	5408	3138
S6	Dry frame	7	0	30	Up-cycle	5464	3041
S6	Dry frame	10	0	30	Up-cycle	5483	3027
S6	Dry frame	20	0	30	Up-cycle	5426	3080
S6	Dry frame	30	0	30	Up-cycle	5417	3144
S6	Dry frame	7	0	40	Up-cycle	5445	3024
S6	Dry frame	10	0	40	Up-cycle	5454	3018
S6	Dry frame	20	0	40	Up-cycle	5408	3074
S6	Dry frame	30	0	40	Up-cycle	5389	3135

S6	Dry frame	7	0	50	Up-cycle	5454	3018
S6	Dry frame	10	0	50	Up-cycle	5464	3015
S6	Dry frame	20	0	50	Up-cycle	5408	3068
S6	Dry frame	30	0	50	Up-cycle	5389	3128
S6	Dry frame	7	0	60	Up-cycle	5464	3012
S6	Dry frame	10	0	60	Up-cycle	5454	3004
S6	Dry frame	20	0	60	Up-cycle	5408	3062
S6	Dry frame	30	0	60	Up-cycle	5389	3122
S6	Dry frame	7	0	70	Up-cycle	5445	2995
S6	Dry frame	10	0	70	Up-cycle	5454	2995
S6	Dry frame	20	0	70	Up-cycle	5399	3059
S6	Dry frame	30	0	70	Up-cycle	5380	3116
S6	Dry frame	7	0	80	Up-cycle	5426	2981
S6	Dry frame	10	0	80	Up-cycle	5436	2981
S6	Dry frame	20	0	80	Up-cycle	5445	3047
S6	Dry frame	30	0	80	Up-cycle	5436	3110
S6	Dry frame	7	0	90	Up-cycle	5436	2978
S6	Dry frame	10	0	90	Up-cycle	5426	2978
S6	Dry frame	20	0	90	Up-cycle	5389	3062
S6	Dry frame	30	0	90	Up-cycle	5389	3113
S6	Dry frame	7	0	100	Up-cycle	5426	NaN
S6	Dry frame	10	0	100	Up-cycle	5436	2978
S6	Dry frame	20	0	100	Up-cycle	5380	3047
S6	Dry frame	30	0	100	Up-cycle	5371	3101
S6	Water saturation	7	0	10	Up-cycle	5550	2918
S6	Water saturation	10	3	10	Up-cycle	5492	2913
S6	Water saturation	20	13	10	Up-cycle	5502	2910
S6	Water saturation	30	23	10	Up-cycle	5511	2910
S6	Water saturation	7	0	20	Up-cycle	5550	2889
S6	Water saturation	10	3	20	Up-cycle	5473	2889
S6	Water saturation	20	13	20	Up-cycle	5483	2889
S6	Water saturation	30	23	20	Up-cycle	5492	2886
S6	Water saturation	7	0	30	Up-cycle	5540	2902
S6	Water saturation	10	3	30	Up-cycle	5492	2899
S6	Water saturation	20	13	30	Up-cycle	5502	2894
S6	Water saturation	30	23	30	Up-cycle	5502	2894
S6	Water saturation	7	0	40	Up-cycle	5502	2868
S6	Water saturation	10	3	40	Up-cycle	5454	2868
S6	Water saturation	20	13	40	Up-cycle	5464	2868
S6	Water saturation	30	23	40	Up-cycle	5473	2865
S6	Water saturation	7	0	50	Up-cycle	5483	2845

S6	Water saturation	10	3	50	Up-cycle	5426	2845
S6	Water saturation	20	13	50	Up-cycle	5445	2842
S6	Water saturation	30	23	50	Up-cycle	5454	2847
S6	Water saturation	7	0	60	Up-cycle	5502	2835
S6	Water saturation	10	3	60	Up-cycle	5408	2822
S6	Water saturation	20	13	60	Up-cycle	5417	2824
S6	Water saturation	30	23	60	Up-cycle	5436	2829
S6	Water saturation	7	0	70	Up-cycle	5454	2817
S6	Water saturation	10	3	70	Up-cycle	5380	2812
S6	Water saturation	20	13	70	Up-cycle	5389	2809
S6	Water saturation	30	23	70	Up-cycle	5408	2809
S6	Water saturation	7	0	80	Up-cycle	5426	2792
S6	Water saturation	10	3	80	Up-cycle	5326	2782
S6	Water saturation	20	13	80	Up-cycle	5335	2785
S6	Water saturation	30	23	80	Up-cycle	5353	2785
S6	Water saturation	7	0	90	Up-cycle	5380	2782
S6	Water saturation	10	3	90	Up-cycle	5282	2768
S6	Water saturation	20	13	90	Up-cycle	5299	2770
S6	Water saturation	30	23	90	Up-cycle	5308	2773
S6	Water saturation	7	0	100	Up-cycle	5221	2763
S6	Water saturation	10	3	100	Up-cycle	5178	2727
S6	Water saturation	20	13	100	Up-cycle	5221	2739
S6	Water saturation	30	23	100	Up-cycle	5238	2746
S8	Natural saturation	7	0	10	Up-cycle	4627	2805
S8	Natural saturation	10	0	10	Up-cycle	4664	2821
S8	Natural saturation	20	0	10	Up-cycle	4753	2860
S8	Natural saturation	30	0	10	Up-cycle	4799	2881
S8	Natural saturation	7	0	20	Up-cycle	4591	2798
S8	Natural saturation	10	0	20	Up-cycle	4621	2809
S8	Natural saturation	20	0	20	Up-cycle	4696	2839
S8	Natural saturation	30	0	20	Up-cycle	4728	2862
S8	Natural saturation	7	0	30	Up-cycle	4485	2760
S8	Natural saturation	10	0	30	Up-cycle	4525	2769
S8	Natural saturation	20	0	30	Up-cycle	4609	2809
S8	Natural saturation	30	0	30	Up-cycle	4646	2837
S8	Natural saturation	7	0	40	Up-cycle	4433	2739
S8	Natural saturation	10	0	40	Up-cycle	4462	2752
S8	Natural saturation	20	0	40	Up-cycle	4549	2793
S8	Natural saturation	30	0	40	Up-cycle	4591	2818
S8	Natural saturation	7	0	50	Up-cycle	4378	2711
S8	Natural saturation	10	0	50	Up-cycle	4411	2728

S8	Natural saturation	20	0	50	Up-cycle	4496	2769
S8	Natural saturation	30	0	50	Up-cycle	4537	2800
S8	Natural saturation	7	0	60	Up-cycle	4307	2686
S8	Natural saturation	10	0	60	Up-cycle	4340	2698
S8	Natural saturation	20	0	60	Up-cycle	4428	2745
S8	Natural saturation	30	0	60	Up-cycle	4479	2773
S8	Natural saturation	7	0	70	Up-cycle	4229	2657
S8	Natural saturation	10	0	70	Up-cycle	4271	2674
S8	Natural saturation	20	0	70	Up-cycle	4367	2724
S8	Natural saturation	30	0	70	Up-cycle	4422	2758
S8	Natural saturation	7	0	80	Up-cycle	4194	2651
S8	Natural saturation	10	0	80	Up-cycle	4224	2665
S8	Natural saturation	20	0	80	Up-cycle	4323	2715
S8	Natural saturation	30	0	80	Up-cycle	4383	2747
S8	Natural saturation	7	0	90	Up-cycle	4144	2631
S8	Natural saturation	10	0	90	Up-cycle	4178	2649
S8	Natural saturation	20	0	90	Up-cycle	4276	2703
S8	Natural saturation	30	0	90	Up-cycle	4334	2739
S8	Natural saturation	7	0	100	Up-cycle	4105	2621
S8	Natural saturation	10	0	100	Up-cycle	4139	2637
S8	Natural saturation	20	0	100	Up-cycle	4245	2692
S8	Natural saturation	30	0	100	Up-cycle	4302	2730
S8	Natural saturation	7	0	10	Up-cycle	4853	2929
S8	Natural saturation	10	3	10	Up-cycle	4832	2932
S8	Natural saturation	20	13	10	Up-cycle	4880	2925
S8	Natural saturation	30	23	10	Up-cycle	4893	2934
S8	Natural saturation	7	0	20	Up-cycle	4728	2869
S8	Natural saturation	10	3	20	Up-cycle	4747	2865
S8	Natural saturation	20	13	20	Up-cycle	4793	2886
S8	Natural saturation	30	23	20	Up-cycle	4812	2903
S8	Natural saturation	7	0	30	Up-cycle	4627	2827
S8	Natural saturation	10	3	30	Up-cycle	4652	2830
S8	Natural saturation	20	13	30	Up-cycle	4702	2850
S8	Natural saturation	30	23	30	Up-cycle	4734	2872
S8	Natural saturation	7	0	40	Up-cycle	4549	2793
S8	Natural saturation	10	3	40	Up-cycle	4573	2802
S8	Natural saturation	20	13	40	Up-cycle	4640	2832
S8	Natural saturation	30	23	40	Up-cycle	4664	2850
S8	Natural saturation	7	0	50	Up-cycle	4473	2765
S8	Natural saturation	10	3	50	Up-cycle	4502	2754
S8	Natural saturation	20	13	50	Up-cycle	4573	2793

S8	Natural saturation	30	23	50	Up-cycle	4603	2823
S8	Natural saturation	7	0	60	Up-cycle	4411	2728
S8	Natural saturation	10	3	60	Up-cycle	4433	2739
S8	Natural saturation	20	13	60	Up-cycle	4508	2776
S8	Natural saturation	30	23	60	Up-cycle	4543	2798
S8	Natural saturation	7	0	70	Up-cycle	4323	2694
S8	Natural saturation	10	3	70	Up-cycle	4367	2711
S8	Natural saturation	20	13	70	Up-cycle	4450	2754
S8	Natural saturation	30	23	70	Up-cycle	4490	2782
S8	Natural saturation	7	0	80	Up-cycle	4271	2680
S8	Natural saturation	10	3	80	Up-cycle	4302	2694
S8	Natural saturation	20	13	80	Up-cycle	4394	2741
S8	Natural saturation	30	23	80	Up-cycle	4445	2771
S8	Natural saturation	7	0	90	Up-cycle	4214	2657
S8	Natural saturation	10	3	90	Up-cycle	4245	2674
S8	Natural saturation	20	13	90	Up-cycle	4340	2726
S8	Natural saturation	30	23	90	Up-cycle	4389	2758
S8	Natural saturation	7	0	100	Up-cycle	4194	2647
S8	Natural saturation	10	3	100	Up-cycle	4214	2653
S8	Natural saturation	20	13	100	Up-cycle	4302	2690
S8	Natural saturation	30	23	100	Up-cycle	4367	2717
S8	Dry frame	7	0	10	Up-cycle	3802	2677
S8	Dry frame	10	0	10	Up-cycle	3891	2704
S8	Dry frame	20	0	10	Up-cycle	4150	2789
S8	Dry frame	30	0	10	Up-cycle	4271	2829
S8	Dry frame	7	0	20	Up-cycle	3961	2732
S8	Dry frame	10	0	20	Up-cycle	4011	2747
S8	Dry frame	20	0	20	Up-cycle	4174	2793
S8	Dry frame	30	0	20	Up-cycle	4271	2827
S8	Dry frame	7	0	30	Up-cycle	3993	2743
S8	Dry frame	10	0	30	Up-cycle	4035	2749
S8	Dry frame	20	0	30	Up-cycle	4184	2793
S8	Dry frame	30	0	30	Up-cycle	4277	2825
S8	Dry frame	7	0	40	Up-cycle	3979	2725
S8	Dry frame	10	0	40	Up-cycle	4030	2743
S8	Dry frame	20	0	40	Up-cycle	4179	2786
S8	Dry frame	30	0	40	Up-cycle	4266	2815
S8	Dry frame	7	0	50	Up-cycle	3975	2711
S8	Dry frame	10	0	50	Up-cycle	4030	2728
S8	Dry frame	20	0	50	Up-cycle	4179	2775
S8	Dry frame	30	0	50	Up-cycle	4256	2806

S8	Dry frame	7	0	60	Up-cycle	3979	2704
S8	Dry frame	10	0	60	Up-cycle	4025	2719
S8	Dry frame	20	0	60	Up-cycle	4169	2766
S8	Dry frame	30	0	60	Up-cycle	4251	2795
S8	Dry frame	7	0	70	Up-cycle	3961	2690
S8	Dry frame	10	0	70	Up-cycle	4021	2711
S8	Dry frame	20	0	70	Up-cycle	4164	2758
S8	Dry frame	30	0	70	Up-cycle	4245	2786
S8	Dry frame	7	0	80	Up-cycle	3917	2671
S8	Dry frame	10	0	80	Up-cycle	3979	2690
S8	Dry frame	20	0	80	Up-cycle	4140	2740
S8	Dry frame	30	0	80	Up-cycle	4220	2773
S8	Dry frame	7	0	90	Up-cycle	3908	2659
S8	Dry frame	10	0	90	Up-cycle	3961	2682
S8	Dry frame	20	0	90	Up-cycle	4120	2732
S8	Dry frame	30	0	90	Up-cycle	4200	2769
S8	Dry frame	7	0	100	Up-cycle	3921	2665
S8	Dry frame	10	0	100	Up-cycle	3970	2684
S8	Dry frame	20	0	100	Up-cycle	4115	2728
S8	Dry frame	30	0	100	Up-cycle	4189	2762
S8	Water saturation	7	0	10	Up-cycle	4368	2651
S8	Water saturation	10	3	10	Up-cycle	4368	2651
S8	Water saturation	20	13	10	Up-cycle	4378	2647
S8	Water saturation	30	23	10	Up-cycle	4384	2641
S8	Water saturation	7	0	20	Up-cycle	4362	2635
S8	Water saturation	10	3	20	Up-cycle	4357	2631
S8	Water saturation	20	13	20	Up-cycle	4373	2629
S8	Water saturation	30	23	20	Up-cycle	4384	2631
S8	Water saturation	7	0	30	Up-cycle	4314	2623
S8	Water saturation	10	3	30	Up-cycle	4346	2619
S8	Water saturation	20	13	30	Up-cycle	4362	2617
S8	Water saturation	30	23	30	Up-cycle	4373	2615
S8	Water saturation	7	0	40	Up-cycle	4324	2617
S8	Water saturation	10	3	40	Up-cycle	4335	2613
S8	Water saturation	20	13	40	Up-cycle	4330	2598
S8	Water saturation	30	23	40	Up-cycle	4357	2604
S8	Water saturation	7	0	50	Up-cycle	4282	2582
S8	Water saturation	10	3	50	Up-cycle	4298	2579
S8	Water saturation	20	13	50	Up-cycle	4314	2581
S8	Water saturation	30	23	50	Up-cycle	4324	2581
S8	Water saturation	7	0	60	Up-cycle	4261	2558

S8	Water saturation	10	3	60	Up-cycle	4266	2554
S8	Water saturation	20	13	60	Up-cycle	4282	2554
S8	Water saturation	30	23	60	Up-cycle	4292	2554
S8	Water saturation	7	0	70	Up-cycle	4220	2532
S8	Water saturation	10	3	70	Up-cycle	4235	2530
S8	Water saturation	20	13	70	Up-cycle	4245	2534
S8	Water saturation	30	23	70	Up-cycle	4266	2534
S8	Water saturation	7	0	80	Up-cycle	4184	2508
S8	Water saturation	10	3	80	Up-cycle	4189	2508
S8	Water saturation	20	13	80	Up-cycle	4205	2510
S8	Water saturation	30	23	80	Up-cycle	4215	2512
S8	Water saturation	7	0	90	Up-cycle	4145	2494
S8	Water saturation	10	3	90	Up-cycle	4150	2496
S8	Water saturation	20	13	90	Up-cycle	4164	2497
S8	Water saturation	30	23	90	Up-cycle	4179	2499
S8	Water saturation	7	0	100	Up-cycle	4130	2485
S8	Water saturation	10	3	100	Up-cycle	4125	2496
S8	Water saturation	20	13	100	Up-cycle	4125	2489
S8	Water saturation	30	23	100	Up-cycle	4135	2487
S15	Natural saturation	7	0	10	Up-cycle	5488	3165
S15	Natural saturation	10	0	10	Up-cycle	5497	3165
S15	Natural saturation	20	0	10	Up-cycle	5515	3168
S15	Natural saturation	30	0	10	Up-cycle	5524	3171
S15	Natural saturation	7	0	20	Up-cycle	5470	3162
S15	Natural saturation	10	0	20	Up-cycle	5470	3159
S15	Natural saturation	20	0	20	Up-cycle	5470	3147
S15	Natural saturation	30	0	20	Up-cycle	5470	3147
S15	Natural saturation	7	0	30	Up-cycle	5340	3100
S15	Natural saturation	10	0	30	Up-cycle	5348	3095
S15	Natural saturation	20	0	30	Up-cycle	5391	3109
S15	Natural saturation	30	0	30	Up-cycle	5417	3115
S15	Natural saturation	7	0	40	Up-cycle	5323	3092
S15	Natural saturation	10	0	40	Up-cycle	5323	3092
S15	Natural saturation	20	0	40	Up-cycle	5348	3095
S15	Natural saturation	30	0	40	Up-cycle	5374	3098
S15	Natural saturation	7	0	50	Up-cycle	5256	3058
S15	Natural saturation	10	0	50	Up-cycle	5273	3064
S15	Natural saturation	20	0	50	Up-cycle	5323	3075
S15	Natural saturation	30	0	50	Up-cycle	5340	3083
S15	Natural saturation	7	0	60	Up-cycle	5207	3036
S15	Natural saturation	10	0	60	Up-cycle	5207	3039

S15	Natural saturation	20	0	60	Up-cycle	5273	3055
S15	Natural saturation	30	0	60	Up-cycle	5298	3061
S15	Natural saturation	7	0	70	Up-cycle	5136	3012
S15	Natural saturation	10	0	70	Up-cycle	NaN	3020
S15	Natural saturation	20	0	70	Up-cycle	5232	3039
S15	Natural saturation	30	0	70	Up-cycle	5264	3044
S15	Natural saturation	7	0	80	Up-cycle	5066	2985
S15	Natural saturation	10	0	80	Up-cycle	5089	2990
S15	Natural saturation	20	0	80	Up-cycle	5167	3014
S15	Natural saturation	30	0	80	Up-cycle	5207	3022
S15	Natural saturation	7	0	90	Up-cycle	5021	2956
S15	Natural saturation	10	0	90	Up-cycle	5051	2969
S15	Natural saturation	20	0	90	Up-cycle	5136	3001
S15	Natural saturation	30	0	90	Up-cycle	5183	3014
S15	Natural saturation	7	0	100	Up-cycle	4976	2941
S15	Natural saturation	10	0	100	Up-cycle	5006	2951
S15	Natural saturation	20	0	100	Up-cycle	5097	2988
S15	Natural saturation	30	0	100	Up-cycle	5152	3001
S15	Natural saturation	7	0	10	Up-cycle	5400	3135
S15	Natural saturation	10	3	10	Up-cycle	5417	3135
S15	Natural saturation	20	13	10	Up-cycle	5443	3144
S15	Natural saturation	30	23	10	Up-cycle	5461	3150
S15	Natural saturation	7	0	20	Up-cycle	5426	3156
S15	Natural saturation	10	3	20	Up-cycle	5435	3150
S15	Natural saturation	20	13	20	Up-cycle	5443	3144
S15	Natural saturation	30	23	20	Up-cycle	5443	3144
S15	Natural saturation	7	0	30	Up-cycle	5340	3121
S15	Natural saturation	10	3	30	Up-cycle	5357	3115
S15	Natural saturation	20	13	30	Up-cycle	5382	3118
S15	Natural saturation	30	23	30	Up-cycle	5382	3112
S15	Natural saturation	7	0	40	Up-cycle	5264	3081
S15	Natural saturation	10	3	40	Up-cycle	5273	3078
S15	Natural saturation	20	13	40	Up-cycle	5306	3081
S15	Natural saturation	30	23	40	Up-cycle	5323	3078
S15	Natural saturation	7	0	50	Up-cycle	5207	3042
S15	Natural saturation	10	3	50	Up-cycle	5224	3047
S15	Natural saturation	20	13	50	Up-cycle	5264	3055
S15	Natural saturation	30	23	50	Up-cycle	5289	3061
S15	Natural saturation	7	0	60	Up-cycle	5160	3017
S15	Natural saturation	10	3	60	Up-cycle	5167	3014
S15	Natural saturation	20	13	60	Up-cycle	5224	3025

S15	Natural saturation	30	23	60	Up-cycle	5248	3031
S15	Natural saturation	7	0	70	Up-cycle	5089	2980
S15	Natural saturation	10	3	70	Up-cycle	5105	2982
S15	Natural saturation	20	13	70	Up-cycle	5152	2996
S15	Natural saturation	30	23	70	Up-cycle	5175	2998
S15	Natural saturation	7	0	80	Up-cycle	5013	2930
S15	Natural saturation	10	3	80	Up-cycle	5021	2935
S15	Natural saturation	20	13	80	Up-cycle	5089	NaN
S15	Natural saturation	30	23	80	Up-cycle	5120	2972
S15	Natural saturation	7	0	90	Up-cycle	4954	2905
S15	Natural saturation	10	3	90	Up-cycle	4969	2910
S15	Natural saturation	20	13	90	Up-cycle	5051	2951
S15	Natural saturation	30	23	90	Up-cycle	5105	2966
S15	Natural saturation	7	0	100	Up-cycle	4861	2868
S15	Natural saturation	10	3	100	Up-cycle	4875	2875
S15	Natural saturation	20	13	100	Up-cycle	4954	2905
S15	Natural saturation	30	23	100	Up-cycle	5028	2930
S15	Dry frame	7	0	10	Up-cycle	5149	3136
S15	Dry frame	10	0	10	Up-cycle	5157	3136
S15	Dry frame	20	0	10	Up-cycle	5237	3145
S15	Dry frame	30	0	10	Up-cycle	5295	3157
S15	Dry frame	7	0	20	Up-cycle	5142	3134
S15	Dry frame	10	0	20	Up-cycle	5157	3131
S15	Dry frame	20	0	20	Up-cycle	5237	3139
S15	Dry frame	30	0	20	Up-cycle	5295	3154
S15	Dry frame	7	0	30	Up-cycle	5126	3131
S15	Dry frame	10	0	30	Up-cycle	5157	3128
S15	Dry frame	20	0	30	Up-cycle	5237	3139
S15	Dry frame	30	0	30	Up-cycle	5295	3151
S15	Dry frame	7	0	40	Up-cycle	5134	3131
S15	Dry frame	10	0	40	Up-cycle	5142	3131
S15	Dry frame	20	0	40	Up-cycle	5229	3142
S15	Dry frame	30	0	40	Up-cycle	5278	3151
S15	Dry frame	7	0	50	Up-cycle	5103	3116
S15	Dry frame	10	0	50	Up-cycle	5126	3119
S15	Dry frame	20	0	50	Up-cycle	5237	3139
S15	Dry frame	30	0	50	Up-cycle	5278	3148
S15	Dry frame	7	0	60	Up-cycle	5103	3113
S15	Dry frame	10	0	60	Up-cycle	5118	3110
S15	Dry frame	20	0	60	Up-cycle	5213	3131
S15	Dry frame	30	0	60	Up-cycle	5270	3139

S15	Dry frame	7	0	70	Up-cycle	5095	3099
S15	Dry frame	10	0	70	Up-cycle	5103	3102
S15	Dry frame	20	0	70	Up-cycle	5197	3122
S15	Dry frame	30	0	70	Up-cycle	5270	3134
S15	Dry frame	7	0	80	Up-cycle	5064	3079
S15	Dry frame	10	0	80	Up-cycle	5064	3085
S15	Dry frame	20	0	80	Up-cycle	5173	3110
S15	Dry frame	30	0	80	Up-cycle	5237	3122
S15	Dry frame	7	0	90	Up-cycle	5034	3063
S15	Dry frame	10	0	90	Up-cycle	5034	3074
S15	Dry frame	20	0	90	Up-cycle	5149	3108
S15	Dry frame	30	0	90	Up-cycle	5229	3125
S15	Dry frame	7	0	100	Up-cycle	4997	3046
S15	Dry frame	10	0	100	Up-cycle	4997	3063
S15	Dry frame	20	0	100	Up-cycle	5134	3105
S15	Dry frame	30	0	100	Up-cycle	5213	3122
S15	Water saturation	7	0	10	Up-cycle	5245	3046
S15	Water saturation	10	3	10	Up-cycle	5253	3049
S15	Water saturation	20	13	10	Up-cycle	5253	3043
S15	Water saturation	30	23	10	Up-cycle	5262	3038
S15	Water saturation	7	0	20	Up-cycle	5181	3041
S15	Water saturation	10	3	20	Up-cycle	5245	3038
S15	Water saturation	20	13	20	Up-cycle	5245	3032
S15	Water saturation	30	23	20	Up-cycle	5253	3032
S15	Water saturation	7	0	30	Up-cycle	5181	3041
S15	Water saturation	10	3	30	Up-cycle	5237	3032
S15	Water saturation	20	13	30	Up-cycle	5245	3032
S15	Water saturation	30	23	30	Up-cycle	5245	3027
S15	Water saturation	7	0	40	Up-cycle	5165	3027
S15	Water saturation	10	3	40	Up-cycle	5213	3024
S15	Water saturation	20	13	40	Up-cycle	5213	3016
S15	Water saturation	30	23	40	Up-cycle	5221	3016
S15	Water saturation	7	0	50	Up-cycle	5165	2976
S15	Water saturation	10	3	50	Up-cycle	5181	2981
S15	Water saturation	20	13	50	Up-cycle	5213	2992
S15	Water saturation	30	23	50	Up-cycle	5229	2992
S15	Water saturation	7	0	60	Up-cycle	5165	2992
S15	Water saturation	10	3	60	Up-cycle	5173	2987
S15	Water saturation	20	13	60	Up-cycle	5189	2984
S15	Water saturation	30	23	60	Up-cycle	5205	2984
S15	Water saturation	7	0	70	Up-cycle	5126	2976

S15	Water saturation	10	3	70	Up-cycle	5134	2976
S15	Water saturation	20	13	70	Up-cycle	5157	2976
S15	Water saturation	30	23	70	Up-cycle	5173	2974
S15	Water saturation	7	0	80	Up-cycle	5080	2958
S15	Water saturation	10	3	80	Up-cycle	5080	2953
S15	Water saturation	20	13	80	Up-cycle	5095	2953
S15	Water saturation	30	23	80	Up-cycle	5118	2955
S15	Water saturation	7	0	90	Up-cycle	5012	2935
S15	Water saturation	10	3	90	Up-cycle	5042	2935
S15	Water saturation	20	13	90	Up-cycle	5064	2943
S15	Water saturation	30	23	90	Up-cycle	5072	2940
S15	Water saturation	7	0	100	Up-cycle	5034	2925
S15	Water saturation	10	3	100	Up-cycle	5034	2930
S15	Water saturation	20	13	100	Up-cycle	5049	2935
S15	Water saturation	30	23	100	Up-cycle	5064	2932
S17	Natural saturation	7	0	10	Up-cycle	NaN	2327
S17	Natural saturation	10	0	10	Up-cycle	NaN	2338
S17	Natural saturation	20	0	10	Up-cycle	4066	2390
S17	Natural saturation	30	0	10	Up-cycle	4184	2417
S17	Natural saturation	7	0	20	Up-cycle	NaN	2301
S17	Natural saturation	10	0	20	Up-cycle	NaN	2314
S17	Natural saturation	20	0	20	Up-cycle	4058	2345
S17	Natural saturation	30	0	20	Up-cycle	4133	2364
S17	Natural saturation	7	0	30	Up-cycle	NaN	2248
S17	Natural saturation	10	0	30	Up-cycle	NaN	2262
S17	Natural saturation	20	0	30	Up-cycle	4006	2295
S17	Natural saturation	30	0	30	Up-cycle	4070	2314
S17	Natural saturation	7	0	40	Up-cycle	NaN	2184
S17	Natural saturation	10	0	40	Up-cycle	NaN	2197
S17	Natural saturation	20	0	40	Up-cycle	3920	2236
S17	Natural saturation	30	0	40	Up-cycle	3994	2257
S17	Natural saturation	7	0	50	Up-cycle	NaN	2117
S17	Natural saturation	10	0	50	Up-cycle	NaN	2157
S17	Natural saturation	20	0	50	Up-cycle	3868	2191
S17	Natural saturation	30	0	50	Up-cycle	3932	2214
S17	Natural saturation	7	0	60	Up-cycle	NaN	2087
S17	Natural saturation	10	0	60	Up-cycle	NaN	2105
S17	Natural saturation	20	0	60	Up-cycle	3831	2165
S17	Natural saturation	30	0	60	Up-cycle	3898	2187
S17	Natural saturation	7	0	70	Up-cycle	NaN	2063
S17	Natural saturation	10	0	70	Up-cycle	NaN	2075

S17	Natural saturation	20	0	70	Up-cycle	3778	2134
S17	Natural saturation	30	0	70	Up-cycle	3839	2158
S17	Natural saturation	7	0	80	Up-cycle	NaN	2050
S17	Natural saturation	10	0	80	Up-cycle	NaN	2056
S17	Natural saturation	20	0	80	Up-cycle	3736	2110
S17	Natural saturation	30	0	80	Up-cycle	3799	2140
S17	Natural saturation	7	0	90	Up-cycle	NaN	NaN
S17	Natural saturation	10	0	90	Up-cycle	NaN	2042
S17	Natural saturation	20	0	90	Up-cycle	3705	2092
S17	Natural saturation	30	0	90	Up-cycle	3767	2126
S17	Natural saturation	7	0	100	Up-cycle	NaN	2008
S17	Natural saturation	10	0	100	Up-cycle	NaN	2030
S17	Natural saturation	20	0	100	Up-cycle	3691	2087
S17	Natural saturation	30	0	100	Up-cycle	3753	2118
S17	Natural saturation	7	0	10	Up-cycle	4241	2442
S17	Natural saturation	10	3	10	Up-cycle	4259	2444
S17	Natural saturation	20	13	10	Up-cycle	4314	2454
S17	Natural saturation	30	23	10	Up-cycle	4342	2459
S17	Natural saturation	7	0	20	Up-cycle	4120	2368
S17	Natural saturation	10	3	20	Up-cycle	4146	2372
S17	Natural saturation	20	13	20	Up-cycle	4202	2385
S17	Natural saturation	30	23	20	Up-cycle	4228	2392
S17	Natural saturation	7	0	30	Up-cycle	4006	2290
S17	Natural saturation	10	3	30	Up-cycle	4030	2294
S17	Natural saturation	20	13	30	Up-cycle	4099	2315
S17	Natural saturation	30	23	30	Up-cycle	4137	2327
S17	Natural saturation	7	0	40	Up-cycle	3917	2228
S17	Natural saturation	10	3	40	Up-cycle	3940	2239
S17	Natural saturation	20	13	40	Up-cycle	4022	2264
S17	Natural saturation	30	23	40	Up-cycle	4062	2278
S17	Natural saturation	7	0	50	Up-cycle	3839	2180
S17	Natural saturation	10	3	50	Up-cycle	3872	2190
S17	Natural saturation	20	13	50	Up-cycle	3955	2218
S17	Natural saturation	30	23	50	Up-cycle	4002	2238
S17	Natural saturation	7	0	60	Up-cycle	3792	2149
S17	Natural saturation	10	3	60	Up-cycle	3817	2156
S17	Natural saturation	20	13	60	Up-cycle	3902	2184
S17	Natural saturation	30	23	60	Up-cycle	3951	2202
S17	Natural saturation	7	0	70	Up-cycle	3708	2078
S17	Natural saturation	10	3	70	Up-cycle	3746	2105
S17	Natural saturation	20	13	70	Up-cycle	3828	2150

S17	Natural saturation	30	23	70	Up-cycle	3887	2170
S17	Natural saturation	7	0	80	Up-cycle	3675	2058
S17	Natural saturation	10	3	80	Up-cycle	3688	2071
S17	Natural saturation	20	13	80	Up-cycle	3774	2121
S17	Natural saturation	30	23	80	Up-cycle	3831	2140
S17	Natural saturation	7	0	90	Up-cycle	3655	2040
S17	Natural saturation	10	3	90	Up-cycle	3658	2051
S17	Natural saturation	20	13	90	Up-cycle	3746	2095
S17	Natural saturation	30	23	90	Up-cycle	3810	2120
S17	Natural saturation	7	0	100	Up-cycle	3648	2009
S17	Natural saturation	10	3	100	Up-cycle	3661	2021
S17	Natural saturation	20	13	100	Up-cycle	3715	2042
S17	Natural saturation	30	23	100	Up-cycle	3753	2055
S17	Dry frame	7	0	10	Up-cycle	NaN	2106
S17	Dry frame	10	0	10	Up-cycle	NaN	2157
S17	Dry frame	20	0	10	Up-cycle	3688	2225
S17	Dry frame	30	0	10	Up-cycle	3747	2253
S17	Dry frame	7	0	20	Up-cycle	NaN	2096
S17	Dry frame	10	0	20	Up-cycle	NaN	2129
S17	Dry frame	20	0	20	Up-cycle	3655	2209
S17	Dry frame	30	0	20	Up-cycle	3747	2251
S17	Dry frame	7	0	30	Up-cycle	NaN	2090
S17	Dry frame	10	0	30	Up-cycle	NaN	2125
S17	Dry frame	20	0	30	Up-cycle	3658	2205
S17	Dry frame	30	0	30	Up-cycle	3747	2248
S17	Dry frame	7	0	40	Up-cycle	NaN	2087
S17	Dry frame	10	0	40	Up-cycle	NaN	2124
S17	Dry frame	20	0	40	Up-cycle	3658	2205
S17	Dry frame	30	0	40	Up-cycle	3743	2243
S17	Dry frame	7	0	50	Up-cycle	NaN	2090
S17	Dry frame	10	0	50	Up-cycle	NaN	2128
S17	Dry frame	20	0	50	Up-cycle	3661	2204
S17	Dry frame	30	0	50	Up-cycle	3743	2245
S17	Dry frame	7	0	60	Up-cycle	NaN	2084
S17	Dry frame	10	0	60	Up-cycle	NaN	2122
S17	Dry frame	20	0	60	Up-cycle	3671	2199
S17	Dry frame	30	0	60	Up-cycle	3743	2240
S17	Dry frame	7	0	70	Up-cycle	NaN	2089
S17	Dry frame	10	0	70	Up-cycle	NaN	2127
S17	Dry frame	20	0	70	Up-cycle	3668	2199
S17	Dry frame	30	0	70	Up-cycle	3740	2238

S17	Dry frame	7	0	80	Up-cycle	NaN	2065
S17	Dry frame	10	0	80	Up-cycle	NaN	2117
S17	Dry frame	20	0	80	Up-cycle	3661	2193
S17	Dry frame	30	0	80	Up-cycle	3729	2232
S17	Dry frame	7	0	90	Up-cycle	NaN	2075
S17	Dry frame	10	0	90	Up-cycle	NaN	2119
S17	Dry frame	20	0	90	Up-cycle	3658	2191
S17	Dry frame	30	0	90	Up-cycle	3726	2231
S17	Dry frame	7	0	100	Up-cycle	NaN	2076
S17	Dry frame	10	0	100	Up-cycle	NaN	2111
S17	Dry frame	20	0	100	Up-cycle	3655	2187
S17	Dry frame	30	0	100	Up-cycle	3722	2226
S17	Water saturation	7	0	10	Up-cycle	3681	2016
S17	Water saturation	10	3	10	Up-cycle	3747	2017
S17	Water saturation	20	13	10	Up-cycle	3757	2012
S17	Water saturation	30	23	10	Up-cycle	3764	2011
S17	Water saturation	7	0	20	Up-cycle	3708	1999
S17	Water saturation	10	3	20	Up-cycle	3740	2000
S17	Water saturation	20	13	20	Up-cycle	3736	1986
S17	Water saturation	30	23	20	Up-cycle	3757	1997
S17	Water saturation	7	0	30	Up-cycle	3705	1989
S17	Water saturation	10	3	30	Up-cycle	3729	1984
S17	Water saturation	20	13	30	Up-cycle	3747	1989
S17	Water saturation	30	23	30	Up-cycle	3757	1989
S17	Water saturation	7	0	40	Up-cycle	3722	1988
S17	Water saturation	10	3	40	Up-cycle	3733	1989
S17	Water saturation	20	13	40	Up-cycle	3733	1980
S17	Water saturation	30	23	40	Up-cycle	3747	1984
S17	Water saturation	7	0	50	Up-cycle	3691	1974
S17	Water saturation	10	3	50	Up-cycle	3719	1974
S17	Water saturation	20	13	50	Up-cycle	3729	1974
S17	Water saturation	30	23	50	Up-cycle	3726	1965
S17	Water saturation	7	0	60	Up-cycle	3695	1967
S17	Water saturation	10	3	60	Up-cycle	3702	1966
S17	Water saturation	20	13	60	Up-cycle	3715	1966
S17	Water saturation	30	23	60	Up-cycle	3726	1968
S17	Water saturation	7	0	70	Up-cycle	3668	1958
S17	Water saturation	10	3	70	Up-cycle	3681	1958
S17	Water saturation	20	13	70	Up-cycle	3688	1955
S17	Water saturation	30	23	70	Up-cycle	3702	1954
S17	Water saturation	7	0	80	Up-cycle	3665	1953

S17	Water saturation	10	3	80	Up-cycle	3671	1952
S17	Water saturation	20	13	80	Up-cycle	3685	1953
S17	Water saturation	30	23	80	Up-cycle	3698	1954
S17	Water saturation	7	0	90	Up-cycle	3641	1942
S17	Water saturation	10	3	90	Up-cycle	3648	1943
S17	Water saturation	20	13	90	Up-cycle	3658	1945
S17	Water saturation	30	23	90	Up-cycle	3671	1944
S17	Water saturation	7	0	100	Up-cycle	3648	1934
S17	Water saturation	10	3	100	Up-cycle	3641	1937
S17	Water saturation	20	13	100	Up-cycle	3655	1945
S17	Water saturation	30	23	100	Up-cycle	3665	1944